

POLITECNICO
MILANO 1863

SCUOLA DI INGEGNERIA INDUSTRIALE
E DELL'INFORMAZIONE

Modeling of High-Power Microwave Grating Couplers for Fusion Plasma Heating Systems

Tesi di Laurea Magistrale in
Telecommunication Engineering
Ingegneria delle Telecomunicazioni

Author: **Gabriele Lecce**

Student ID: 10703432
Advisor: Prof. Gian Guido Gentili
Co-advisors: Dr. Alessandro Bruschi, Dr. Francesco Fanale,
Dr. Alessandro Simonetto
Academic Year: 2025-26

Abstract

The design of highly efficient quasi-optical components is a critical requirement for the Electron Cyclotron Resonance Heating (ECRH) system of the Divertor Tokamak Test (DTT) fusion experiment, currently under construction at the ENEA research center in Frascati (Italy). In this thesis, a rigorous numerical tool based on the Mode-Matching (MM) Method was developed and applied to the modeling of metallic grating couplers. The primary objective was to establish a practical, self-consistent computational tool capable of evaluating both the grating efficiencies and the complex spatial characteristics of the diffracted Gaussian beams. The accuracy of the developed code was validated through benchmarking against Finite Element Method (FEM) simulations and analytical predictions derived from the tensor ABCD law. Although primarily focused on grating couplers, the tool is highly versatile because it can be employed for any reflector shape with one-dimensional lamellar grating patterns. Furthermore, the tool can be extended in the future to cover arbitrary groove shapes. This work represents a fundamental first step towards the design of a complete diagnostic system for measuring the electromagnetic characteristics of the electron cyclotron waves injected into fusion plasmas.

Keywords: grating couplers, mode-matching method, electron cyclotron resonance heating, nuclear fusion

Abstract in lingua italiana

La progettazione di componenti quasi-ottici ad alte prestazioni riveste un ruolo fondamentale per il sistema di riscaldamento a risonanza ciclotronica elettronica (ECRH) dell'esperimento di fusione Divertor Tokamak Test (DTT), attualmente in costruzione al centro di ricerca ENEA a Frascati (Italia). In questa tesi, è stato sviluppato un software basato sul Metodo del Mode-Matching (MM) per la progettazione di accoppiatori a reticolo metallico. Questo codice numerico è in grado di calcolare con accuratezza le efficienze del reticolo e le caratteristiche spaziali dei fasci gaussiani diffratti dai riflettori. Il codice è stato validato confrontandone i risultati con simulazioni basate sul Metodo degli Elementi Finiti (FEM) e con la teoria dei fasci gaussiani. La versatilità di questo codice permette di impiegarlo su riflettori di forma arbitraria con corrugazioni rettangolari monodimensionali. In sviluppi futuri, inoltre, il modello potrà essere esteso per trattare reticoli di forma arbitraria. Questo lavoro rappresenta un primo passo fondamentale verso la progettazione di un sistema diagnostico completo, essenziale per misurare le proprietà elettromagnetiche delle onde ciclotroniche elettroniche iniettate nei plasmi da fusione.

Parole chiave: accoppiatori a reticolo, metodo del mode-matching, riscaldamento a risonanza ciclotronica elettronica, fusione nucleare

Contents

Abstract **i**

Abstract in lingua italiana **iii**

Contents **v**

Introduction **1**

1 Nuclear Fusion Technologies **3**
1.1 Introduction to Nuclear Fusion . . . 3
1.1.1 Fusion Reactions and Magnetic Confinement . . . 4
1.2 ECRH systems . . . 6
1.2.1 Gyrotrons . . . 10
1.2.2 Transmission Lines . . . 13
1.2.3 Launching Systems . . . 18
1.2.4 Power Diagnostic Techniques . . . 20
1.3 Fusion Experiments . . . 24
1.3.1 Divertor Tokamak Test (DTT) . . . 25

2 Grating Reflectors Theory and Applications **29**
2.1 Diffraction Gratings Theory . . . 29
2.1.1 Numerical Methods for Grating Efficiency . . . 32
2.2 Quasi-Optical Theory . . . 33
2.2.1 ABCD matrices . . . 34
2.2.2 Tensor ABCD Law . . . 37
2.3 Applications of Grating Reflectors . . . 40
2.3.1 W7-X Grating Coupler . . . 40
2.3.2 DTT Grating Polarizer . . . 45

3 Mode-Matching Method for Grating Reflectors **47**
3.1 Mode-Matching of 1D Lamellar Grooves 48
3.1.1 Fields in the Slot 51
3.1.2 Groove Mode-Matching 54
3.2 Gaussian Beam Diffraction 57
3.3 MATLAB Implementation and Convergence 60

4 DTT Grating Couplers Design **67**
4.1 Geometrical parameters 68
4.2 Splitting Mirrors Design 69
4.2.1 Central Splitting Mirror 71
4.2.2 Lateral Splitting Mirrors 74
4.3 Gaussian Beam Parameters 77
4.4 Fabrication Tolerances and Alternative Designs 79

5 Conclusions and Future Developments **81**

Bibliography **83**

A Appendix A **91**

List of Figures **97**

List of Tables **101**

Introduction

The Divertor Tokamak Test (DTT) facility, currently under construction at the ENEA research center in Frascati (Italy), relies on its Electron Cyclotron Resonance Heating (ECRH) system to deliver highly localized power to the fusion plasma. Supplying up to 32 MW through gyrotrons operating at 170 GHz, the ECRH system is fundamental to control the fusion plasma and provide additional heating. To guarantee the operation of such a system, the electromagnetic characteristics of the electron cyclotron (EC) waves traveling towards the plasma should be known with high precision. For example, transmitted power, alignment, mode purity, and polarization state must be continuously monitored. In quasi-optical transmission lines, this monitoring is commonly achieved by means of metallic grating couplers: diffraction-grating mirrors that couple a small fraction of the main beam into a diagnostic diffraction order, while the specular reflection carries the power towards the antenna launchers. The diffracted beam is subsequently focused into a horn antenna, from which the beam parameters can be retrieved. In the DTT ECRH system, such couplers are planned to be machined directly onto the splitting mirrors located at the end of the multi-beam (MB) transmission line. The design of these components requires the accurate evaluation of both the diffraction efficiencies and the complex spatial characteristics of the diffracted Gaussian beams. Electromagnetic commercial solvers can provide this information, but they are impractical for the rapid parametric sweeps and iterative optimization loops needed during the design phase. Therefore, the scope of this thesis is the development, implementation, and validation of a rigorous, self-consistent numerical tool, based on mode-matching theory, for the design of metallic grating couplers. The tool handles arbitrary reflector geometries with 1D periodic lamellar corrugations in conical mounting, and it is benchmarked against FEM simulations for the diffraction efficiencies and against the tensor ABCD law for the Gaussian beam parameters. This work represents a fundamental first step towards the modeling of a complete quasi-optical diagnostic system for the EC waves of the DTT ECRH system. The thesis is divided as follows: **Chapter 1** introduces the principles of nuclear fusion and magnetic confinement, the objectives of fusion research, and the main components of ECRH systems. **Chapter 2** presents diffraction grating theory and the fundamentals of

quasi-optics and Gaussian beam propagation. The W7-X grating coupler and the DTT grating polarizer are analyzed as benchmark applications. **Chapter 3** details the mathematical formulation and numerical implementation of the mode-matching tool, validating its convergence. **Chapter 4** applies the developed tool to the design of the DTT splitting mirrors, evaluating the results against the FEM simulations and analytical predictions. **Chapter 5** summarizes the main achievements of this work and future developments.

1 | Nuclear Fusion Technologies

This chapter introduces the main technologies employed in nuclear fusion research and the challenges of future fusion experiments. In particular, Electron Cyclotron Resonance Heating (ECRH), one of the most prominent methods to deliver power in fusion plants, is described. Particular attention is given to the high-power, high-frequency microwave components, transmission lines, and diagnostic methods of ECRH systems.

1.1. Introduction to Nuclear Fusion

Nuclear fusion is an interdisciplinary research field that has been extensively pursued over the last seven to eight decades as a long-term solution for achieving an inherently safe and virtually unlimited source of energy. A key advantage of thermonuclear fusion is its reliance on fuel that is abundant in nature and produces minimal short-lived radioactive waste [1]. Including fusion as part of the energy mix, alongside fission and intermittent renewable sources such as wind and solar, could reduce the global dependence on fossil fuels to generate electricity. Future fusion power plants are estimated to produce approximately 1 GW of electrical power by converting thermal power using a conventional steam cycle [2]. However, many challenges arise from the conceptual studies of these new types of power plants. To start fusion reactions, the fuel isotopes must overcome electrostatic repulsion, and extremely high temperatures similar to those found in stars are required. Under these conditions, particles ionize forming a plasma; a deep understanding of plasma physics is thus required to control fusion reactions inside reactors. Research efforts in applied and fundamental physics and engineering have achieved an advanced level of understanding of how to generate and control fusion plasmas, and many research institutes and private companies are currently trying to apply this knowledge to design the first commercial fusion power plant [3]. It should be noted that the cost of building a nuclear fusion power plant is a significant factor, and should be competitive with fission reactors or other sources of energy. Currently, two main research lines are pursued in parallel to achieve the design of a fusion power plant: magnetic confinement fusion (MCF) and inertial confinement fusion (ICF). The former uses magnetic fields to confine

fusion plasmas at high temperatures for long periods of time, while the latter employs high-power pulsed lasers to compress and heat small pellets filled with thermonuclear fuel. Despite progress, research and development challenges are still present in both fields. The European roadmap to fusion electricity [4] focuses on magnetically confined plasmas of a deuterium-tritium (DT) mixture. In Europe, the most important planned fusion experiments are the International Thermonuclear Experimental Reactor (ITER) and the DEMOnstration power plant (DEMO). The former aims to demonstrate the feasibility of a fusion power plant with a ratio (Q-factor) of output power from fusion reactions to input power from heating systems of $Q = 10$, thus obtaining a power output of approximately 500 MW in pulses of 400 s. DEMO will be the successor of ITER, and its aim will be to achieve production of electricity with a self-sufficient fuel cycle. Together with ITER and DEMO, many other fusion devices, such as JET, ASDEX Upgrade, W7-X and DTT have been devised over the last decades to study important characteristics of the operation of power fusion plants, such as withstanding large power loads, ensuring the economic potential of fusion reactors and developing alternative magnetic confinement configurations. In particular, the Divertor Tokamak Test (DTT), currently under construction at the Frascati ENEA research center in Italy, aims to study the control of power and particle exhaust in a fusion reactor [5]. Fusion reactors require powerful heating systems on the order of megawatts to perform many different relevant tasks, such as plasma heating and start-up, instability suppression and control of current profiles. As an example, DTT employs three different heating systems: the Ion-Cyclotron Resonance Heating (ICRH) uses radio-frequency waves at 60–90 MHz, the Neutral Beam Injection (NBI) Heating injects 510 keV neutral particles, and the Electron Cyclotron Resonance Heating (ECRH) employs microwaves at 170 GHz [5, 6].

1.1.1. Fusion Reactions and Magnetic Confinement

Nuclear reactions are easily produced at the center of stars due to their extreme gravitational force. Therefore, typical values of pressure of 150×10^9 bar and temperature of 15×10^6 °C make feasible fusion reactions like the proton-proton chain, which has a low reaction cross-section. On Earth, fusion reactions can be achieved by magnetically confined thermo-nuclear fusion plasmas with isotopes of higher reaction cross-section such as the deuterium-tritium reaction

$$^2\mathrm{D} + {}^3\mathrm{T} \rightarrow {}^4\mathrm{He}\,(3.5\,\mathrm{MeV}) + n\,(14.1\,\mathrm{MeV}), \tag{1.1}$$

at temperatures of about 150×10^6 °C and pressures of a few bars [2]. Deuterium is easily obtained from seawater, while tritium is produced through the reaction

$$^{6}\mathrm{Li} + \mathrm{n} \rightarrow {}^{4}\mathrm{He} + {}^{3}\mathrm{T} + 4.78\,\mathrm{MeV} \tag{1.2a}$$

$$^{7}\mathrm{Li} + \mathrm{n} \rightarrow {}^{4}\mathrm{He} + {}^{3}\mathrm{T} + \mathrm{n} - 2.47\,\mathrm{MeV}. \tag{1.2b}$$

The produced helium is a non-radioactive and non-toxic exhaust product commonly called alpha particle. To obtain a self-sustaining reaction cycle, neutrons obtained from the DT reaction escape from the plasma and produce tritium by reacting with the lithium breeding blanket constituting the inner walls of the plasma chamber. Fusion ignition is described as a two-step process: magnetically confining plasma in a stable configuration and maintaining self-sustaining reactions [1]. Tokamaks and stellarators are the two main toroidal devices currently being studied to achieve magnetic confinement. However, research has been predominantly focused on tokamaks due to the technical complexity of building stellarators [7]. Both are evaluated considering trade-offs between physics and engineering advantages and disadvantages. The objective of these devices is to compensate for the plasma pressure by using magnetic fields and control the charged particles through the Lorentz force [8]. In tokamaks, the magnetic field is generated by a combination of a toroidal field from superconducting external coils and a poloidal field generated by toroidal currents inductively driven by a transformer, as shown in Fig. 1.1. The resulting helical magnetic field is necessary to avoid the drift of charged plasma particles towards the tokamak walls, which may release cold impurities and cause plasma instabilities. The drift is caused by the gradient of the toroidal magnetic field, which is stronger at the inner side of the torus than on the outer side. However, tokamaks have some disadvantages: the transformer limits the device to pulsed regimes and the toroidal plasma current may cause magnetohydrodynamic (MHD) instability which disrupts the plasma operation. Due to the electrical resistance of the plasma, this current heats the plasma via the Joule effect, but not enough to reach fusion ignition temperatures on its own. This kind of current is negligible in stellarators because the twisted magnetic field is entirely generated by helical external coils. Thus, stellarators can operate in steady state, but have the disadvantage of having an asymmetric configuration, which drastically increases the neoclassical transport (random walk) of energetic particles like alpha particles. ITER and DEMO are based on the tokamak device, but problems due to disruptions of operation caused by current-driven instabilities are pushing research on stellarators. To achieve ignition we need to satisfy the simplified Lawson criterion [2]

$$n_i \tau_{\mathrm{E}} \geq 2 \times 10^{20} \mathrm{m}^{-3}\mathrm{s}, \tag{1.3}$$

where n_i is the ion density and τ_E is the energy-confinement time, which is the time the plasma maintains its temperature if heating power is switched off. If the criterion is satisfied, the plasma remains hot enough to allow fusion reactions for a long time. With the additional heating power switched off, power from DT-produced alpha particles is enough to sustain the reaction, thus reaching an infinite Q-factor (no input power). Nevertheless, to keep the plasma in steady state with a constant temperature, systems to manage power and particle exhaust are needed, and deuterium and tritium should be continuously injected into the plasma chamber.

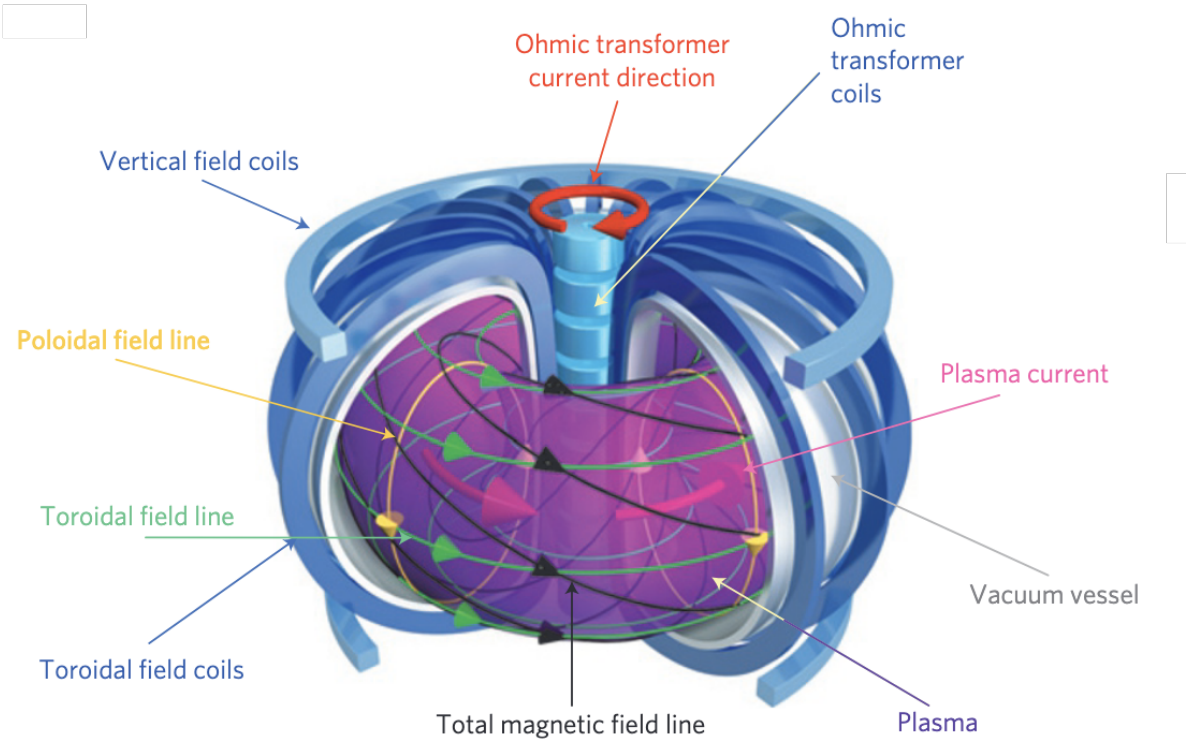


Figure 1.1: Scheme of the main components of a tokamak [2]. Key components include the toroidal and vertical field coils, the ohmic transformer to generate the plasma current, and the vacuum vessel that supports the breeding blanket and the divertor.

1.2. ECRH systems

Electron cyclotron resonance heating (ECRH) is a well-established method for heating and ionization of magnetically confined fusion plasmas with high-power (∼1 MW) millimeter waves (∼30–300 GHz). Its theoretical basis was developed during the 1960s and 1970s, and has been confirmed by many experimental works [9]. In recent years, thanks to progress

in the development of high-power microwave sources and in the technology to transmit and launch microwaves into the plasma, ECRH has attracted growing interest and is now widely used in toroidal magnetic confinement devices for fusion energy applications [10]. In addition to ECRH, electron cyclotron current drive (ECCD) methods can be used to control the current profiles and suppress instabilities in tokamaks. Electron cyclotron (EC) waves are able to propagate as narrow, highly collimated beams that efficiently penetrate the vacuum-plasma boundary without reflection. This allows highly localized absorption of power and the use of launchers far from the plasma chamber to avoid introduction of impurities. To optimally use EC waves as a heating mechanism of ECRH systems, three main ingredients are required [11]:

- Launching a well-collimated beam at the plasma.
- Controlling the direction of propagation of the beam.
- Controlling the polarization depending on the launching direction and the harmonic number of the resonance.

To satisfy these requirements, high-power microwaves with high mode purity are needed. Such microwaves are usually generated by gyrotrons. Many gyrotrons have been studied and developed over the past years, differing in their desired output mode, output power, efficiency, frequency range and pulse duration [12]. The typical frequency range corresponds to the electron cyclotron frequency, which for modern toroidal magnetic confinement devices goes from 28 to 170 GHz [13]:

$$f_{\mathrm{ce}} = s\frac{\Omega_{\mathrm{e}}}{2\pi} = s\frac{1}{2\pi}\frac{|e|B}{m_{\mathrm{e}}}, \tag{1.4}$$

where Ω_{e} is the electron cyclotron angular frequency, e is the electron charge, B the magnetic field of the toroidal device, m_{e} the electron rest mass and s is the harmonic number. To control the propagation and the properties of the emitted beams between the source and the launcher, passive high-power microwave components such as waveguide mode converters, polarizers, mode selective filters, directional couplers and beam combiners and dividers are used [14]. These high-power components are implemented in low-loss oversized metallic waveguides or quasi-optical beam waveguides which guarantee transmission with low-ohmic attenuation and high mode purity. It is important to notice that high-power microwave components and transmission lines are not only fundamental for fusion plasma applications, but are also present in a wide range of different material science and telecommunications technologies such as materials processing, spectroscopy, deep-space and specialized satellite communication, high-resolution radar ranging and

imaging [15]. Fusion applications require high frequency, high energy, and long pulses (or continuous operation); by contrast, materials processing demands high power but at lower frequencies than fusion, while radar systems operate at high peak power and high frequency but with short pulses. At the end of the transmission lines, we find antenna launchers to emit EC waves into the plasma with a defined direction and polarization. The dispersion relation for the refractive index of propagating EC modes can be obtained in the cold plasma limit, where electrons and ions are considered zero-temperature frictionless charged fluids in a constant magnetic field. The refractive index of the EC waves depends on which mode is excited [16, 17]:

$$n^2_{\text{O-mode}} = 1 - \frac{\omega^2_{\text{pe}}}{\omega^2} \frac{2(\omega^2 - \omega^2_{\text{pe}})}{2(\omega^2 - \omega^2_{\text{pe}}) - \Omega^2_{\text{e}}(\sin^2\theta - \rho)} \tag{1.5a}$$

$$n^2_{\text{X-mode}} = 1 - \frac{\omega^2_{\text{pe}}}{\omega^2} \frac{2(\omega^2 - \omega^2_{\text{pe}})}{2(\omega^2 - \omega^2_{\text{pe}}) - \Omega^2_{\text{e}}(\sin^2\theta + \rho)} \tag{1.5b}$$

and ρ is a parameter defined as

$$\rho = \sqrt{\sin^4\theta + 4\left(\frac{\omega^2 - \omega^2_{\text{pe}}}{\omega\Omega_{\text{e}}}\right)^2 \cos^2\theta}, \tag{1.6}$$

where

$$\omega_{\text{pe}} = \sqrt{\frac{n_{\text{e}} e^2}{\epsilon_0 m_{\text{e}}}} \tag{1.7}$$

is the electron plasma frequency, and θ is the angle between the direction of propagation and the magnetic field. Two normal modes of propagation are found, the ordinary mode (O-mode), and the extraordinary mode (X-mode). In the vacuum between the launcher and the plasma ($n_e \to 0$, $n_{\text{O-mode}} = n_{\text{X-mode}} \to 1$), the two modes are degenerate and propagate at the speed of light. At the plasma boundary, depending on the polarization, the beam is coupled with different power fractions to the two modes propagating independently into the plasma. For convenience and better control of the power, the polarization is adjusted so that only one of the two modes is excited, being the one that is better coupled, avoiding cutoffs in the plasma region or having a higher heating or current drive efficiency. The excited O- or X-mode will propagate in the plasma with minimal mode conversion if hot plasma effects are negligible. For propagation perpendicular to the stationary magnetic field B, the O-mode is linearly polarized with electric field parallel to B and is purely transverse, while the X-mode has a transverse field that is linearly polarized and perpendicular to B, with a longitudinal component along the propagation direction,

which is present only in the plasma and vanishes in vacuum. For non-perpendicular propagation, both modes become elliptically polarized, and the X-mode maintains its longitudinal component. The cut-off condition for the O-mode corresponds to

$$\omega_{\text{co, O-mode}} = \omega_{\text{pe}}, \tag{1.8}$$

while for the X-mode there are two cut-offs (low density and high density) assuming perpendicular propagation to B,

$$\omega_{\text{co, X-mode}} = \pm\frac{\Omega_{\text{e}}}{2} + \sqrt{\frac{\Omega_{\text{e}}^2}{4} + \omega_{\text{pe}}^2}. \tag{1.9}$$

These cut-off conditions can be visually represented by the Clemmow-Mullaly-Allis (CMA) diagrams, as shown in Fig. 1.2.

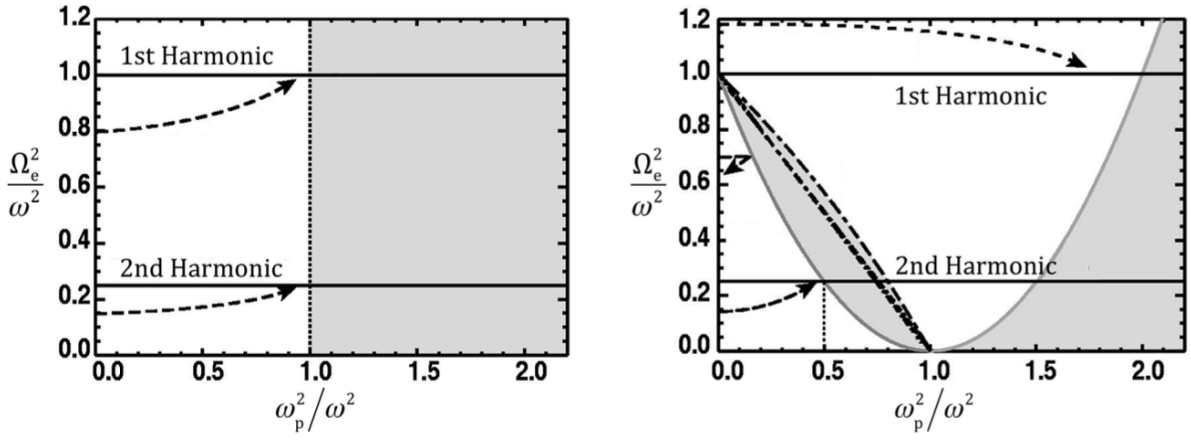


Figure 1.2: Clemmow-Mullaly-Allis (CMA) diagrams of the O-mode (left) and X-mode (right) in the cold plasma approximation. Dashed lines show possible propagation paths from the plasma boundary towards the resonance layer. Shaded areas are inaccessible due to the cut-off conditions [13].

These diagrams show how the dispersion relations limit the accessibility to the fundamental or harmonic resonance layers in inhomogeneous magnetized plasmas. For the O-mode the accessibility to the resonance layers depends only on the electron plasma frequency, which is proportional to the electron plasma density. For example, at electron densities of 2×10^{20} m^{-3}, as envisaged in the present experimental devices, the condition $\omega > \omega_{\text{pe}}$ is easily guaranteed for $\omega > 140$ GHz. Although the EC absorption mechanism for the O-mode is weaker than the one for the X-mode, an almost complete absorption at first harmonic is obtained at electron temperatures of a few keV. The X-mode is upper bounded

by the low density cut-off in the low-field side (LFS) ($\Omega_e/\omega < 1$), where it is reflected before reaching the first harmonic resonance. In the high-field side (HFS), the X-mode is lower bounded by both the low density and high density cut-offs. Therefore, due to these accessibility limits, higher harmonics are usually preferred from the low-field side, while the first harmonic can be reached only from the high-field side. Cyclotron resonant absorption depends on the polarization of the EC wave and happens at the resonance layers of the plasma. At a given frequency the position of the resonance regions depends mainly on the magnetic field intensity of the toroidal device and the toroidal direction of propagation of the EC beam. In a given device, the power deposition can be controlled by selecting a proper injection frequency and then changing the poloidal and toroidal direction of propagation of the EC beam with a suitable injection optics, allowing highly localized power deposition profiles.

1.2.1. Gyrotrons

ECRH systems require high-power sources of millimeter waves to generate narrow beams with well-defined polarizations and mode purity. The most effective sources are gyrotrons, which are part of a class of fast-wave vacuum electronic sources of coherent electromagnetic waves known as electron cyclotron masers (ECMs) [18, 19]. For ECRH systems, single-mode gyrotron emission of fundamental Gaussian beam modes (TEM_{00}) is preferred in order to achieve high mode purity ($\eta \geq 95\%$). Conversion of the output mode into a linearly polarized fundamental Gaussian mode is usually achieved by quasi-optical converters before reaching the output window. A scheme of a single-cavity gyrotron is shown in Fig. 1.3.

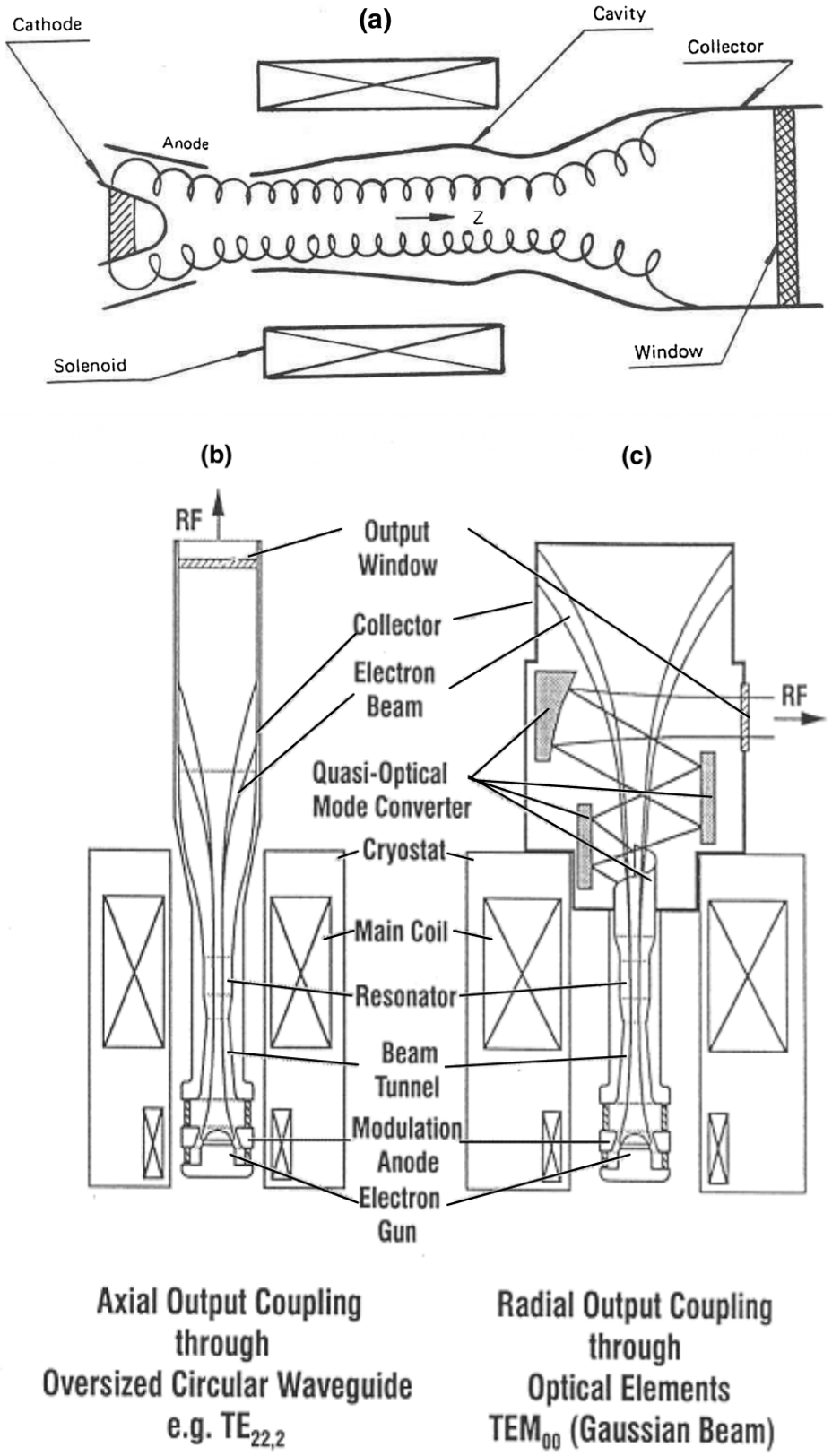


Figure 1.3: (a) Simplified scheme of a single-cavity gyrotron [18] and (b)-(c) examples of output coupling schemes for high-power high-frequency gyrotrons [14].

From an annular cathode of a magnetron-injection gun (MIG), an electron beam is emitted and accelerated by a DC voltage towards the resonant cavity. Since the electrons interact with the field only through the transverse component of their velocity, the beam is compressed by an increasing external magnetic field, which raises the perpendicular energy at the expense of the longitudinal one, before entering the cavity through a cutoff input section. Under the magnetic field, the electrons undergo a periodic oscillation. If this oscillation satisfies the cyclotron resonance condition, coherent radiation is emitted or amplified [20]. The resonance originates from the cyclotron maser instability [21], which depends on the relativistic dependence of the electron cyclotron frequency on the electron energy: electrons that give energy to the field increase their gyration frequency, while those that absorb energy decrease it. Since the magnetic field is set so that the cyclotron frequency lies slightly below the cavity resonance, the electrons that transfer energy shift towards resonance, while those that absorb it move away; this asymmetry sustains the instability and the coherent oscillation. The resonance condition is

$$\omega - \omega_{\mathrm{d}} = s\frac{\Omega_{\mathrm{e}}}{\gamma}, \tag{1.10}$$

where ω_{d} is a Doppler shift that depends on the longitudinal velocity, which does not contribute to the interaction and is therefore kept to the minimum needed for the spent beam to reach the collector intact and to avoid broadening of the cyclotron resonance band. γ is the relativistic factor

$$\gamma = \frac{1}{\sqrt{1-\left(\frac{v}{c}\right)^2}} = 1 + \frac{eV_0}{m_{\mathrm{e}}c^2}, \tag{1.11}$$

which can be expressed as a function of the accelerating voltage V_0. The emitted wave has a wavelength that does not depend on the geometry of the resonant structure, but primarily on the strength of the applied magnetic field. This permits the internal dimensions of the gyrotron cavity to be much larger than the wavelength, extending the high-power handling capabilities to the mm-wave range. After the wave is excited in a high-order cavity mode, an internal quasi-optical mode converter transforms it into a linearly polarized Gaussian beam (TEM_{00}), which is radiated through the output window with high efficiency, while the residual energy of the spent electron beam is dissipated at the collector. For current fusion experiments with magnetic confinement devices capable of generating magnetic fields up to $B \simeq$ 1–5.5 T, long-pulse and continuous wave (CW) gyrotrons with output powers of 0.1–1.3 MW and frequencies between 28–170 GHz are being employed [12]. Examples of state-of-the-art gyrotrons for fusion research are the

140 GHz IPP-KIT-THALES gyrotron operating at a maximum pulse length of 3 minutes and 1.3 MW output power, with 97.5% Gaussian output mode purity and the 170 GHz QST-CANON ITER gyrotron prototype at 800 seconds pulse length and 1 MW output power. Current research on gyrotrons keeps pushing the maximum operating frequency and output power to allow the feasibility of larger fusion machines with higher magnetic fields. Gyrotrons have also been widely used in radar systems for high-resolution ranging and imaging, and for deep-space and satellite communication; unlike the long-pulse and continuous wave fusion gyrotrons, these operate in shorter pulses and lower total energy [22]. Gyrotrons have also been considered as a source for data transmission systems in the sub-terahertz and terahertz frequency range, exploiting the atmospheric transparency at 200–300 GHz [23].

1.2.2. Transmission Lines

In ECRH systems, transmission of high-power microwaves from the gyrotron sources (gyrotron hall) to the plasma chamber is typically implemented through oversized corrugated metallic waveguides and open quasi-optical beam waveguides. To ensure reliable high-power operation and prevent electrical discharges, these transmission lines are typically evacuated. Corrugated waveguides consist of hollow metallic cylinders with periodic corrugations and transverse dimensions much larger than the wavelength, as shown in Fig. 1.4. Moreover, they are capable of handling power over 1 MW with a broadband operating spectrum and low cross-polarization for the HE_{11} in balanced conditions ($d = \lambda/4$) [14, 24].

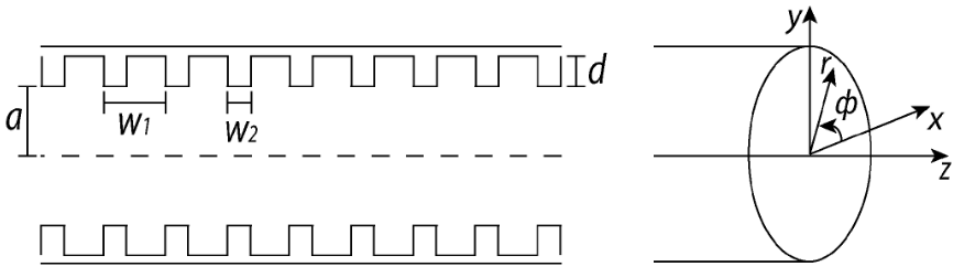


Figure 1.4: Section of a circular corrugated waveguide with radius $a \gg \lambda$, corrugation depth d, corrugation period w_1 and corrugation width w_2 [25].

These waveguides provide extremely low attenuation that scales proportionally with the ratio $(\lambda/a)^3$, with optimal corrugation depth $d = \lambda/4$ and corrugation period small with respect to λ. Although usually only the mode HE_{11} is propagated, overmoded corrugated

waveguides achieve low losses for higher-order modes as well, though these are still higher than those of the HE_{11}. A waveguide in balanced conditions ($d = \lambda/4$) supports TE_{0n} and TM_{0n} modes, and hybrid HE_{mn} and EH_{mn}, which can be easily represented by a set of linearly polarized modes LP_{mn} by summing modes with the same propagation constant (degenerate modes). This mode basis set is analogous to the one used for the propagation of modes in optical fibers within the weakly guiding approximation [26], with the important difference that in dielectric waveguides the fields are finite at the core-cladding interface, while for metallic waveguides the transverse electric field is equal to zero at the wall of the waveguide. Representing waves as LP_{mn} modes simplifies the analysis of linearly polarized input beams. The index $m \geq 0$ is the azimuthal number, and shows the degree of circular symmetry, while the index $n \geq 1$ is the radial number, showing the degree of radial symmetry, as in Fig. 1.5.

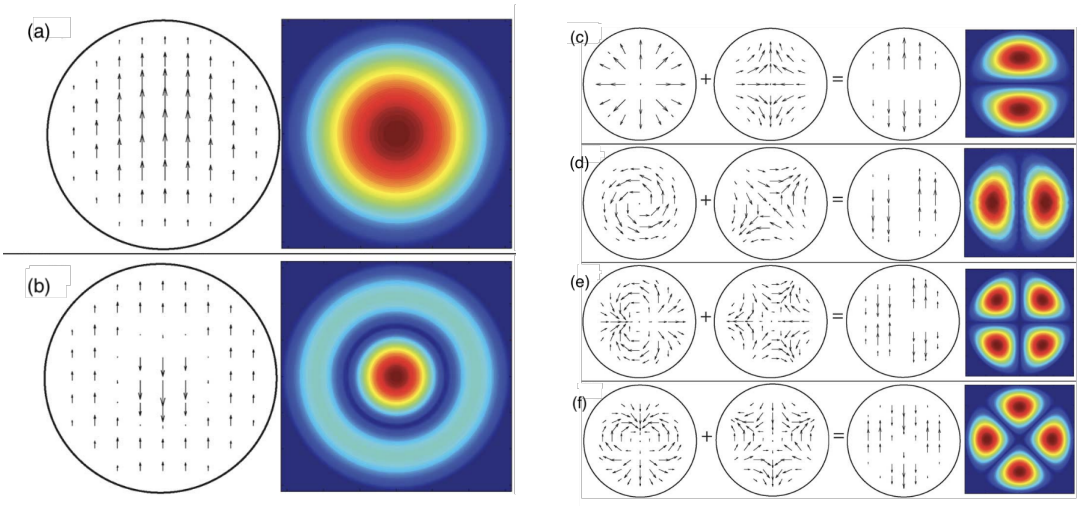


Figure 1.5: LP modes, showing how the degree of circular and radial symmetry changes with m and n: (a) LP_{01}, (b) LP_{02}, (c) LP_{11}-even, (d) LP_{11}-odd, (e) LP_{21}-even, (f) LP_{21}-odd. Even and odd modes are degenerate in the azimuthal direction [25].

LP_{mn} modes are degenerate in two orthogonal states of polarization, while modes with $m \neq 0$ are also degenerate in the azimuthal direction. The longitudinal electric field is proportional to λ/a, and thus negligible with respect to the transverse field. The mode LP_{01} matches well with the power distribution of linearly polarized TEM_{00} microwave beams produced by gyrotrons [25], allowing coupling with approximately $\eta = 98\%$ efficiency if the beam radius is chosen as $0.64a$ [24, 27]. The 2% theoretical loss is caused by the truncation of the Gaussian beam at the aperture of the waveguide and the difference in the amplitude profiles of the Gaussian and Bessel functions. As even a conversion loss as low as 2% can reduce the performance of the ECRH system, the mode conversion

between the TEM_{00} mode and LP_{01} mode can be improved by using hyperbolic horns as mode converters at the gyrotron output, achieving over $\eta = 99.5\%$ coupling efficiency. Defining E_A and E_B as field distributions over a cross section S, the coupled power is given by

$$\eta = \frac{|\langle E_A|E_B\rangle|^2}{\langle E_A|E_A\rangle \langle E_B|E_B\rangle}, \tag{1.12}$$

where the bracket notation $\langle E_A|E_B\rangle = \int_S E_A^* E_B dxdy$ has been introduced to simplify the expression. Additional losses may be caused by misalignment of the input beam, leading to the excitation and propagation of higher-order modes. In a circular overmoded corrugated waveguide in balanced conditions, assuming linear polarization over a generic axis, the mode LP_{01} can be described by a Bessel function of order zero

$$E(r) = \frac{1}{\sqrt{\pi} a J_1(X_{01})} J_0\left(X_{01}\frac{r}{a}\right). \tag{1.13}$$

Higher-order modes can be represented by the general form:

$$E_{mn}(r,\phi) = \Gamma_{mn} J_m\left(X_{mn}\frac{r}{a}\right)\cos(m\phi) \tag{1.14a}$$

$$E_{mn}(r,\phi) = \Gamma_{mn} J_m\left(X_{mn}\frac{r}{a}\right)\sin(m\phi) \tag{1.14b}$$

where the phase term $e^{j(\omega t - \beta_{z,mn} z)}$ describing the propagation has been dropped. Eq. 1.14a and Eq. 1.14b describe odd and even modes, respectively. X_{mn} is the n-th root of a Bessel function of order m, and r and ϕ are the radial and azimuthal transverse coordinates. The set is orthogonal and normalized, with factor $\Gamma_{mn} = \frac{1}{\sqrt{\pi} a J_1(X_{0n})}$ for modes with $m = 0$ and $\Gamma_{mn} = \frac{\sqrt{2}}{\sqrt{\pi} a J_{m-1}(X_{mn})}$ for $m \neq 0$. The propagation constant of the m-th, n-th mode is

$$\beta_{z,mn} = k\sqrt{1 - \left(\frac{X_{mn}}{ka}\right)^2},$$

where $k = 2\pi/\lambda$ is the propagation constant in vacuum.

Quasi-optical beam waveguides are used to propagate paraxial Gaussian beams (mainly the TEM_{00} mode) in free-space. Such beams are well-confined and show low angular divergence, and are solutions to the paraxial approximation of the Helmholtz equation. The theory of Gaussian beam propagation and transformation is described in detail in Chapter 2. Following the cylindrical coordinates used for LP_{mn} modes, we have for a TEM_{00} non-astigmatic mode traveling in the z-direction the following expression (dropping the

time dependence) [28]

$$E(r,z) = \sqrt{\frac{2}{\pi w^2}} \exp\left(-\frac{r^2}{w^2} - jkz - j\frac{\pi r^2}{\lambda R} + j\phi_0\right), \tag{1.15}$$

and for the general TEM_{mn} mode [29, 30]:

$$\begin{aligned} E_{mn}(r,\phi,z) = \sqrt{\frac{2}{\pi}}\sqrt{\frac{m!}{(m+|n|)!}}\frac{1}{w}\left(\frac{\sqrt{2}r}{w}\right)^{|n|} L_m^{|n|}\left(\frac{2r^2}{w^2}\right) \times \\ \exp\left(-\frac{r^2}{w^2} - jkz - j\frac{\pi r^2}{\lambda R} + j(2m+|n|+1)\phi_0 + jn\phi\right), \end{aligned} \tag{1.16}$$

which has already been normalized. $L_m^{|n|}\left(\frac{2r^2}{w^2}\right)$ is the generalized Laguerre polynomial with $m \geq 0$ integer radial index and n azimuthal index. The electric field notation has been adapted to be similar to the LP_{mn} convention. The beam radius, the radius of curvature and the Gouy phase shift are defined as

$$w(z) = w_0\sqrt{1 + \left(\frac{\lambda z}{\pi w_0^2}\right)^2}, \tag{1.17a}$$

$$R(z) = z + \frac{1}{z}\left(\frac{\pi w_0^2}{\lambda}\right)^2, \tag{1.17b}$$

$$\phi_0(z) = \arctan\left(\frac{\lambda z}{\pi w_0^2}\right). \tag{1.17c}$$

Fig. 1.6 shows the cross section of a Gaussian beam and its main parameters.

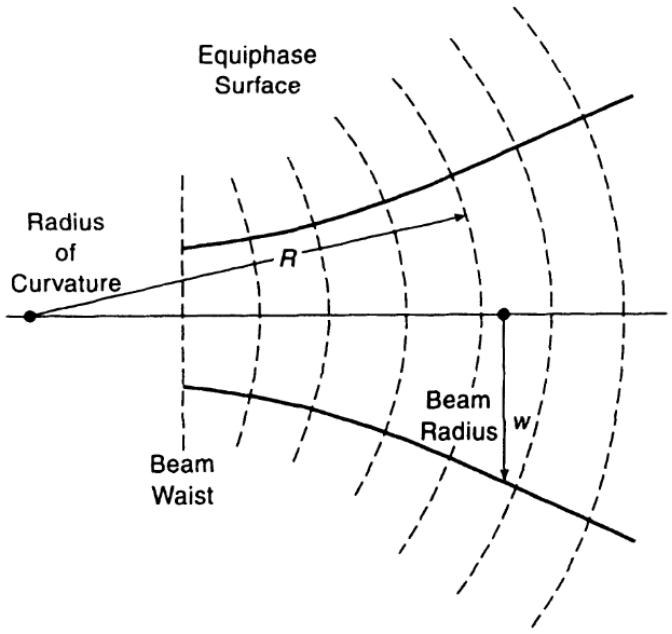


Figure 1.6: Cross section of a Gaussian Beam, showing the radius of curvature and the beam radius as it diverges [28].

QO transmission lines are capable of transmitting several high-power quasi-optical beams while maintaining high mode purity, broadband transmission and low losses. Losses depend only on beam truncation at the surface of the reflectors and finite conductivity [31]. In quasi-optical systems, the radius of a reflector is usually chosen to be at least two times the local beam radius, ensuring that 99.97% of the power is reflected. The power loss due to truncation is given by the simple formula $P_{\text{loss}} = P_0 e^{-D^2/(2w^2)}$ for the TEM_{00} mode [28], where D is the diameter of the reflector and P_0 is the input power. Fusion experiments usually require a large number of MW-class power beams to be launched into the plasma chamber. To avoid running several individual transmission lines in parallel, a single multiple-beam (MB) transmission line can be implemented using a system of oversized focusing mirrors [32]. The main advantages of using a single MB waveguide are the substantial reduction of the total required mirror surface area and the avoidance of multiple bulky systems that require independent alignment. Various configurations can be adopted. For instance, a series of four confocal mirrors with the same focal length is able to reconvert spurious modes generated at the mirrors back into the fundamental mode, provided an optimal "square arrangement" is chosen, such as a "zigzag" configuration. A visual comparison between quasi-optical single-beam and multi-beam transmission lines is shown in Fig. 1.7.

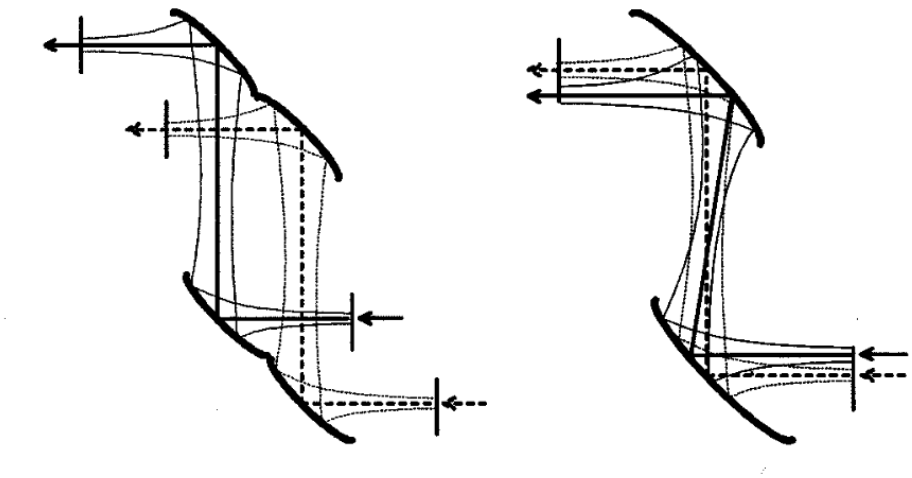


Figure 1.7: Sketch of quasi-optical parallel beam waveguides (left) and a multiple-beam waveguide (right) [32].

The excitation of higher-order Gaussian modes cannot be entirely avoided because the beams travel off-axis; consequently, the local curvature of the shared MB mirror cannot be perfectly matched to the phase front of each individual beam, leading to optical aberrations. Optimal arrangements are thus able to maintain a high mode purity by letting the higher-order modes interfere destructively. Moreover, the geometrical parameters of the MB reflector can be extensively optimized to minimize the total transmission losses. An example of a multi-beam transmission line is the one designed for the Divertor Tokamak Test (DTT) ECRH system. After exiting the gyrotrons, the individual beams are directed into the MB transmission line using combiner mirrors. At the end of the line, each beam is individually routed to its specific port via splitting mirrors and circular corrugated waveguides.

1.2.3. Launching Systems

At the end of a transmission line, EC beams are launched into the plasma through specific ports of the vacuum vessel. The tokamak and the transmission line are typically separated by a vacuum barrier window, which prevents tritium and other plasma material from traveling towards the transmission line. To ensure efficient coupling to the O- or X-modes of the plasma and localized absorption of power, these launchers must be able to deliver well-collimated beams with a precise direction and polarization. Front-steering (FS) launchers are typically designed using a combination of a fixed focusing mirror and a steerable planar mirror, as shown in Fig. 1.8 for the DTT ECRH launchers.

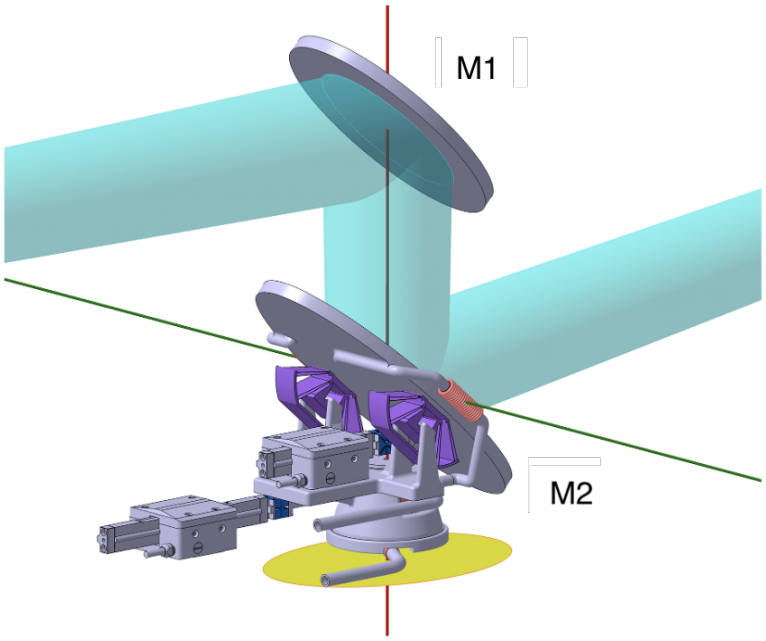


Figure 1.8: Fixed focusing mirror (M1) and steerable flat (M2) mirror of DTT front-steering launchers [33].

These mirrors are subjected to significant thermal loads on their surfaces due to microwave ohmic losses, plasma radiation and nuclear heating [33], so water cooling systems must be designed to prevent severe thermal deformations. As an alternative to front-steering designs, remote-steering (RS) antennas can be employed. These launchers have limited angular range and radiate broader beams, but have the advantage of being located far from the plasma, which guarantees easier maintenance and reliability. RS launchers are based on overmoded corrugated rectangular waveguides with specific lengths. A steered EC wave at the input of the waveguide maintains the same angle, phase and amplitude at output of the waveguide [34]. Steering launchers are placed at different positions of the tokamak chamber, and can inject the beams in a limited range of poloidal and toroidal angles. Depending on the plasma operation, it is often necessary to adjust the launching angles in real-time to address specific tasks and control plasma parameters [35]. For example, ITER has equatorial launchers which are used for heating, current drive and profile tailoring, while the upper launchers are used to control plasma instabilities.

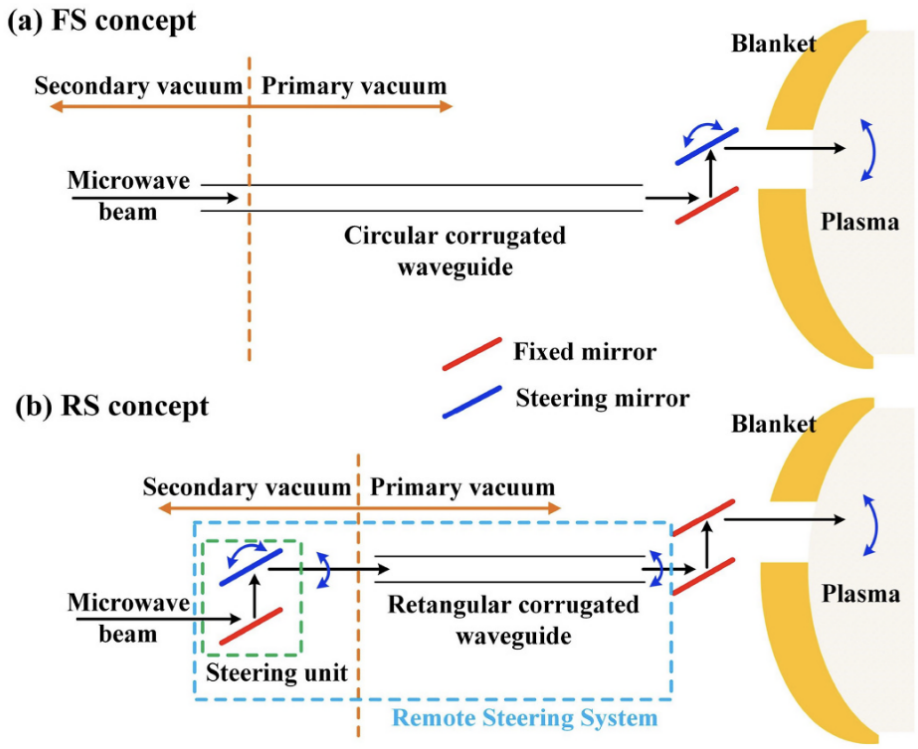


Figure 1.9: Conceptual schemes of (a) front-steering (FS) launchers and (b) remote-steering (RS) launchers for ECRH systems [34].

1.2.4. Power Diagnostic Techniques

Power monitoring techniques are essential to ensure the proper functioning of high-power microwave systems. In particular, these techniques are needed to achieve three main purposes [36]: monitoring the performance of microwave sources, protecting the microwave source if a high amount of power is reflected toward it, and measuring the power delivered to a load. Corrugated waveguides employ miter bends with coupling holes or diffraction gratings, while quasi-optical transmission lines usually employ grating couplers designed as diffraction grating mirrors. Both techniques couple a fraction of the input beam power to secondary waveguides in order to retrieve fundamental beam characteristics such as power, offset, tilt, polarization and mode purity. Misalignment of the input beam in oversized corrugated waveguides can cause excitation of higher-order modes. As shown in [37], a tilt of the input beam or an offset of the beam entering a corrugated waveguide can easily excite the $LP_{11}^{(e/o)}$ modes, while a mismatch of the radius of the input beam can excite axially symmetric modes such as LP_{02}. Different configurations can be adopted to measure power with arrays of hole couplers. For example, in the J-TEXT ECRH system,

a multi-hole directional coupler for measuring the power of a 105 GHz/500 kW gyrotron has been studied [38]. The presence of spurious modes can be detected by measuring the variation of the coupling into a specific port, compared to the expected coupling of the LP_{01} mode. This method shows that the coupling coefficient is a function of the phase difference between the fundamental mode and the spurious modes, due to different propagation constants. The structure of a miter-bend directional coupler with its main components is shown in Fig. 1.10.

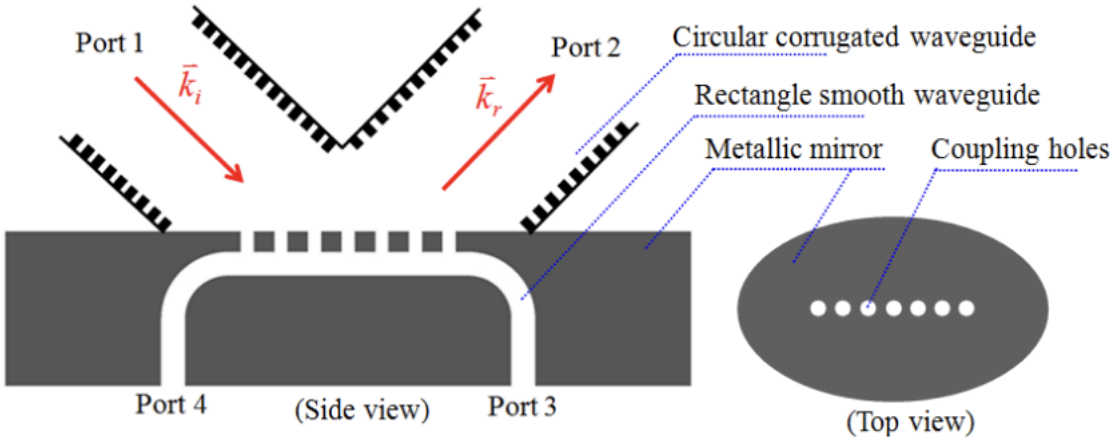


Figure 1.10: Schematic representation of a miter-bend directional coupler [39].

More complex configurations like those studied for the ASDEX-Upgrade ECRH system [37, 40] employ an array of leaky wave antennas made of hole couplers. A desired mode amplitude is measured by weighting the sampled signals to cancel the contribution of the other propagating modes. In general, with N-port directional couplers it is possible to resolve up to N propagating modes, if the hole arrays are placed to couple the field in appropriate positions. As the hole couplers may be sensitive to polarization, a polarizer is usually installed before reaching the miter bend. Miter bends can also cause mode conversion, but this issue does not depend on the alignment of the input beam, but rather on the geometrical parameters of the holes and on the geometrical discontinuity introduced by the bend. Real-time monitoring of the polarization is also of fundamental importance as it affects the propagation and absorption of the EC beam in the plasma. A notable example of a polarization monitor with hole couplers is the one designed for the LHD ECRH system [41], where two arrays of hole couplers are used to measure the two orthogonal signals. The main objective is to retrieve the polarization angle α and ellipticity angle β, and thus determine the state of polarization of the wave. An arbitrary

state of polarization can be described by the superposition of two orthogonal linear states of polarization, for example along the x- or y-axes:

$$E_x = E_{0,x} e^{j\Phi_x} \tag{1.18a}$$

$$E_y = E_{0,y} e^{j\Phi_y} \tag{1.18b}$$

where $E_{0,x}$ and $E_{0,y}$ are the wave amplitudes, and $\delta = \Phi_y - \Phi_x$ is the phase difference. The relationship between these field components and the polarization parameters is given by [42]:

$$\tan(2\alpha) = \tan(2\gamma)\cos\delta \tag{1.19a}$$

$$\sin(2\beta) = \sin(2\gamma)\sin\delta \tag{1.19b}$$

where $\gamma = \arctan(E_{0,y}/E_{0,x})$.

Quasi-optical metallic grating reflectors are a direct solution to implement directional couplers in quasi-optical transmission lines. Grating patterns are milled on planar or concave reflectors placed along the transmission line. These devices are designed to diffract a small fraction of the power into a specific diffraction order (typically the -1st or +1st order) while the main beam is specularly reflected (0th order). The coupling efficiencies depend on the geometrical properties of the grooves, such as the period, the depth and the shape. The diffracted beam is typically focused into a horn antenna, and from its properties it is possible to monitor the power and the alignment [43]. Polarization states are harder to monitor because gratings usually produce diffracted orders with non-trivial cross-polarization. Focusing of the beam can be achieved by using a concave grating coupler and by placing secondary concave mirrors along the direction of the diffracted beam. Aperiodic grating patterns are also a possible solution to modify the shape and phase front of the diffracted beam. The theory of grating reflectors is explored in depth in Chapter 2, and mode-matching methods to design grating couplers are described in Chapter 3. For quasi-optical TEM_{00} beams we can express the power coupling coefficient with respect to a desired Gaussian beam, in terms of beam parameters at an arbitrary reference plane. The one-dimensional power coupling coefficients are expressed as three main contributions, depending on the beam radii (w_a, w_b) and radii of curvature (R_a, R_b), tilt θ_t and offset d_0 along a specific transverse dimension of the input beam E_a and the desired beam E_b [28, 44]:

$$\eta_{\text{beam}} = \frac{2}{\sqrt{(w_b/w_a + w_a/w_b)^2 + (\pi w_a w_b/\lambda)^2(1/R_b - 1/R_a)^2}} \tag{1.20a}$$

$$\eta_{\text{tilt}} = \exp\left(-\frac{\theta^2}{\theta_{\text{t}}^2}\right) \tag{1.20b}$$

$$\eta_{\text{off}} = \exp\left(-\frac{d_0^2}{d_{\text{off}}^2}\right) \tag{1.20c}$$

where θ_{t} and d_{off} are referred to as the tilt tolerance angle and the lateral offset distance, respectively, using the convention of [44]:

$$\theta_{\text{t}} = \frac{\lambda\sqrt{2}}{\pi\eta_{\text{beam}}\sqrt{w_a^2 + w_b^2}} \tag{1.21a}$$

$$d_{\text{off}} = \frac{\sqrt{2}}{\eta_{\text{beam}}\sqrt{\frac{1}{w_a^2} + \frac{1}{w_b^2} + \left(\frac{\pi w_a}{\lambda R_a}\right)^2 + \left(\frac{\pi w_b}{\lambda R_b}\right)^2}} \tag{1.21b}$$

The total power coupling coefficient is the product of the one-dimensional coupling coefficients for the two orthogonal transverse axes (x and y), since a simple astigmatic Gaussian beam can always be decomposed into two orthogonal spatial contributions $E_a = E_{a,x}(x,z)E_{a,y}(y,z)$:

$$\eta_{\text{tot}} = (\eta_{\text{beam}}\eta_{\text{tilt}}\eta_{\text{off}})_x \cdot (\eta_{\text{beam}}\eta_{\text{tilt}}\eta_{\text{off}})_y \tag{1.22}$$

Under conditions of perfect alignment, a coupling efficiency of less than one implies a conversion of the fundamental mode into higher-order modes.

Finally, an alternative method to measure the total EC power emitted by gyrotron sources, particularly during testing, calibration, and conditioning phases, is the use of calorimetric loads [45]. These devices typically consist of spherical or cylindrical metallic cavities (often copper, aluminum, or stainless steel) whose internal surfaces are coated with microwave-absorbing materials, specifically designed for different high-power and pulse length applications. Microwave energy is converted into thermal energy which is transmitted to a water circuit that measures the average power and cools the system. As the measurement is done over time, it does not require the signal processing effort of the hole and grating couplers, but it is not able to capture real-time variations of the beam power. An example of a calorimetric matched load is the one designed for the FTU ECRH system

[46, 47]. When an input LP_{01} or TEM_{00} mode enters through the entrance port of the calorimeter, it propagates towards a spreading mirror placed at the opposite side of the sphere, directly facing the entrance port, as shown in Fig. 1.11. This mirror reflects a diverging beam onto the interior surface of the cavity. Its shape is precisely optimized for a given set of input beam parameters to ensure uniform power absorption across the walls while minimizing any power reflected back toward the entrance port. A correct design of the calorimeter is essential to avoid arcing of the transmission line or damage to the gyrotron sources due to back-reflected radiation. Safe operation requires that the ratio of power traveling back through the entrance port to the total input power is extremely low. This isolation can be improved by decreasing the reflectivity of the inner walls or by increasing the cavity diameter, though these parameters must be carefully balanced against the requirements for absorption uniformity and overall compactness of the device.

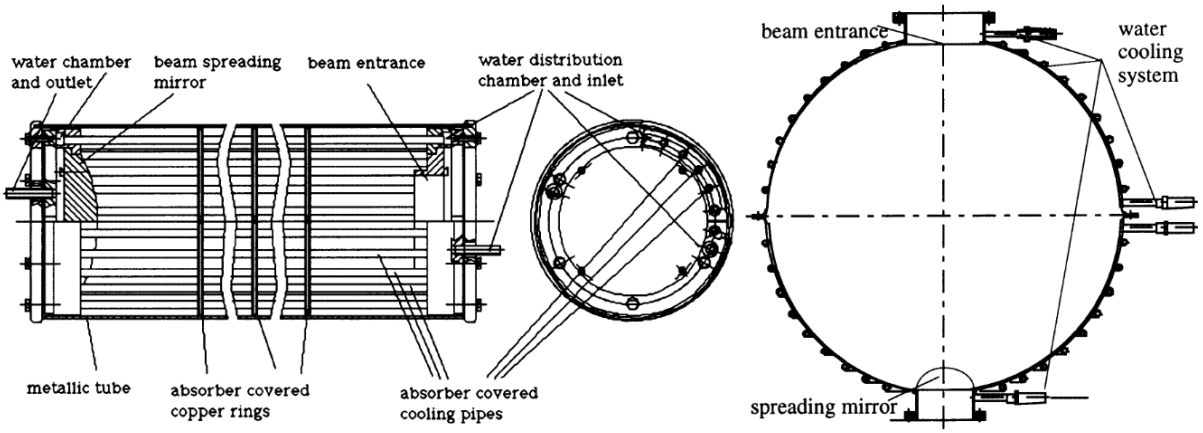


Figure 1.11: Schematic representation of cylindrical (left) and spherical (right) calorimetric loads [46].

1.3. Fusion Experiments

Fusion experiments have been designed ever since the construction of the first tokamak at the Kurchatov Institute of Atomic Energy in Moscow in the 1950s. The main goal driving research has always been to achieve energy production from fusion reactions. However, experimental fusion devices have faced significant problems in confining fusion plasmas and achieving ignition; therefore, there has been continuous development in their design, diagnostics, and operation [48]. To overcome these engineering challenges, many fusion experiments have been developed throughout the years, pushing applied and fundamental fusion research to interdisciplinary areas such as mechanical and microwave engineering. Currently, the main fusion device being built is ITER, together with the DEMO Oriented

Neutron Source (IFMIF-DONES) accelerator-based neutron source, which will be used to test and validate neutron-resistant materials. DEMO will be the next step to produce electricity for the first time through self-sufficient fusion reactions [4]. To maximize the success and safety of DEMO operation, fusion experiments such as DTT are being newly built or upgraded.

1.3.1. Divertor Tokamak Test (DTT)

DTT is a fusion experiment currently under construction at the ENEA research center in Frascati, Italy, focused on testing reliable solutions for the power exhaust of fusion plasmas. In particular, it will be testing different divertor concepts and various magnetic configurations compatible with those planned for DEMO [5]. The ECRH system is the main heating source [49], providing up to 32 MW out of a total 45 MW of additional heating, which also includes ICRH and NBI systems. Thanks to its flexibility, the ECRH system can assist with numerous tasks during different plasma phases, such as improving pre-ionization to initiate the plasma, building up temperature, stabilizing the plasma, tailoring current and temperature profiles, and cleaning the tokamak wall during plasma restart operations [5]. DTT is designed with a modular layout comprising the Gyrotron Hall, the evacuated quasi-optical transmission line, and the Torus Hall, as shown in Fig. 1.12.

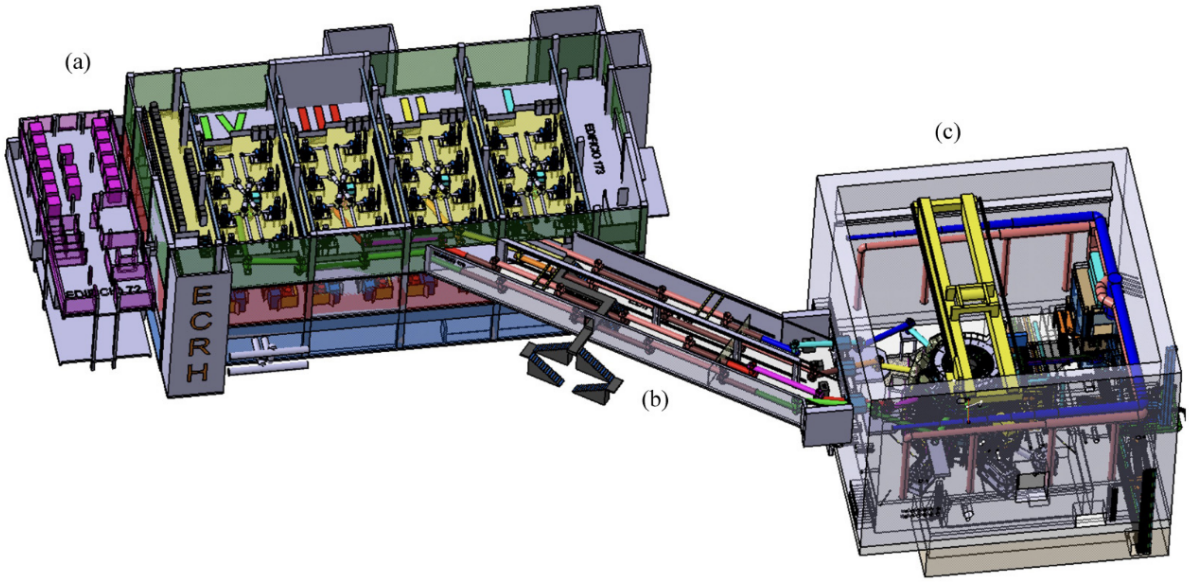


Figure 1.12: Graphical representation of the ECRH system of DTT: (a) Gyrotron Hall, (b) Quasi-optical evacuated transmission lines, (c) Torus Hall [50].

Great attention has been paid to making the system as flexible, safe and reliable as pos-

sible. The Gyrotron Hall consists of 4 clusters of 8 gyrotrons each, operating at 170 GHz for 100 s pulse lengths with output powers up to 1.5 MW. To optimize space and avoid mutual magnetic interference, the gyrotrons are arranged in two rows with a 5 m distance between each unit. The power delivered by clusters can be dynamically modulated depending on the requirements of the specific plasma operational phase. Gyrotron output ports are connected through single-beam (SB) quasi-optical transmission lines to combiner mirrors. SB lines are composed of a focusing mirror and a polarizer, in order to enter the multi-beam transmission line with a desired polarization (chosen to minimize ohmic losses). For each cluster of gyrotrons, there is a MB waveguide composed in "square arrangement", with 8 mirrors, capable of supporting up to 8 EC beams of 1.5 MW each. The transmission line concept is based on the one installed at the ECRH system of the W7-X stellarator, and is designed to be compact and minimize mode conversion losses [51]. At the exit of the MB transmission line, splitting mirrors redirect EC waves to launchers using a focusing mirror and two polarizers, employed to optimize the coupling to the plasma. Beams are divided towards two antennas, six into the equatorial port, and two into the upper port. A 63.5 mm circular waveguide of properly tuned length connects the single beam transmission lines to the front-steering launcher mirrors, coupling the LP_{01} and LP_{02} modes with efficiency $\eta = 99.85\%$. In this tokamak, between the launchers and the plasma there are no vacuum barrier windows, and the connection is only regulated by gate valves that open only during ECRH pulses. The total length of the transmission lines ranges between 84 to 137 m depending on the cluster, with major and minor diameters of the copper mirrors ranging from 102 to 356 mm for SB lines and from 650 to 1076 mm for the MB lines. At the entrance of the MB line, the Gaussian beams are designed to have a waist size of approximately 25 mm in order to allow proper spatial separation at the combiner mirrors [52]. At the same time, the splitting mirrors are placed where the beams exiting from the MB line reach the minimum beam radius ~ 25 mm and have the maximum separation. The main losses of the transmission lines are due to ohmic losses, beam truncation at the reflectors, generation of spurious modes, misalignments and thermo-mechanical deformation of components due to heat [53].

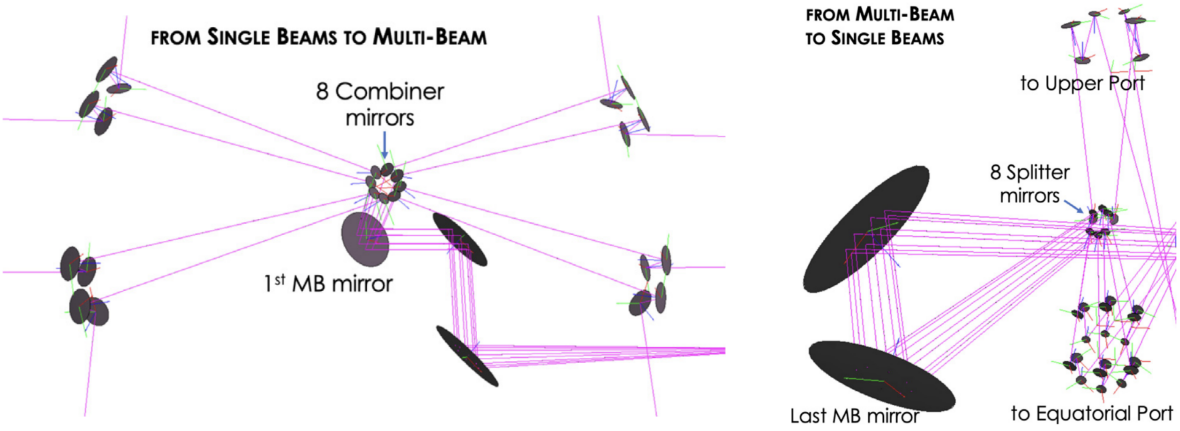


Figure 1.13: Graphical representation of the combiner mirrors (left) and splitter mirrors (right) of a multi-beam transmission line [54].

2 | Grating Reflectors Theory and Applications

2.1. Diffraction Gratings Theory

A diffraction grating can be defined, in general terms, as any transmitting or reflecting structure that exhibits a periodic variation of geometrical and material characteristics. If this periodicity is comparable to the wavelength of an incident wave, the grating acts as an obstruction that scatters electromagnetic energy [55]. This interaction generates a set of diffraction orders (including a specular reflection), whose direction, polarization, and energy are determined by the grating design. The wavelength dependence allows these structures to be used as spectroscopic instruments. Moreover, diffraction gratings can be designed to cover a wide range of applications, such as optical filters, directional couplers, polarizers, and mode converters [56]. Periodic photonic structures are also widely observed in nature. Recent studies have shown that natural grating-like structures give rise to optical effects such as iridescence and the blue halo effect, which may have important biological functions including enhancing communication between plants and pollinators [57, 58]. Diffraction gratings can be analyzed using the so-called grating equation, which, for one-dimensional periodicity and classical mounting (plane of incidence perpendicular to the grooves), is expressed as:

$$\sin\theta_m + \sin\theta_{\text{in}} = m\frac{\lambda}{a}, \tag{2.1}$$

where $m = 0, \pm1, \pm2, \ldots$ is the diffraction order, a is the grating period, λ is the wavelength of the incoming wave, θ_{in} is the angle of incidence, and θ_m is the angle of diffraction, as shown in Fig. 2.1.

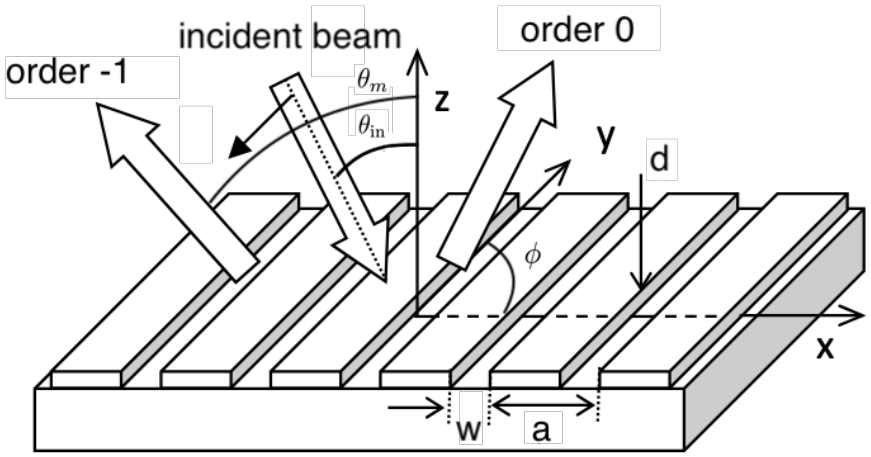


Figure 2.1: Principle of a planar lamellar grating reflector, with grating period a, width w and depth d. The 0th order is the specular reflection, and the -1st order is a diffracted lobe [56].

The specific diffraction angles predicted by this equation correspond to the scattered waves that remain in phase and interfere constructively, constituting propagating orders. Waves that cannot propagate are called evanescent orders. We can expand the grating equation into a more general law that is valid for conical diffraction and two-dimensional periodicity. The wavevector $\mathbf{k}^+$ of an incident plane wave with angles θ (polar angle) and ϕ (azimuthal angle) is defined as:

$$\mathbf{k}^+ = -\boldsymbol{i}_r k = \boldsymbol{i}_x k_x^+ + \boldsymbol{i}_y k_y^+ + \boldsymbol{i}_z k_z^+ = -\boldsymbol{i}_x k \sin\theta\cos\phi - \boldsymbol{i}_y k \sin\theta\sin\phi - \boldsymbol{i}_z k\cos\theta, \quad (2.2)$$

where k_x^+ and k_y^+ are the tangential components of the incident wavevector and k_z^+ is the longitudinal component, using the coordinate system shown in Fig.2.1. These incident components are related to those of the scattered wavevector $\mathbf{k}_{mn}$:

$$k_{xm} = k_x^+ + \frac{2m\pi}{a}, \quad (2.3a)$$

$$k_{yn} = k_y^+ + \frac{2n\pi}{b}, \quad (2.3b)$$

$$\mathbf{k}_{mn} = \boldsymbol{i}_x k_{xm} + \boldsymbol{i}_y k_{yn} + \boldsymbol{i}_z k_{z,mn}, \quad (2.3c)$$

where m and n are the indices of the diffracted order (m, n), and the longitudinal com-

ponent is determined by the dispersion relation:

$$k_{z,mn} = \sqrt{k^2 - k_{xm}^2 - k_{yn}^2}. \tag{2.4}$$

The longitudinal component of the wavevector must be either real and positive (representing propagating orders), or purely imaginary and negative (representing exponentially decaying evanescent orders). In general, based on the wavevector equations, we can distinguish three approximate operating regimes: for $a < \lambda$, only the specular reflection propagates; for $a \sim \lambda$, the specular reflection is accompanied by a single diffraction order ($+1$ or -1); and for $a > \lambda$, multiple diffraction orders are generated. The exact thresholds depend on the angle of incidence of the incoming wave. Since our main application involves grating couplers for ECRH systems, we aim to produce only one propagating diffraction order and the specular reflection. Thus, in Chapter 3, we will restrict our analysis to 1D periodic corrugations, invariant along the y-axis ($n = 0$), with a grating period $a \sim \lambda$ along the x-axis. Several shapes can be chosen for the design of a grating reflector, as shown in Fig. 2.2. Relevant geometrical factors in determining the grating efficiency are the wavelength to grating period ratio (λ/a), the groove depth to grating period ratio (d/a) and, for lamellar gratings, the duty cycle (w/a) [59].

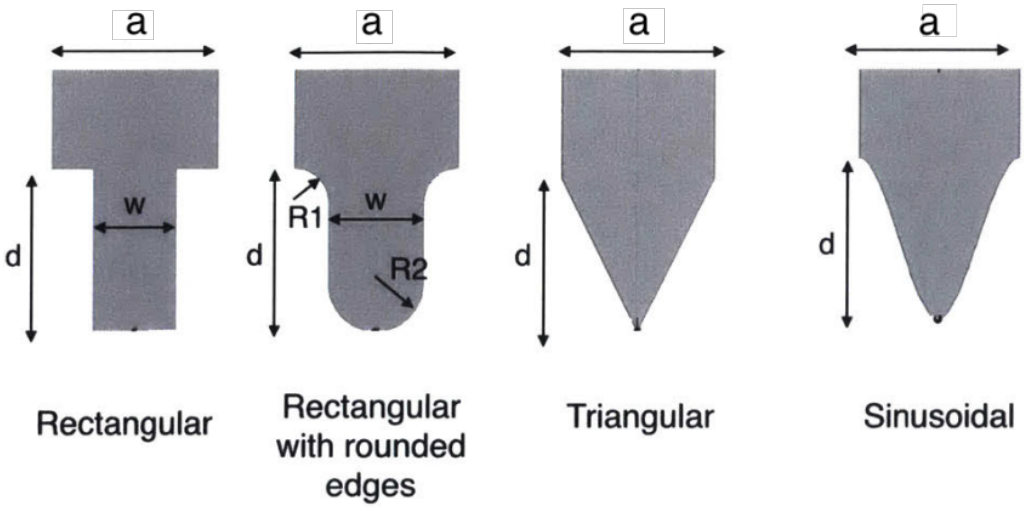


Figure 2.2: Example of groove shapes: rectangular (lamellar), rectangular with rounded edges, triangular and sinusoidal [60].

For high-power applications, an optimal shape of the metallic grooves reduces arcing and ohmic losses. In particular, arcing is mitigated by rounded edges, while ohmic losses are minimized by wide grooves and thin ridges [61].

Grating efficiency cannot be calculated from the grating equation alone, but requires the scattering amplitudes to be derived by numerical methods [56]. Efficiency depends not only on the geometry of the grating but also on the incoming polarization, which can be decomposed into its TE and TM components. In conical mountings (plane of incidence not perpendicular to the grooves), cross-polarization between TE and TM orders is generally not negligible. The macroscopic geometry of the grating substrate also plays an important role in shaping the overall scattered beam profile. In practice, gratings are typically manufactured in either planar or concave configurations. The latter option is used to take advantage of the focusing properties of concave mirrors. Imaging properties can also be introduced by spatially varying the geometrical parameters of the grating, such as the period or depth, to shape the scattered wavefront or reduce optical aberrations [62, 63].

2.1.1. Numerical Methods for Grating Efficiency

Many numerical methods can be employed for the analysis and design of periodic structures such as diffraction gratings [56]. No universal method exists, and depending on the complexity, the materials, and the application, a given method may solve a particular scattering problem more efficiently than others. Nevertheless, there are some fundamental properties of periodic structures that are common to every technique. An electromagnetic field interacting with a periodic structure can be expanded into a Fourier-Floquet series:

$$E(x,y,z) = \sum_{m=-\infty}^{\infty} \sum_{n=-\infty}^{\infty} S_{mn}(z) e^{-j(k_{xm}x + k_{yn}y)}, \tag{2.5}$$

where $S_{mn}(z)$ represents the z-dependent amplitude of each Floquet harmonic. This generalized expansion is particularly useful in modal methods to obtain closed form solutions for the scattering amplitudes. In free space, we consider a similar formulation (known as Rayleigh expansion), to describe the reflected (or incident) fields. It consists of a superposition of independent plane waves representing both propagating and evanescent diffraction orders, with constant reflection (or incidence) amplitudes:

$$E(x,y,z) = \sum_{m=-\infty}^{\infty} \sum_{n=-\infty}^{\infty} E_{mn} e^{-j\mathbf{k}_{mn}\cdot\mathbf{r}}. \tag{2.6}$$

To validate the results obtained via the Mode-Matching Method employed in Chapter 3, rigorous electromagnetic simulations were performed using Ansys High-Frequency Structure Simulator (HFSS) [64], a commercial solver based on the Finite Element Method (FEM). HFSS is highly suited for diffraction grating analysis, as it allows the modeling

of periodic unit cells through periodic boundary conditions and plane-wave excitation via Floquet ports.

2.2. Quasi-Optical Theory

Similar to plane waves, paraxial Gaussian beams propagate in a well-defined direction and remain highly collimated, yet they exhibit a transverse Gaussian variation. Gaussian waves are solutions of the paraxial wave equation [28]

$$\frac{\partial^2 u}{\partial x^2} + \frac{\partial^2 u}{\partial y^2} - 2jk\frac{\partial u}{\partial z} = 0, \tag{2.7}$$

where u is the complex amplitude of a wave traveling along the positive z-direction, described by the function $E(x, y, z) = u(x, y, z)e^{j(\omega t - kz)}$. For simplicity the time-dependent term $e^{j\omega t}$ has been dropped in the following equations. The paraxial wave equation is derived from the Helmholtz equation assuming that axial variations of u are small over a distance comparable to λ and are negligible with respect to transverse variations. A quantitative way to define a well-collimated Gaussian beam is through the Rayleigh range (or confocal distance):

$$z_R = \frac{\pi w_0^2}{\lambda}. \tag{2.8}$$

Beams traveling at distances $z \ll z_R$ (near field) from their beam waist remain well-collimated because they propagate without growing significantly ($w \leq \sqrt{2}w_0$), while for $z \gg z_R$ (far field) beams start to diverge, with both the beam radius and radius of curvature growing linearly with the distance. The paraxial Gaussian beam approximation should be used with well-defined beams without excessive divergence. The spreading of a Gaussian can be quantified by the far-field divergence angle, which, as $z \to \infty$, becomes:

$$\theta_R = \arctan\left(\frac{\lambda}{\pi w_0}\right). \tag{2.9}$$

From this, it can be observed that beams with a smaller beam waist with respect to their wavelength spread more widely, while beams with a larger waist have a low angular divergence, remain well-confined and have a larger Rayleigh range. A spreading up to $\theta_R = 20°$ is considered a good upper boundary for a well-defined or paraxial beam [28], and corresponds to a ratio $w_0/\lambda \geq 0.9$. For ECRH systems employing microwave sources at 170 GHz, this ratio is largely satisfied as $w_0 \simeq 16$ mm (typical beam waist at the exit of ECRH gyrotrons), and $\lambda \simeq 1.76$ mm yield

$$\frac{w_0}{\lambda} = 9.1 > 0.9, \tag{2.10a}$$

$$\theta_{R,\mathrm{ECRH}} = 2^\circ \ll 20^\circ. \tag{2.10b}$$

This means that ECRH TEM_{00} modes can be treated within the quasi-optical framework, since they remain well-defined throughout their propagation.

2.2.1. ABCD matrices

In order to preserve quasi-optical propagation and avoid excessive growth of the beam dimensions, we can transform the Gaussian beam properties by using quasi-optical elements such as concave reflectors and grating couplers. Similar to geometrical optics, Gaussian beam propagation and transformation can be described in the paraxial limit through a set of transfer matrices. A practical way to handle calculations with Gaussian beams is by using the two-dimensional Cartesian formulation

$$E(x,y,z) = \sqrt{\frac{2}{\pi w_x w_y}} \exp\left(-\frac{x^2}{w_x^2} - \frac{y^2}{w_y^2} - jkz - j\frac{\pi x^2}{\lambda R_x} - j\frac{\pi y^2}{\lambda R_y} + j\frac{\phi_{0y}}{2} + j\frac{\phi_{0x}}{2}\right). \tag{2.11}$$

In this case, Eqs. 1.17 are defined separately for the x-axis (with beam waist w_{0x}) and y-axis (with beam waist w_{0y}). Compared to Eq. 1.15, this expression allows one to define different values for the beam waists and analyze transformations in two independent transverse dimensions.

Gaussian beam transformation can be described by means of the ABCD law. While geometrical optics applies ABCD matrices to the ray height and slope, Gaussian beam transformations are applied to the complex beam parameter q, defined as [28, 65]:

$$\frac{1}{q_{\mathrm{in}}} = \frac{1}{R_{\mathrm{in}}} - j\frac{\lambda}{\pi w_{\mathrm{in}}^2}. \tag{2.12}$$

This gives an alternative expression for the complex amplitude of the Gaussian beam:

$$E(x,y,z) \propto \exp\left[-\frac{jk}{2}\left(\frac{x^2}{q_x} + \frac{y^2}{q_y}\right)\right]. \tag{2.13}$$

Beam transformations through these matrices apply in the same way to higher-order Gaussian modes, because the beam radius and the radius of curvature change in the same way for all modes. However, it is important to note that the phase shift is mode-dependent

and must be taken into account separately. The generic ABCD beam transformation can be expressed as:

$$q_{\text{out}} = \frac{A \cdot q_{\text{in}} + B}{C \cdot q_{\text{in}} + D}, \tag{2.14}$$

where the transfer matrix is defined as:

$$\mathbb{M} = \begin{bmatrix} A & B \\ C & D \end{bmatrix}. \tag{2.15}$$

In this framework, matrices for common optical elements, including diffraction gratings, can be derived [28]. Starting from an ABCD matrix, we can define separate matrices for the tangential and sagittal planes of propagation. Examples of matrices for ECRH-relevant quasi-optical elements are shown in Table 2.1.

Optical Element	**Tangential Plane**	**Sagittal Plane**
$\mathbb{M}_L$**: free space propagation**	$\begin{bmatrix} 1 & L \\ 0 & 1 \end{bmatrix}$	$\begin{bmatrix} 1 & L \\ 0 & 1 \end{bmatrix}$
$\mathbb{M}_R$**: tilted spherical mirror**	$\begin{bmatrix} 1 & 0 \\ -\frac{2}{R\cos\theta} & 1 \end{bmatrix}$	$\begin{bmatrix} 1 & 0 \\ -\frac{2\cos\theta}{R} & 1 \end{bmatrix}$
$\mathbb{M}_f$**: tilted ellipsoidal mirror**	$\begin{bmatrix} 1 & 0 \\ -\frac{1}{f_{\text{t}}\cos\theta} & 1 \end{bmatrix}$	$\begin{bmatrix} 1 & 0 \\ -\frac{\cos\theta}{f_{\text{s}}} & 1 \end{bmatrix}$
$\mathbb{M}_m$**: planar grating reflector**	$\begin{bmatrix} M & 0 \\ 0 & 1/M \end{bmatrix}$	$\begin{bmatrix} 1 & 0 \\ 0 & 1 \end{bmatrix}$
$\mathbb{M}_{mf}$**: curved grating reflector**	$\begin{bmatrix} M & 0 \\ -2/R_{\text{gt}} & 1/M \end{bmatrix}$	$\begin{bmatrix} 1 & 0 \\ -2/R_{\text{gs}} & 1 \end{bmatrix}$

Table 2.1: ABCD matrix representation for ECRH-relevant optical elements. $M = \frac{\cos\theta_{\text{out}}}{\cos\theta_{\text{in}}}$ is the anamorphic magnification factor. For spherical mirrors, R is the physical radius of curvature. For ellipsoidal mirrors, f_{t} and f_{s} are the focal lengths in the tangential and sagittal planes. For the curved grating, the effective radii of curvature are $R_{\text{gt}} = \frac{2\cos\theta_{\text{in}}\cos\theta_{\text{out}}}{\cos\theta_{\text{in}}+\cos\theta_{\text{out}}} R_g$ and $R_{\text{gs}} = \frac{2}{\cos\theta_{\text{in}}+\cos\theta_{\text{out}}} R_g$, where R_g is the physical radius of the grating [28, 66].

In order to compute the output beam radius and curvature radius, ABCD matrices must be multiplied from right to left in the order in which the elements are encountered. This means that the transformation of an incident Gaussian beam into a given diffraction order can be computed as (assuming classical mounting):

$$\mathbb{M}_{LmL}^{(T)} = \mathbb{M}_{L}^{\text{out}}\mathbb{M}_{m}^{(T)}\mathbb{M}_{L}^{\text{in}} = \begin{bmatrix} M & L_{\text{in}}M + L_{\text{out}}/M \\ 0 & 1/M \end{bmatrix}, \tag{2.16a}$$

$$\mathbb{M}_{LmL}^{(S)} = \mathbb{M}_{L}^{\text{out}}\mathbb{M}_{m}^{(S)}\mathbb{M}_{L}^{\text{in}} = \begin{bmatrix} 1 & L_{\text{in}} + L_{\text{out}} \\ 0 & 1 \end{bmatrix}, \tag{2.16b}$$

where θ_{in} is the incidence angle, θ_{out} is the diffraction angle, L_{in} is the incident propagation path, and L_{out} is the diffracted propagation path. As expected, for a propagation plane perpendicular to the grating grooves, anamorphic magnification occurs only in the tangential plane, as shown in Fig. 2.3.

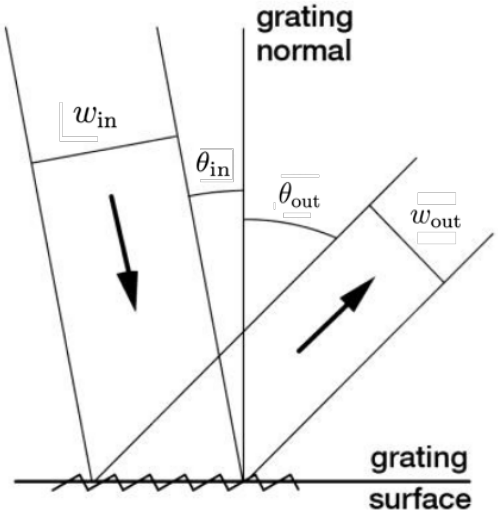


Figure 2.3: Anamorphic beam magnification from a diffraction grating (simplified using planar wavefronts) [67].

After an optical transformation, it is possible to derive the output beam radius w_{out} and the output radius of curvature R_{out} of the Gaussian beam from the resulting complex

beam parameter q_{out}:

$$w_{\text{out}} = \sqrt{\frac{\lambda}{\pi \mathfrak{Im}(-1/q_{\text{out}})}}, \tag{2.17a}$$

$$R_{\text{out}} = \mathfrak{Re}(1/q_{\text{out}})^{-1}. \tag{2.17b}$$

2.2.2. Tensor ABCD Law

Quasi-optical transmission lines of ECRH systems can include astigmatic beams and off-axis, curved optical elements. For this reason, it is sometimes difficult to work exclusively with ABCD matrices, and other generalizations may be more suitable to describe the optical system. A first generalization employs generalized beam matrices, or "ABCDGH matrices", which consist of 3x3 matrices with only 6 non-trivial elements [68, 69]. This method accounts for misalignments and off-axis optical elements, and makes it easy to distinguish astigmatic propagation along two orthogonal planes (tangential and sagittal). Compared to the standard ABCD law, which employs only the complex beam parameter q, an additional characteristic variable, the complex displacement parameter S, is employed [70]. Although this is a great improvement over traditional ABCD matrices, the limits of ABCDGH matrices emerge when it is necessary to describe off-plane propagation and general astigmatism. This is a common case when grating couplers are introduced in a quasi-optical transmission line, because higher diffraction orders become astigmatic and are diffracted in different directions relative to the main transmission line. The tensor ABCD law introduces 4x4 matrices that are able to describe orthogonal and non-orthogonal optical systems, including arbitrary optical transformations. These matrices were originally introduced in the literature for ray systems in two transverse directions [71]. ABCD tensors have the general form [72]:

$$\mathbb{M} = \begin{bmatrix} A_{xx} & A_{xy} & B_{xx} & B_{xy} \\ A_{yx} & A_{yy} & B_{yx} & B_{yy} \\ C_{xx} & C_{xy} & D_{xx} & D_{xy} \\ C_{yx} & C_{yy} & D_{yx} & D_{yy} \end{bmatrix} = \begin{bmatrix} \mathbb{M}_A & \mathbb{M}_B \\ \mathbb{M}_C & \mathbb{M}_D \end{bmatrix}, \tag{2.18}$$

where four sub-matrices $\mathbb{M}_A$, $\mathbb{M}_B$, $\mathbb{M}_C$ and $\mathbb{M}_D$ have been defined to simplify the notation. In order to use these matrices, a tensor formulation including two orthogonal directions must also be introduced for the complex beam parameter q [73]:

$$q_{3D}^{-1} = \begin{bmatrix} 1/q_{xx} & 1/q_{xy} \\ 1/q_{yx} & 1/q_{yy} \end{bmatrix}, \tag{2.19}$$

with $1/q_{xy} = 1/q_{yx}$. This expression is called the complex beam matrix for general astigmatic Gaussian beams, and is valid only for the TEM_{00} mode. In most cases, we can consider the input Gaussian beam aligned with the optical axis and neglect the off-diagonal elements. The expression to obtain the output beam matrix with the tensor ABCD law is analogous to the conventional one:

$$q_{3D,\text{out}}^{-1} = (\mathbb{M}_C + \mathbb{M}_D \cdot q_{3D,\text{in}}^{-1})(\mathbb{M}_A + \mathbb{M}_B \cdot q_{3D,\text{in}}^{-1})^{-1}. \tag{2.20}$$

The complex beam matrix may not be diagonal after a series of transformations. It should be noted that an arbitrary beam transformation can convert a simple astigmatic beam into a general astigmatic beam. For a general astigmatic beam, the isophotes (curves of constant intensity) and isophases (curves of constant phase) are different ellipses whose orientations change relative to each other during propagation, even though the overall direction of propagation remains the same [74, 75], as shown in Fig. 2.4.

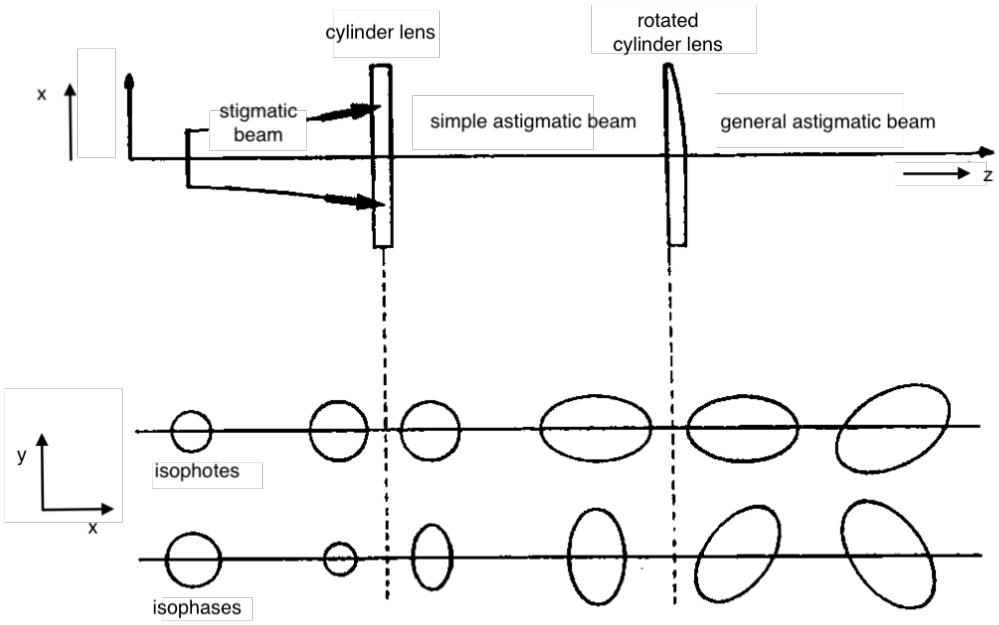


Figure 2.4: Example of variation of isophote and isophase ellipses during propagation through optical elements. A stigmatic beam becomes a simple astigmatic beam and then a general astigmatic beam [75].

The electric field of a general astigmatic fundamental Gaussian beam is given by [75]:

$$E(x,y,z) \propto \exp\left[-\frac{jk}{2}\left(\frac{x^2}{q_{xx}}+\frac{2xy}{q_{xy}}+\frac{y^2}{q_{yy}}\right)\right]. \tag{2.21}$$

It is possible to retrieve the major and minor axes of the ellipses if we extract from the complex beam matrix its real and imaginary parts:

$$W_{3D}^{-2} = -\frac{\pi}{\lambda}\mathfrak{Im}(q_{3D}^{-1}) = \begin{bmatrix} 1/w_{xx}^2 & 1/w_{xy}^2 \\ 1/w_{yx}^2 & 1/w_{yy}^2 \end{bmatrix}, \tag{2.22a}$$

$$R_{3D}^{-1} = \mathfrak{Re}(q_{3D}^{-1}) = \begin{bmatrix} 1/R_{xx} & 1/R_{xy} \\ 1/R_{yx} & 1/R_{yy} \end{bmatrix}. \tag{2.22b}$$

The relative angle $\Delta\theta$ between the major axes of the isophote and isophase ellipses can be retrieved directly from the components of the W_{3D}^{-2} and R_{3D}^{-1} tensors:

$$\Delta\theta = \frac{1}{2}\left[\arctan\left(\frac{2/w_{xy}^2}{1/w_{xx}^2 - 1/w_{yy}^2}\right) - \arctan\left(\frac{2/R_{xy}}{1/R_{xx} - 1/R_{yy}}\right)\right]. \tag{2.23}$$

This angle represents the degree of general astigmatism of the output Gaussian beam. The isophote and isophase ellipses share the same principal axes when $\Delta\theta = 0°$ or $90°$ (simple astigmatic beam).

By diagonalizing W_{3D}^{-2} and R_{3D}^{-1} it is possible to obtain the major and minor axes of the isophote (w_1^2,w_2^2) and isophase (R_1,R_2) ellipses. Matrices for free space propagation, focusing mirrors and grating reflectors are summarized in Table 2.2, including the planar grating reflector which is of great interest for the design of DTT grating couplers. In the tensorial ABCD law, its matrix $\mathbb{M}_{m,3D}$ applies the appropriate anamorphic magnification to the general case of conical diffraction. Being planar, the sub-matrix $\mathbb{M}_C$ has all zero elements, but it can be generalized to introduce focusing properties [76].

Optical Element	$\mathbb{M}_A$	$\mathbb{M}_B$	$\mathbb{M}_C$	$\mathbb{M}_D$
$\mathbb{M}_{L,\mathrm{3D}}$: free space propagation	$\begin{bmatrix} 1 & 0 \\ 0 & 1 \end{bmatrix}$	$\begin{bmatrix} L & 0 \\ 0 & L \end{bmatrix}$	$\begin{bmatrix} 0 & 0 \\ 0 & 0 \end{bmatrix}$	$\begin{bmatrix} 1 & 0 \\ 0 & 1 \end{bmatrix}$
$\mathbb{M}_{f,\mathrm{3D}}$: focusing reflector	$\begin{bmatrix} 1 & 0 \\ 0 & 1 \end{bmatrix}$	$\begin{bmatrix} 0 & 0 \\ 0 & 0 \end{bmatrix}$	$\begin{bmatrix} -1/f_x & 0 \\ 0 & -1/f_y \end{bmatrix}$	$\begin{bmatrix} 1 & 0 \\ 0 & 1 \end{bmatrix}$
$\mathbb{M}_{m,\mathrm{3D}}$: planar grating reflector	$\begin{bmatrix} M_\theta & 0 \\ M_\phi t_{\theta_{\mathrm{in}}} s_{\phi_{\mathrm{in}}} - M_\theta t_{\theta_{\mathrm{out}}} s_{\phi_{\mathrm{out}}} & M_\phi \end{bmatrix}$	$\begin{bmatrix} 0 & 0 \\ 0 & 0 \end{bmatrix}$	$\begin{bmatrix} 0 & 0 \\ 0 & 0 \end{bmatrix}$	$\begin{bmatrix} 1/M_\theta & t_{\theta_{\mathrm{out}}} s_{\phi_{\mathrm{out}}}/M_\phi - t_{\theta_{\mathrm{in}}} s_{\phi_{\mathrm{in}}}/M_\theta \\ 0 & 1/M_\phi \end{bmatrix}$

Table 2.2: Tensorial Matrix representation for ECRH-relevant optical elements [75–77]. For compactness, trigonometric functions are abbreviated as $c_x = \cos x$, $s_x = \sin x$, and $t_x = \tan x$. $M_\theta = c_{\theta_{\mathrm{out}}}/c_{\theta_{\mathrm{in}}}$ and $M_\phi = c_{\phi_{\mathrm{out}}}/c_{\phi_{\mathrm{in}}}$ the anamorphic magnification factors.

2.3. Applications of Grating Reflectors

Grating reflectors are fundamental components in the high-power quasi-optical transmission lines of modern magnetic confinement fusion experiments. The following examples analyze two distinct components designed for ECRH systems: the diagnostic grating coupler employed in the W7-X stellarator, and the grating polarizer developed for the DTT experiment.

2.3.1. W7-X Grating Coupler

As discussed in Chapter 1, the precise alignment of Gaussian beams is of great importance to ensure the efficient delivery of high-power EM waves to the plasma. Alignment diagnostics within quasi-optical transmission lines frequently employ grating couplers to generate a low-power image of the main beam via a specific diffraction order. A notable implementation of this technique is the alignment system designed for the W7-X stellarator [43]. This ECRH system employs 140 GHz gyrotrons to deliver up to 10 MW of continuous-wave power to the plasma. At the end of the multi-beam transmission lines, the Gaussian beams are divided by splitting mirrors and routed to individual launchers. A grating coupler machined onto a focusing mirror diffracts a small fraction of this power into a -1st or $+1$st diffraction order. This diffracted beam is subsequently coupled into a matched horn antenna and analyzed to monitor the angular and spatial alignment of the main beam. The experimental configuration described by Shi and Kasparek [43] is shown in Fig. 2.5.

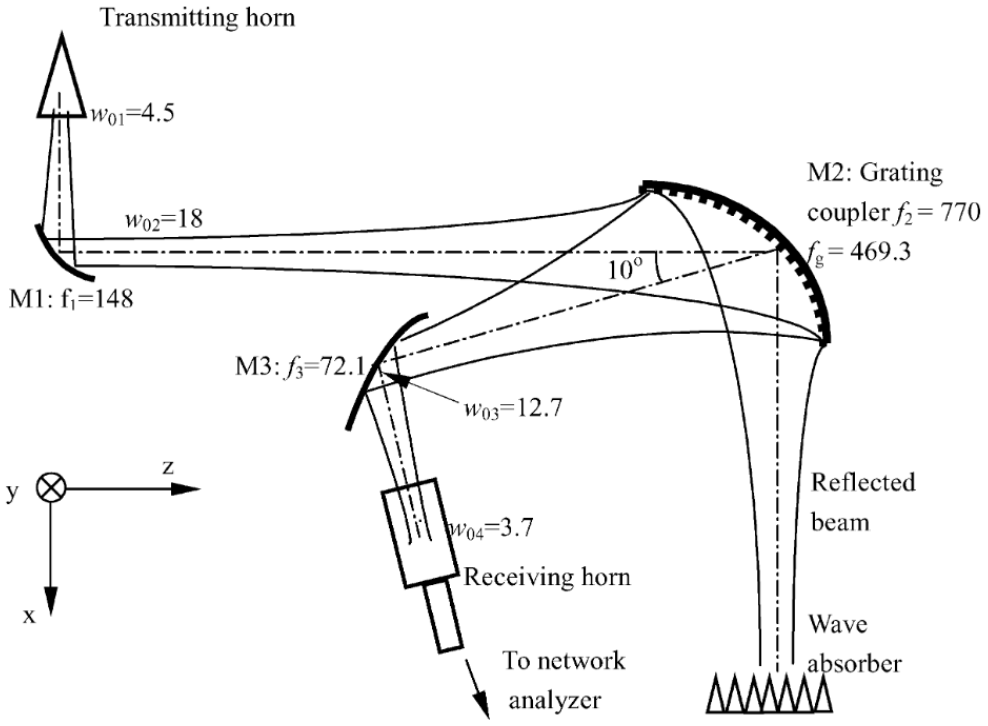


Figure 2.5: Experimental configuration of the W7-X grating coupler. M1 and M2 are off-axis ellipsoidal reflectors, and M3 is an off-axis paraboloidal reflector. The effective focal lengths and beam waists shown in the diagram are normalized to (mm).

This example serves as a benchmark to validate both the ABCD analytical model and the grating efficiency calculations performed in ANSYS HFSS. In order to simulate the power efficiency, the grating unit cell is modeled as a perfect electric conductor (PEC) placed in a vacuum. The excitation is assigned using a Floquet port and coupled periodic boundary conditions. The diffractive mirror surface is fabricated using a spherical milling tool with a radius of $R = 16$ mm. For a grating period of $a = 1.68$ mm on the x-axis, a shallow groove depth of $d \simeq 22$ μm is obtained. M2 is designed to have low distortion and low cross-polarization of the beam. The designed HFSS model confirms that these milling parameters precisely correspond to the reported groove depth. The HFSS model is shown in Fig. 2.6, for a reduced milling radius of $R = 2$ mm as 16 mm produces a depth that is too shallow to be resolved visually.

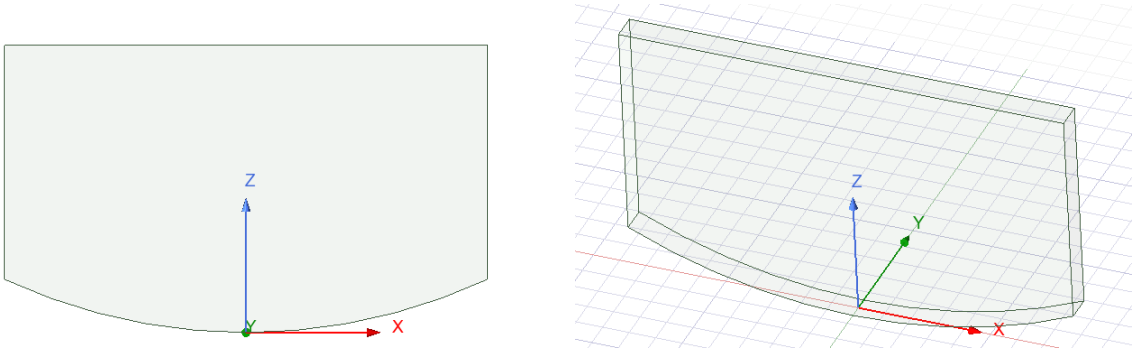


Figure 2.6: HFSS geometric model of the grating profile (depicted with a scaled milling radius of $R = 2$ mm for visualization purposes). The actual simulated profile utilizes $R = 16$ mm and $a = 1.68$ mm, yielding the nominal groove depth of $d \simeq 22$ μm.

The reported experimental diffraction efficiencies for the incident Transverse Electric (TE) and Transverse Magnetic (TM) polarizations are -35.2 dB (0.03%) and -27.0 dB (0.2%), respectively. These geometrical grating parameters ensure a cross-polarization scattering that is largely negligible. Thus, TE and TM power mainly couple to modes with the same polarization. HFSS results for the grating efficiencies are summarized in Table 2.3.

	$\mathbf{TE}_0$	$\mathbf{TM}_0$	$\mathbf{TE}_1$	$\mathbf{TM}_1$
$\mathbf{TE}_0$	-0.0018	-125	-33.8 (-35.2)	-139
$\mathbf{TM}_0$	-132	-0.01	-128	-26.3 (-27.0)

Table 2.3: Diffraction efficiencies in dB. Values represent HFSS simulations, with measured results from Shi et al. [43] provided in parentheses.

HFSS simulations show a power efficiency of -33.8 dB for the TE case and -26.3 dB for the TM case, computed by setting the convergence criterion for the maximum magnitude of the scattering parameters at $\Delta S \leq 10^{-6}$. The main Gaussian beam remains practically undisturbed, exhibiting minimal insertion losses of 0.0018 dB and 0.01 dB for the TE and TM polarizations, respectively. These results show strong agreement with the experimental measurements. Discrepancies between the idealized HFSS efficiencies and the experimental values can be attributed to several factors, including the HFSS model which assumes an infinite PEC and plane-wave incidence, while the experimental setup measures a Gaussian beam traveling at the end of propagation through several copper mirrors with finite diameter. Furthermore, machining imperfections in the grating mirror may account for deviations from theoretical predictions, as the small groove depth ($d = 22$

μm) makes the system particularly sensitive to fabrication tolerances. The experimental setup can be treated as a quasi-optical transmission line, since the maximum far-field diffraction angle in the transmission line is

$$\theta_{\text{W7-X}} = \arctan\left(\frac{2.14}{3.7\pi}\right) = 10.44^\circ < 20^\circ, \tag{2.24}$$

obtained by using the minimum waist of the line (3.7 mm). The lengths of the optical paths are not explicitly given in [43], but can be retrieved analytically from the knowledge of the expected beam waists at each optical transformation. The total ABCD transfer matrices for the entire optical system, evaluated independently for the tangential (T) and sagittal (S) planes, are derived:

$$\mathbb{M}^{(T)}_{\text{W7-X}} = \mathbb{M}_{f3}\mathbb{M}_{L3}\mathbb{M}^{(T)}_{mf}\mathbb{M}_{L2}\mathbb{M}_{f1}\mathbb{M}_{L1}, \tag{2.25a}$$

$$\mathbb{M}^{(S)}_{\text{W7-X}} = \mathbb{M}_{f3}\mathbb{M}_{L3}\mathbb{M}^{(S)}_{mf}\mathbb{M}_{L2}\mathbb{M}_{f1}\mathbb{M}_{L1}, \tag{2.25b}$$

where $\mathbb{M}_{L_i}$ and $\mathbb{M}_{f_i}$ represent, respectively, the free-space propagation matrix of the i-th section and the focusing matrix of the i-th mirror. Reflectors M1 and M3 are designed as astigmatism-free focusing mirrors (equal tangential and sagittal effective focal lengths, $f_1 = 148$ mm and $f_3 = 72.1$ mm), so that the astigmatism is introduced entirely by the curved grating coupler M2. Following Beutler [78], the sagittal and tangential focusing conditions of an elliptical grating reflector of physical radii R_s and R_t, at incidence angle θ_{in} and diffraction angle θ_{out}, are given by

$$\frac{1}{R_1} + \frac{1}{R_2} = \frac{\cos\theta_{\text{in}} + \cos\theta_{\text{out}}}{R_s}, \qquad \frac{\cos^2\theta_{\text{in}}}{R_1} + \frac{\cos^2\theta_{\text{out}}}{R_2} = \frac{\cos\theta_{\text{in}} + \cos\theta_{\text{out}}}{R_t}, \tag{2.26}$$

where R_1, R_2 are the object (incident) and image (diffracted) phase-center distances. The first gives the sagittal focal length, $1/f_s = 1/R_1 + 1/R_2$; the second, introducing the transverse magnification $M = \cos\theta_{\text{out}}/\cos\theta_{\text{in}}$ and dividing both sides by $\cos\theta_{\text{in}}\cos\theta_{\text{out}}$, gives the tangential one,

$$\frac{1}{f_t} = \frac{1}{M\,R_1} + \frac{M}{R_2}. \tag{2.27}$$

Hence the sagittal focal length keeps its nominal value $f_s = 469.37$ mm, while the tangential focal length is shortened to $f_t = 443.70$ mm for $\theta_{\text{in}} = 45^\circ$, $\theta_{\text{out}} = 34.6^\circ$ ($s_1 = 1347.7$ mm, $s_2 = 720.2$ mm, $M = 1.1641$). This focal-length difference, together with the beam-width magnification M, results in a waist ratio ($w_{0,x}/w_{0,y} \simeq 0.86$).

The full evolution of the spatial beam parameters traversing this system is summarized in Tables 2.4-2.5, for two possible propagation paths (a real intermediate waist after M1, and a virtual one behind M1).

Optical Stage	R_x **(mm)**	R_y **(mm)**	$w_{0,x}$ **(mm)**	$w_{0,y}$ **(mm)**	L **(mm)**	θ_{div} **(deg)**
At transmitting horn	$+\infty$	$+\infty$	4.50	4.50	0	8.61
After Mirror M1	-952.10	-952.10	18.00	18.00	170.05	2.17
After Mirror M2	-764.03	-780.91	10.99	12.70	1435.56	3.56 / 3.07
After Mirror M3	-68.84	-72.06	3.97	3.70	700.60	9.74 / 10.44

Table 2.4: Evolution of the Gaussian beam parameters along the W7-X alignment system (assuming a real intermediate waist after M1): radius of curvature, tangential and sagittal beam waists, propagation length, and far-field divergence angles.

Optical Stage	R_x **(mm)**	R_y **(mm)**	$w_{0,x}$ **(mm)**	$w_{0,y}$ **(mm)**	L **(mm)**	θ_{div} **(deg)**
At transmitting horn	$+\infty$	$+\infty$	4.50	4.50	0	8.61
After Mirror M1	+1308.15	+1308.15	18.00	18.00	125.95	2.17
After Mirror M2	-764.03	-780.91	10.99	12.70	729.86	3.56 / 3.07
After Mirror M3	-68.84	-72.06	3.97	3.70	700.60	9.74 / 10.44

Table 2.5: Evolution of the Gaussian beam parameters along the W7-X alignment system (assuming a virtual intermediate waist upstream of M1): radius of curvature, tangential and sagittal beam waists, propagation length, and far-field divergence angles.

Using the grating equation, we can confirm that for $a = 1.68$ mm and $\theta_{\text{in}} = 45°$, the diffraction angle is $\theta_{out} = 34.6° \simeq 35°$, as shown in the polar plot (Fig. 2.7).

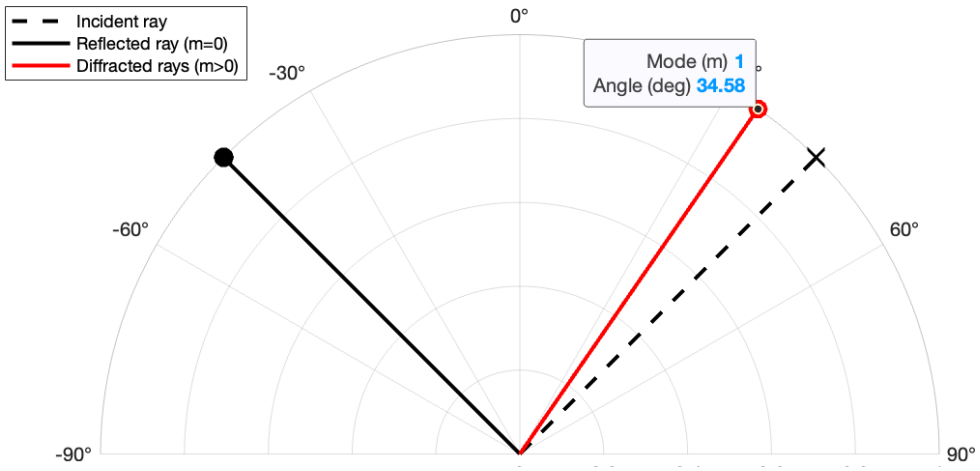


Figure 2.7: Polar plot representing the angular diffraction spectrum for the W7-X grating coupler, with the 1st order diffraction angle at $\theta \simeq 34.6°$.

From a diagnostic point of view, this alignment system provides high sensitivity to both parallel and angular displacements. Any displacement modifies the coupling coefficient at the receiving horn, generating a measurable error signal that can be used to deduce the current parallel and angular displacements in the x- and y-axes and re-align the beam. In the experimental paper, the TM polarization was chosen because of the higher dynamic range of measurements.

2.3.2. DTT Grating Polarizer

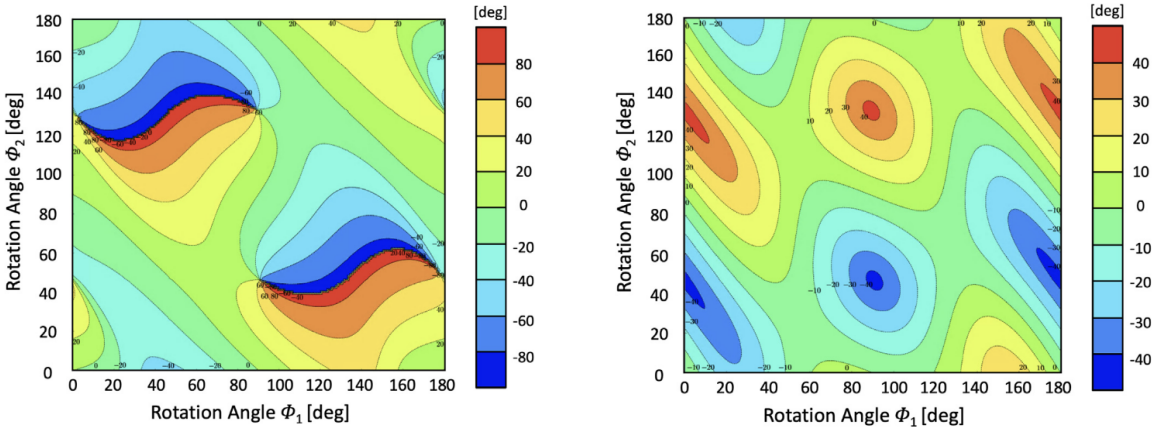
Grating reflectors are widely employed to control the polarization of EC waves. Unlike directional couplers, grating polarizers are specifically designed to scatter only the specular reflection (the 0th order) while introducing targeted phase shifts to the polarization components. In particular, for the ECRH system of DTT, the combination of two elliptical polarizers to achieve an arbitrary state of polarization has recently been studied [42]. Standard ECRH arrangements typically use planar $\lambda/4$ and $\lambda/8$ grating polarizers [61], while the DTT design currently employs two identical $\lambda/8$ polarizers with a grating period $a = 1.1$ mm, and an optimized groove depth $d = 0.46$ mm (sinusoidal profile). The choice of a sinusoidal grating profile over a lamellar one is helpful in high-power applications to prevent arcing effects. Moreover $\lambda/8$ polarizers exhibit lower ohmic losses than $\lambda/4$ polarizers [79]. When designing polarizers, a characteristic parameter to consider is the phase shift τ, which can be obtained in terms of the scattering amplitudes

$$\tau = \arg(\tilde{A}) - \arg(-\tilde{B}), \tag{2.28}$$

where $\tilde{A}$ is the scattering amplitude of the TE mode and $\tilde{B}$ is the scattering amplitude of the TM mode. From τ, it is possible to calculate the polarization angle α and the ellipticity angle β, since the amplitudes of the incident waves and the polar angle of incidence θ are known and the azimuthal angle ϕ can be changed by rotating the reflector around its normal axis. To ensure that the polarizer does not generate other scattering orders, the following condition must be respected [60]:

$$a < \frac{\lambda}{1 + \sin\theta\cos\phi}, \tag{2.29}$$

where $\theta = 22.5°$ in DTT configuration. Fig. 2.8 shows the angles α and β as a function of the two rotation angles ϕ_1 and ϕ_2, of the first and second grating polarizers, respectively, for a specific input linear polarization.



(a) Polarization angle α (b) Ellipticity angle β

Figure 2.8: Contour plots showing the achievable polarization angles α and β as a function of the mechanical rotation angles (ϕ_1 and ϕ_2) of the two identical DTT grating polarizers [42].

These two contour plots cover all possible combinations of α and β, successfully demonstrating the capability to arbitrarily control the polarization state of the beam launched into the plasma. Despite these successful results, alternative designs may be proposed in the future to simplify the real-time control algorithms for the rotation angles, as different input linear polarizations are expected for the different beam lines.

3 | Mode-Matching Method for Grating Reflectors

Modal methods are an efficient way of analyzing diffraction gratings and deriving the main properties of scattered electromagnetic waves [56]. This approach considers the electric and magnetic fields inside periodic corrugations as a superposition of propagating and evanescent modes, similarly to the modal expansion in transmission lines. Among these methods, notable examples are the Fourier Modal Method (FMM) [80, 81] (or Rigorous Coupled-Wave Analysis) and the Exact Modal Method (EMM) [82]. The former exploits the periodicity of the grating structure to expand the electromagnetic field, the medium permittivity and permeability into Fourier-Floquet series, and is primarily used for dielectric structures. The EMM expands the electromagnetic field into exact modes, which is possible only in specific cases. This method is particularly effective for solving metallic periodic structures, which can often be well approximated as perfect electric conductors. Thus, FMM and EMM can be seen as complementary methods: the former is particularly convenient for dielectrics and arbitrary shapes, while the latter is best suited for metallic lamellar gratings. Exact modal methods can also be used for arbitrary shapes through a staircase approximation, but in the case of TM-polarization, differential methods are preferred because of faster convergence [83]. These modal methods are implemented through mode-matching, the same technique used in microwave theory to solve scattering problems such as discontinuities in perfectly conducting waveguides. In those cases, the most general representation of the boundary fields involves an expansion in TE and TM modes [84]. In this chapter, the application of mode-matching follows three main steps [56]:

- Describing the physical space of the grating in two regions: a free space region where the incident wave propagates and the finite grating region in which we have the periodic corrugation.
- Imposing boundary conditions for the total electric and magnetic fields at the interfaces, and solving the equations to calculate the scattering amplitudes.

- Determining relevant quantities for the study of the scattering problem such as diffraction efficiency, amplitude and phase of the scattered waves, direction of propagation and state of polarization.

Modal methods exploit the simplicity of the geometry of lamellar gratings, which gives closed-form modes and closed-form integrals from boundary conditions. The scattering amplitudes can then be calculated by solving a linear system of equations. The contribution of this work consists in using mode-matching techniques to build a fast and practical design tool for grating reflectors of ECRH systems, independent of any commercial software. The tool is implemented in MATLAB [85], and can retrieve all the properties of the scattered electromagnetic waves given arbitrary reflector and grating geometries for 1D periodic lamellar corrugations in conical mounting. The quasi-optical framework and the local plane wave approximation allow us to obtain results that are in excellent agreement with the theoretical predictions of the grating theory, the tensor ABCD law, and alternative numerical methods for the grating efficiency, as described in Chapter 2.

3.1. Mode-Matching of 1D Lamellar Grooves

We consider a structure in the xy plane with a cell of size a and b along x- and y-axes respectively. A plane wave is incident from direction θ, ϕ, so that the electric and magnetic fields can be expressed as

$$\mathbf{E}^+ = \mathbf{E}_0^+ e^{-j\mathbf{k}^+\cdot\mathbf{r}}, \qquad \mathbf{H}^+ = \mathbf{H}_0^+ e^{-j\mathbf{k}^+\cdot\mathbf{r}} = \frac{\mathbf{k}^+ \times \mathbf{E}_0^+}{\omega\mu} e^{-j\mathbf{k}^+\cdot\mathbf{r}}, \tag{3.1}$$

with incident wavevector $\mathbf{k}^+$ defined as in Eq. 2.2. By introducing the transverse incident wavevector

$$\hat{\boldsymbol{\tau}}^+ = \frac{\boldsymbol{i}_x k_x^+ + \boldsymbol{i}_y k_y^+}{\sqrt{(k_x^+)^2 + (k_y^+)^2}}, \tag{3.2}$$

we can write the transverse-to-z fields, leaving aside the term $e^{-j\mathbf{k}^+\cdot\mathbf{r}}$ as

$$\mathbf{E}_{0t}^+ = \mathbf{E}_0^{+\mathrm{TE}} + \mathbf{E}_0^{+\mathrm{TM}} = \frac{\boldsymbol{i}_z \times \hat{\boldsymbol{\tau}}^+}{\sqrt{ab}} E_0^{+\mathrm{TE}} + \frac{\hat{\boldsymbol{\tau}}^+}{\sqrt{ab}} E_0^{+\mathrm{TM}} = \frac{\hat{\mathbf{e}}_{\mathrm{TE}}^+}{\sqrt{ab}} E_0^{+\mathrm{TE}} + \frac{\hat{\mathbf{e}}_{\mathrm{TM}}^+}{\sqrt{ab}} E_0^{+\mathrm{TM}}, \tag{3.3a}$$

$$\begin{aligned}\mathbf{H}_{0t}^+ &= \mathbf{H}_0^{+\mathrm{TE}} + \mathbf{H}_0^{+\mathrm{TM}} = \frac{-\boldsymbol{i}_z \times (\boldsymbol{i}_z \times \hat{\boldsymbol{\tau}}^+)}{\sqrt{ab}} \frac{E_0^{+\mathrm{TE}} \cos\theta}{\eta} - \frac{\boldsymbol{i}_z \times \hat{\boldsymbol{\tau}}^+}{\sqrt{ab}} \frac{E_0^{+\mathrm{TM}}}{\eta \cos\theta} \\ &= \frac{\hat{\boldsymbol{\tau}}^+}{\sqrt{ab}} \frac{E_0^{+\mathrm{TE}} \cos\theta}{\eta} - \frac{\boldsymbol{i}_z \times \hat{\boldsymbol{\tau}}^+}{\sqrt{ab}} \frac{E_0^{+\mathrm{TM}}}{\eta \cos\theta} = \frac{\hat{\boldsymbol{\tau}}^+}{\sqrt{ab}} \frac{E_0^{+\mathrm{TE}}}{\eta_{\mathrm{TE}}} - \frac{\boldsymbol{i}_z \times \hat{\boldsymbol{\tau}}^+}{\sqrt{ab}} \frac{E_0^{+\mathrm{TM}}}{\eta_{\mathrm{TM}}} \\ &= \frac{\hat{\mathbf{h}}_{\mathrm{TE}}^+}{\sqrt{ab}} \frac{E_0^{+\mathrm{TE}}}{\eta_{\mathrm{TE}}} + \frac{\hat{\mathbf{h}}_{\mathrm{TM}}^+}{\sqrt{ab}} \frac{E_0^{+\mathrm{TM}}}{\eta_{\mathrm{TM}}},\end{aligned} \tag{3.3b}$$

where the free-space impedances have been introduced and defined as

$$\eta_{\mathrm{TE}} = \frac{\eta}{\cos\theta}, \qquad \eta_{\mathrm{TM}} = \eta \cos\theta. \tag{3.4}$$

When $\theta = 0$, TE and TM polarization are set with the convention

$$\hat{\mathbf{e}}_{\mathrm{TE}}^+ = -\boldsymbol{i}_\phi, \qquad \hat{\mathbf{e}}_{\mathrm{TM}}^+ = \hat{\mathbf{e}}_{\mathrm{TE}}^+ \times \boldsymbol{i}_z, \tag{3.5}$$

with z oriented out of the periodic structure, as shown in Fig. 3.1.

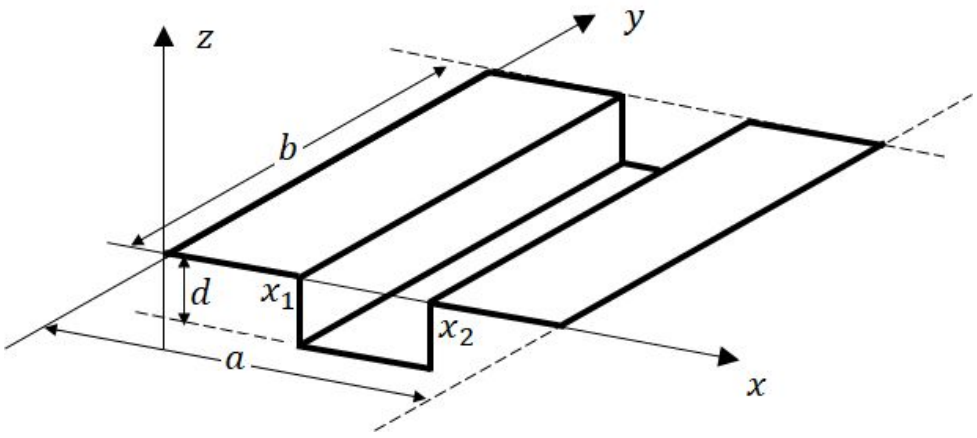


Figure 3.1: Lamellar one-dimensional unit cell with grating period a along x, cell size b along y, groove width $w = x_2 - x_1$, groove depth d.

If the lattice is rectangular, we can write the set of scattered waves as a Rayleigh expan-

sion:

$$\mathbf{E}^- = \sum_{m=-\infty}^{\infty}\sum_{n=-\infty}^{\infty} \mathbf{E}^-_{mn} e^{-j\mathbf{k}_{mn}\cdot\mathbf{r}}, \qquad \mathbf{H}^- = \sum_{m=-\infty}^{\infty}\sum_{n=-\infty}^{\infty} \frac{\mathbf{k}_{mn}\times\mathbf{E}^-_{mn}}{\omega\mu} e^{-j\mathbf{k}_{mn}\cdot\mathbf{r}}, \tag{3.6}$$

with wavenumbers given by Eqs. 2.3-2.4. Now we can define a transverse vector for the reflected waves:

$$\boldsymbol{\tau}_{mn} = \boldsymbol{i}_x k_{xm} + \boldsymbol{i}_y k_{yn}, \qquad \hat{\boldsymbol{\tau}}_{mn} = \frac{\boldsymbol{\tau}_{mn}}{|\boldsymbol{\tau}_{mn}|} = \frac{\boldsymbol{i}_x k_{xm} + \boldsymbol{i}_y k_{yn}}{\sqrt{k_{xm}^2 + k_{yn}^2}}, \tag{3.7}$$

so that we can rewrite Eq. 2.3c in its transverse and longitudinal components

$$\mathbf{k}_{mn} = \boldsymbol{\tau}_{mn} + \boldsymbol{i}_z k_{z,mn} \tag{3.8}$$

and express the Floquet expansion for the transverse-to-z fields at $z = 0$ as

$$\begin{aligned}
\mathbf{E}^-_{mn} &= \mathbf{E}^{\mathrm{TE}}_{mn} + \mathbf{E}^{\mathrm{TM}}_{mn} \\
&= \tilde{A}_{mn}\frac{\hat{\boldsymbol{\tau}}_{mn}\times\boldsymbol{i}_z}{\sqrt{ab}} e^{-j\boldsymbol{\tau}_{mn}\cdot\mathbf{r}} + \tilde{B}_{mn}\frac{\hat{\boldsymbol{\tau}}_{mn}}{\sqrt{ab}} e^{-j\boldsymbol{\tau}_{mn}\cdot\mathbf{r}}, \\
&= \tilde{A}_{mn}\frac{\tilde{\mathbf{e}}^{\mathrm{TE}}_{mn}}{\sqrt{ab}} e^{-j\boldsymbol{\tau}_{mn}\cdot\mathbf{r}} + \tilde{B}_{mn}\frac{\tilde{\mathbf{e}}^{\mathrm{TM}}_{mn}}{\sqrt{ab}} e^{-j\boldsymbol{\tau}_{mn}\cdot\mathbf{r}},
\end{aligned} \tag{3.9a}$$

$$\begin{aligned}
\mathbf{H}^-_{mn} &= \mathbf{H}^{\mathrm{TE}}_{mn} + \mathbf{H}^{\mathrm{TM}}_{mn} = \\
&= \tilde{A}_{mn} Y^{\mathrm{TE}}_{mn}\frac{\hat{\boldsymbol{\tau}}_{mn}}{\sqrt{ab}} e^{-j\boldsymbol{\tau}_{mn}\cdot\mathbf{r}} + \tilde{B}_{mn} Y^{\mathrm{TM}}_{mn}\frac{\boldsymbol{i}_z\times\hat{\boldsymbol{\tau}}_{mn}}{\sqrt{ab}} e^{-j\boldsymbol{\tau}_{mn}\cdot\mathbf{r}} \\
&= \tilde{A}_{mn} Y^{\mathrm{TE}}_{mn}\frac{\tilde{\mathbf{h}}^{\mathrm{TE}}_{mn}}{\sqrt{ab}} e^{-j\boldsymbol{\tau}_{mn}\cdot\mathbf{r}} + \tilde{B}_{mn} Y^{\mathrm{TM}}_{mn}\frac{\tilde{\mathbf{h}}^{\mathrm{TM}}_{mn}}{\sqrt{ab}} e^{-j\boldsymbol{\tau}_{mn}\cdot\mathbf{r}}.
\end{aligned} \tag{3.9b}$$

where the admittances of the TE and TM modes have been defined

$$Y^{\mathrm{TM}}_{mn} = \frac{\omega\epsilon}{k_{z,mn}}, \qquad Y^{\mathrm{TE}}_{mn} = \frac{k_{z,mn}}{\omega\mu}. \tag{3.10}$$

We notice that the case $\theta = 0$ must be treated separately by arbitrarily setting the TE and TM component directions along the x- or y-axes. The directions can be set according to the azimuthal angle ϕ of the incident wave, taking the limit $\theta \to 0$. The expansion

used has the following orthogonality properties:

$$\frac{1}{ab}\int_{\text{cell}} \left(\tilde{\mathbf{e}}^{\text{TE}}_{mn}\, e^{-j\boldsymbol{\tau}_{mn}\cdot\mathbf{r}}\right)\cdot\left(\tilde{\mathbf{e}}^{\text{TE}}_{m'n'}\, e^{-j\boldsymbol{\tau}_{m'n'}\cdot\mathbf{r}}\right)^{*} dS = \delta_{mm'}\delta_{nn'}, \tag{3.11a}$$

$$\frac{1}{ab}\int_{\text{cell}} \left(\tilde{\mathbf{e}}^{\text{TM}}_{mn}\, e^{-j\boldsymbol{\tau}_{mn}\cdot\mathbf{r}}\right)\cdot\left(\tilde{\mathbf{e}}^{\text{TM}}_{m'n'}\, e^{-j\boldsymbol{\tau}_{m'n'}\cdot\mathbf{r}}\right)^{*} dS = \delta_{mm'}\delta_{nn'}, \tag{3.11b}$$

$$\frac{1}{ab}\int_{\text{cell}} \left(\tilde{\mathbf{e}}^{\text{TE}}_{mn}\, e^{-j\boldsymbol{\tau}_{mn}\cdot\mathbf{r}}\right)\cdot\left(\tilde{\mathbf{e}}^{\text{TM}}_{m'n'}\, e^{-j\boldsymbol{\tau}_{m'n'}\cdot\mathbf{r}}\right)^{*} dS = 0, \tag{3.11c}$$

with the following conventions for the reflected fields:

$$\tilde{\mathbf{e}}^{\text{TE}}_{mn} = \hat{\boldsymbol{\tau}}_{mn}\times\boldsymbol{i}_z, \qquad \tilde{\mathbf{e}}^{\text{TM}}_{mn} = \hat{\boldsymbol{\tau}}_{mn}, \tag{3.12a}$$

$$\tilde{\mathbf{h}}^{\text{TE}}_{mn} = \hat{\boldsymbol{\tau}}_{mn}, \qquad \tilde{\mathbf{h}}^{\text{TM}}_{mn} = \boldsymbol{i}_z\times\hat{\boldsymbol{\tau}}_{mn}. \tag{3.12b}$$

3.1.1. Fields in the Slot

Fields in homogeneous regions can be derived from two z-directed Hertz-Debye potentials $\boldsymbol{i}_z\Phi$ and $\boldsymbol{i}_z\Psi$, solutions of

$$\nabla^2\Phi + k^2\Phi = 0, \qquad \nabla^2\Psi + k^2\Psi = 0. \tag{3.13}$$

Assuming solutions of the form

$$\Phi(x,y,z) = \varphi(x,y)e^{\mp jk_z z}, \qquad \Psi(x,y,z) = \psi(x,y)e^{\mp jk_z z}, \tag{3.14}$$

we have that the transverse fields are

$$\mathbf{E}(x,y) = \boldsymbol{i}_z\times\nabla_t\varphi - \frac{\partial_z}{j\omega\epsilon}\nabla_t\psi, \tag{3.15a}$$

$$\mathbf{H}(x,y) = \boldsymbol{i}_z\times\nabla_t\psi + \frac{\partial_z}{j\omega\mu}\nabla_t\varphi. \tag{3.15b}$$

We can now define a field expansion also for the slot, and find the scattering coefficients by mode-matching. Let the slot be oriented along y and place the origin of the coordinates at the beginning of the cell. The slot has a width $w = x_2 - x_1$ and a depth d and its origin is at x_1, as in Fig. 3.1. Using the previous potential functions to represent the fields in

the slot, we can write for TE modes, being $\partial\varphi_{pn}/\partial n = 0$ on PEC lateral walls:

$$\Phi_{pn} = e^{-jk_{yn}y} \cos\frac{p\pi(x-x_1)}{w} \sin[k_{z,pn}(d+z)], \qquad p = 0, 1 \dots P \tag{3.16}$$

so that at $z = -d$ the electric field goes to 0, as shown in the following, then

$$k_{z,pn} = \sqrt{k^2 - k_{yn}^2 - \left(\frac{p\pi}{w}\right)^2} = \sqrt{k^2 - k_{yn}^2 - \kappa_{xp}^2} \tag{3.17}$$

with $k_{z,pn}$ real negative or imaginary positive. The slot modes are found as

$$\mathbf{e}_{pn}^{\mathrm{TE}} = \boldsymbol{i}_z \times \nabla_t \varphi_{pn}, \qquad \mathbf{h}_{pn}^{\mathrm{TE}} = -\frac{\partial_z}{j\omega\mu} \boldsymbol{i}_z \times \mathbf{e}_{pn}^{\mathrm{TE}}. \tag{3.18}$$

Setting $\xi = \pi(x - x_1)/w$ and $z = 0$ (input of the slot), we have for TE modes

$$\begin{aligned} \mathbf{e}_{pn}^{\mathrm{TE}} &= -\boldsymbol{i}_x \frac{\partial\varphi_{pn}}{\partial y} + \boldsymbol{i}_y \frac{\partial\varphi_{pn}}{\partial x} \\ &= -\boldsymbol{i}_x(-jk_{yn}) e_y^- c_{xp} s_{zp} - \boldsymbol{i}_y \kappa_{xp} e_y^- s_{xp} s_{zp} \\ &= \left[\boldsymbol{i}_x jk_{yn} \cos p\xi - \boldsymbol{i}_y \kappa_{xp} \sin p\xi\right] e^{-jk_{yn}y} \sin(k_{z,pn}d) \\ &= \left[\boldsymbol{i}_x jk_{yn} c_{xp} - \boldsymbol{i}_y \kappa_{xp} s_{xp}\right] e_y^- s_{zp} \end{aligned} \tag{3.19a}$$

$$\begin{aligned} \mathbf{h}_{pn}^{\mathrm{TE}} &= -\left[\boldsymbol{i}_y jk_{yn} \cos p\xi + \boldsymbol{i}_x \kappa_{xp} \sin p\xi\right] \frac{k_{z,pn}}{j\omega\mu} e^{-jk_{yn}y} \cos(k_{z,pn}d) \\ &= -\left[\boldsymbol{i}_y jk_{yn} c_{xp} + \boldsymbol{i}_x \kappa_{xp} s_{xp}\right] \frac{k_{z,pn}}{j\omega\mu} e_y^- c_{zp}. \end{aligned} \tag{3.19b}$$

For TM modes, being $\psi_{pn} = 0$ on PEC, we have the following potential

$$\Psi_{pn} = e^{-jk_{yn}y} \sin\frac{p\pi(x-x_1)}{w} \cos[k_{z,pn}(d+z)], \qquad p = 1, 2 \dots P \tag{3.20}$$

which gives:

$$\mathbf{h}_{pn}^{\mathrm{TM}} = \boldsymbol{i}_z \times \nabla_t \psi_{pn}, \qquad \mathbf{e}_{pn}^{\mathrm{TM}} = \frac{\partial_z}{j\omega\epsilon} \boldsymbol{i}_z \times \mathbf{h}_{pn}^{\mathrm{TM}} \tag{3.21}$$

$$\begin{aligned}\mathbf{h}_{pn}^{\mathrm{TM}} &= -\boldsymbol{i}_x \frac{\partial \psi_{pn}}{\partial y} + \boldsymbol{i}_y \frac{\partial \psi_{pn}}{\partial x} \\ &= -\boldsymbol{i}_x (-jk_{yn}) e_y^- s_{xp} c_{zp} + \boldsymbol{i}_y \kappa_{xp} e_y^- c_{xp} c_{zp} \\ &= \left[\boldsymbol{i}_x jk_{yn} \sin p\xi + \boldsymbol{i}_y \kappa_{xp} \cos p\xi\right] e^{-jk_{yn}y} \cos(k_{z,pn} d) \\ &= \left[\boldsymbol{i}_x jk_{yn} s_{xp} + \boldsymbol{i}_y \kappa_{xp} c_{xp}\right] e_y^- c_{zp}, \end{aligned} \tag{3.22a}$$

$$\begin{aligned}\mathbf{e}_{pn}^{\mathrm{TM}} &= \left[-\boldsymbol{i}_y jk_{yn} \sin p\xi + \boldsymbol{i}_x \kappa_{xp} \cos p\xi\right] \frac{k_{z,pn}}{j\omega\epsilon} e^{-jk_{yn}y} \sin(k_{z,pn} d) \\ &= \left[-\boldsymbol{i}_y jk_{yn} s_{xp} + \boldsymbol{i}_x \kappa_{xp} c_{xp}\right] \frac{k_{z,pn}}{j\omega\epsilon} e_y^- s_{zp}. \end{aligned} \tag{3.22b}$$

A TEM mode can also be present, but only if $k_{yn} = 0$. In fact the TEM potential $\Psi_0(x, y, z) = \psi_0(x, y) \cos[k(z + d)]$ must obey the equation

$$\nabla_t^2 \psi_0 = 0, \tag{3.23}$$

and a solution is possible only if $k_{yn} = 0$. In that case a TEM solution is given by the linear potential

$$\psi_0 = x - x_1. \tag{3.24}$$

Note that for this case the constant-field TE solution corresponding to $p = 0$ vanishes because $k_{yn} = 0$. This case can be considered as a special case of TM mode since the potential function can be seen of TM type with non-zero value of the potential on one of the two conductors. So we can write

$$\mathbf{e}_{00}^{\mathrm{TM}} = \boldsymbol{i}_x \frac{k}{j\omega\epsilon} s_{z0}, \qquad \mathbf{h}_{00}^{\mathrm{TM}} = \boldsymbol{i}_y \frac{\partial \psi_0}{\partial x} = \boldsymbol{i}_y c_{z0}. \tag{3.25}$$

Also the case $k_{xm} = k_{yn} = 0$ should be treated as a special case, since in that case we have normal incidence and we must define differently the incident wave.

3.1.2. Groove Mode-Matching

We can write, letting $z = 0$, the matching of the tangential components of the total electric and magnetic field at the boundary of the cell:

$$\mathbf{E}_t^+ + \mathbf{E}_t^- = \sum_{p,n} \left(A_{pn}\mathbf{e}_{pn}^{\mathrm{TE}} + B_{pn}\mathbf{e}_{pn}^{\mathrm{TM}} \right), \tag{3.26a}$$

$$\mathbf{H}_t^+ + \mathbf{H}_t^- = \sum_{p,n} \left(A_{pn}\mathbf{h}_{pn}^{\mathrm{TE}} + B_{pn}\mathbf{h}_{pn}^{\mathrm{TM}} \right), \tag{3.26b}$$

and writing the reflected fields into Fourier-Floquet expansion

$$\begin{aligned} \mathbf{E}_t^+ + \frac{1}{\sqrt{ab}} \sum_{m,n} \left(\tilde{A}_{mn}\tilde{\mathbf{e}}_{mn}^{\mathrm{TE}} + \tilde{B}_{mn}\tilde{\mathbf{e}}_{mn}^{\mathrm{TM}} \right) e^{-j\boldsymbol{\tau}_{mn}\cdot\mathbf{r}} \\ = \sum_{p,n} \left(A_{pn}\mathbf{e}_{pn}^{\mathrm{TE}} + B_{pn}\mathbf{e}_{pn}^{\mathrm{TM}} \right), \end{aligned} \tag{3.27a}$$

$$\begin{aligned} \mathbf{H}_t^+ + \frac{1}{\sqrt{ab}} \sum_{m,n} \left(\tilde{A}_{mn}Y_{mn}^{\mathrm{TE}}\tilde{\mathbf{h}}_{mn}^{\mathrm{TE}} + \tilde{B}_{mn}Y_{mn}^{\mathrm{TM}}\tilde{\mathbf{h}}_{mn}^{\mathrm{TM}} \right) e^{-j\boldsymbol{\tau}_{mn}\cdot\mathbf{r}} \\ = \sum_{p,n} \left(A_{pn}\mathbf{h}_{pn}^{\mathrm{TE}} + B_{pn}\mathbf{h}_{pn}^{\mathrm{TM}} \right). \end{aligned} \tag{3.27b}$$

For the projections, we use the Floquet modes in free space for the electric field and the Floquet modes in the slot for magnetic field. Thus, letting S_{ab} be the surface of the cell and S_{wb} the surface of the slot, we obtain linear system of four equations:

$$\begin{aligned} &\int_{S_{ab}} \frac{\tilde{\mathbf{e}}_{m'n'}^{\mathrm{TE}*}}{\sqrt{ab}} e^{j\boldsymbol{\tau}_{m'n'}\cdot\mathbf{r}} \cdot \left[\mathbf{E}_t^+ + \frac{1}{\sqrt{ab}} \sum_{m,n} \left(\tilde{A}_{mn}\tilde{\mathbf{e}}_{mn}^{\mathrm{TE}} + \tilde{B}_{mn}\tilde{\mathbf{e}}_{mn}^{\mathrm{TM}} \right) e^{-j\boldsymbol{\tau}_{mn}\cdot\mathbf{r}} \right] dS \\ &= \int_{S_{ab}} \frac{\tilde{\mathbf{e}}_{m'n'}^{\mathrm{TE}*}}{\sqrt{ab}} e^{j\boldsymbol{\tau}_{m'n'}\cdot\mathbf{r}} \cdot \sum_{p,n} \left(A_{pn}\mathbf{e}_{pn}^{\mathrm{TE}} + B_{pn}\mathbf{e}_{pn}^{\mathrm{TM}} \right) dS, \end{aligned} \tag{3.28a}$$

$$\begin{aligned} &\int_{S_{ab}} \frac{\tilde{\mathbf{e}}_{m'n'}^{\mathrm{TM}*}}{\sqrt{ab}} e^{j\boldsymbol{\tau}_{m'n'}\cdot\mathbf{r}} \cdot \left[\mathbf{E}_t^+ + \frac{1}{\sqrt{ab}} \sum_{m,n} \left(\tilde{A}_{mn}\tilde{\mathbf{e}}_{mn}^{\mathrm{TE}} + \tilde{B}_{mn}\tilde{\mathbf{e}}_{mn}^{\mathrm{TM}} \right) e^{-j\boldsymbol{\tau}_{mn}\cdot\mathbf{r}} \right] dS \\ &= \int_{S_{ab}} \frac{\tilde{\mathbf{e}}_{m'n'}^{\mathrm{TM}*}}{\sqrt{ab}} e^{j\boldsymbol{\tau}_{m'n'}\cdot\mathbf{r}} \cdot \sum_{p,n} \left(A_{pn}\mathbf{e}_{pn}^{\mathrm{TE}} + B_{pn}\mathbf{e}_{pn}^{\mathrm{TM}} \right) dS, \end{aligned} \tag{3.28b}$$

$$\int_{S_{wb}} \mathbf{h}_{p'n'}^{\mathrm{TE}*} \cdot \left[\mathbf{H}_t^+ + \frac{1}{\sqrt{ab}} \sum_{m,n} \left(\tilde{A}_{mn} Y_{mn}^{\mathrm{TE}} \tilde{\mathbf{h}}_{mn}^{\mathrm{TE}} + \tilde{B}_{mn} Y_{mn}^{\mathrm{TM}} \tilde{\mathbf{h}}_{mn}^{\mathrm{TM}} \right) e^{-j\boldsymbol{\tau}_{mn}\cdot\mathbf{r}} \right] dS$$

$$= \int_{S_{wb}} \mathbf{h}_{p'n'}^{\mathrm{TE}*} \cdot \sum_{p,n} \left(A_{pn} \mathbf{h}_{pn}^{\mathrm{TE}} + B_{pn} \mathbf{h}_{pn}^{\mathrm{TM}} \right) dS, \tag{3.29a}$$

$$\int_{S_{wb}} \mathbf{h}_{p'n'}^{\mathrm{TM}*} \cdot \left[\mathbf{H}_t^+ + \frac{1}{\sqrt{ab}} \sum_{m,n} \left(\tilde{A}_{mn} Y_{mn}^{\mathrm{TE}} \tilde{\mathbf{h}}_{mn}^{\mathrm{TE}} + \tilde{B}_{mn} Y_{mn}^{\mathrm{TM}} \tilde{\mathbf{h}}_{mn}^{\mathrm{TM}} \right) e^{-j\boldsymbol{\tau}_{mn}\cdot\mathbf{r}} \right] dS$$

$$= \int_{S_{wb}} \mathbf{h}_{p'n'}^{\mathrm{TM}*} \cdot \sum_{p,n} \left(A_{pn} \mathbf{h}_{pn}^{\mathrm{TE}} + B_{pn} \mathbf{h}_{pn}^{\mathrm{TM}} \right) dS, \tag{3.29b}$$

and because of the geometry of the corrugation, we can set $n = 0$, and choose the size b as small as desired. Therefore, in all equations, $k_{yn} = k_{y0} = k_y^+$.

In matrix form we can write the boundary conditions in a more immediate way:

$$\mathbb{E}^{+,\mathrm{TE}} + \mathbb{E}_{11}^{\mathrm{TE,TE}} \tilde{\mathbb{A}} + \mathbb{E}_{11}^{\mathrm{TE,TM}} \tilde{\mathbb{B}} = \mathbb{E}_{12}^{\mathrm{TE,TE}} \mathbb{A} + \mathbb{E}_{12}^{\mathrm{TE,TM}} \mathbb{B}, \tag{3.30}$$

$$\mathbb{E}^{+,\mathrm{TM}} + \mathbb{E}_{11}^{\mathrm{TM,TE}} \tilde{\mathbb{A}} + \mathbb{E}_{11}^{\mathrm{TM,TM}} \tilde{\mathbb{B}} = \mathbb{E}_{12}^{\mathrm{TM,TE}} \mathbb{A} + \mathbb{E}_{12}^{\mathrm{TM,TM}} \mathbb{B}, \tag{3.31}$$

$$\mathbb{H}^{+,\mathrm{TE}} + \mathbb{H}_{21}^{\mathrm{TE,TE}} \tilde{\mathbb{A}} + \mathbb{H}_{21}^{\mathrm{TE,TM}} \tilde{\mathbb{B}} = \mathbb{H}_{22}^{\mathrm{TE,TE}} \mathbb{A} + \mathbb{H}_{22}^{\mathrm{TE,TM}} \mathbb{B}, \tag{3.32}$$

$$\mathbb{H}^{+,\mathrm{TM}} + \mathbb{H}_{21}^{\mathrm{TM,TE}} \tilde{\mathbb{A}} + \mathbb{H}_{21}^{\mathrm{TM,TM}} \tilde{\mathbb{B}} = \mathbb{H}_{22}^{\mathrm{TM,TE}} \mathbb{A} + \mathbb{H}_{22}^{\mathrm{TM,TM}} \mathbb{B}. \tag{3.33}$$

The solution of each integral projection can be found in Appendix A. We want to find $\tilde{\mathbb{A}}$ and $\tilde{\mathbb{B}}$. By reorganizing the integrals into submatrices, we find

$$\mathbb{E}^+ + \mathbb{E}_{11} \tilde{\mathbb{C}} = \mathbb{E}_{12} \mathbb{C}, \tag{3.34}$$

$$\mathbb{H}^+ + \mathbb{H}_{21} \tilde{\mathbb{C}} = \mathbb{H}_{22} \mathbb{C},$$

where we have grouped the integrals into four submatrices

$$\mathbb{E}_{11} = \begin{bmatrix} \mathbb{E}_{11}^{\mathrm{TE,TE}} & \mathbb{E}_{11}^{\mathrm{TE,TM}} \\ \mathbb{E}_{11}^{\mathrm{TM,TE}} & \mathbb{E}_{11}^{\mathrm{TM,TM}} \end{bmatrix}, \qquad \mathbb{E}_{12} = \begin{bmatrix} \mathbb{E}_{12}^{\mathrm{TE,TE}} & \mathbb{E}_{12}^{\mathrm{TE,TM}} \\ \mathbb{E}_{12}^{\mathrm{TM,TE}} & \mathbb{E}_{12}^{\mathrm{TM,TM}} \end{bmatrix}, \tag{3.35a}$$

$$\mathbb{H}_{21} = \begin{bmatrix} \mathbb{H}_{21}^{\mathrm{TE,TE}} & \mathbb{H}_{21}^{\mathrm{TE,TM}} \\ \mathbb{H}_{21}^{\mathrm{TM,TE}} & \mathbb{H}_{21}^{\mathrm{TM,TM}} \end{bmatrix}, \qquad \mathbb{H}_{22} = \begin{bmatrix} \mathbb{H}_{22}^{\mathrm{TE,TE}} & \mathbb{H}_{22}^{\mathrm{TE,TM}} \\ \mathbb{H}_{22}^{\mathrm{TM,TE}} & \mathbb{H}_{22}^{\mathrm{TM,TM}} \end{bmatrix}. \tag{3.35b}$$

The scattering amplitudes vectors are:

$$\tilde{\mathbb{C}} = \begin{bmatrix} \tilde{\mathbb{A}} \\ \tilde{\mathbb{B}} \end{bmatrix}, \qquad \mathbb{C} = \begin{bmatrix} \mathbb{A} \\ \mathbb{B} \end{bmatrix}. \tag{3.36}$$

We find

$$\mathbb{C} = \mathbb{H}_{22}^{-1}\mathbb{H}^{+} + \mathbb{H}_{22}^{-1}\mathbb{H}_{21}\tilde{\mathbb{C}} \tag{3.37}$$

and

$$\mathbb{E}^{+} + \mathbb{E}_{11}\tilde{\mathbb{C}} = \mathbb{E}_{12}\mathbb{H}_{22}^{-1}\mathbb{H}^{+} + \mathbb{E}_{12}\mathbb{H}_{22}^{-1}\mathbb{H}_{21}\tilde{\mathbb{C}} \tag{3.38}$$

so that

$$\mathbb{E}^{+} - \mathbb{E}_{12}\mathbb{H}_{22}^{-1}\mathbb{H}^{+} = (\mathbb{E}_{12}\mathbb{H}_{22}^{-1}\mathbb{H}_{21} - \mathbb{E}_{11})\tilde{\mathbb{C}}, \tag{3.39}$$

obtaining a final matrix expression for the scattering amplitudes vector:

$$\tilde{\mathbb{C}} = (\mathbb{E}_{12}\mathbb{H}_{22}^{-1}\mathbb{H}_{21} - \mathbb{E}_{11})^{-1}(\mathbb{E}^{+} - \mathbb{E}_{12}\mathbb{H}_{22}^{-1}\mathbb{H}^{+}) \tag{3.40}$$

We can use the scattering amplitudes $\tilde{\mathbb{A}}, \tilde{\mathbb{B}}$ to retrieve the scattering parameters. Assuming the incident plane wave corresponds to the fundamental Floquet mode ($m = 0, n = 0$), which is propagating so that Y_{00} is real, the power flowing in the z-direction (the propagation direction normal to the grating) is given by:

$$P_{00}^{+,\mathrm{TE}} = \frac{1}{2}\mathfrak{Re}(Y_{00}^{\mathrm{TE}}) \left| \int_{S_{ab}} \frac{\tilde{\mathbf{e}}_{00}^{\mathrm{TE}*}}{\sqrt{ab}} e^{j\boldsymbol{\tau}_{00}\cdot\mathbf{r}} \cdot \mathbf{E}^{+}\, dS \right|^2 = \frac{1}{2}\mathfrak{Re}(Y_{00}^{TE})|E_0^{+,TE}|^2, \tag{3.41a}$$

$$P_{00}^{+,\mathrm{TM}} = \frac{1}{2}\mathfrak{Re}(Y_{00}^{\mathrm{TM}}) \left| \int_{S_{ab}} \frac{\tilde{\mathbf{e}}_{00}^{\mathrm{TM}*}}{\sqrt{ab}} e^{j\boldsymbol{\tau}_{00}\cdot\mathbf{r}} \cdot \mathbf{E}^{+}\, dS \right|^2 = \frac{1}{2}\mathfrak{Re}(Y_{00}^{TM})|E_0^{+,TM}|^2. \tag{3.41b}$$

For the scattered wave, the power carried in the z-direction by the m-th order is extracted by projecting the total scattered field $\mathbf{E}^{-}$ onto the Floquet basis:

$$P_{m0}^{-,\mathrm{TE}} = \frac{1}{2}\mathfrak{Re}(Y_{m0}^{\mathrm{TE}}) \left| \int_{S_{ab}} \frac{\tilde{\mathbf{e}}_{m0}^{\mathrm{TE}*}}{\sqrt{ab}} e^{j\boldsymbol{\tau}_{m0}\cdot\mathbf{r}} \cdot \mathbf{E}^{-}\, dS \right|^2 = \frac{1}{2}\mathfrak{Re}(Y_{m0}^{TE})|\tilde{A}_{m0}|^2, \tag{3.42a}$$

$$P_{m0}^{-,\mathrm{TM}} = \frac{1}{2}\mathfrak{Re}(Y_{m0}^{\mathrm{TM}}) \left| \int_{S_{ab}} \frac{\tilde{\mathbf{e}}_{m0}^{\mathrm{TM}*}}{\sqrt{ab}} e^{j\boldsymbol{\tau}_{m0}\cdot\mathbf{r}} \cdot \mathbf{E}^{-}\, dS \right|^2 = \frac{1}{2}\mathfrak{Re}(Y_{m0}^{TM})|\tilde{B}_{m0}|^2. \tag{3.42b}$$

It is important to note that evanescent orders (where $k_{z,m0}$ is purely imaginary) carry no power in the propagation direction, since the real part of their wave admittance vanishes ($\mathfrak{Re}(Y_{m0}) = 0$). The scattering coefficients are defined as the square root of the ratio of

the z-directed powers ($|S| = W^-/W^+$ with $W = \sqrt{P}$), yielding:

$$|S_{m0}^{\mathrm{TE,TE}}| = \frac{W_{m0}^{-,\mathrm{TE}}}{W_{00}^{+,\mathrm{TE}}} = \frac{|\tilde{A}_{m0}|}{|E_0^{+,\mathrm{TE}}|}\sqrt{\frac{\mathfrak{Re}(Y_{m0}^{TE})}{\mathfrak{Re}(Y_{00}^{\mathrm{TE}})}},$$

$$|S_{m0}^{\mathrm{TE,TM}}| = \frac{W_{m0}^{-,\mathrm{TE}}}{W_{00}^{+,\mathrm{TM}}} = \frac{|\tilde{A}_{m0}|}{|E_0^{+,\mathrm{TM}}|}\sqrt{\frac{\mathfrak{Re}(Y_{m0}^{\mathrm{TE}})}{\mathfrak{Re}(Y_{00}^{\mathrm{TM}})}},$$

$$|S_{m0}^{\mathrm{TM,TE}}| = \frac{W_{m0}^{-,\mathrm{TM}}}{W_{00}^{+,\mathrm{TE}}} = \frac{|\tilde{B}_{m0}|}{|E_0^{+,\mathrm{TE}}|}\sqrt{\frac{\mathfrak{Re}(Y_{m0}^{\mathrm{TM}})}{\mathfrak{Re}(Y_{00}^{\mathrm{TE}})}},$$

$$|S_{m0}^{\mathrm{TM,TM}}| = \frac{W_{m0}^{-,\mathrm{TM}}}{W_{00}^{+,\mathrm{TM}}} = \frac{|\tilde{B}_{m0}|}{|E_0^{+,\mathrm{TM}}|}\sqrt{\frac{\mathfrak{Re}(Y_{m0}^{\mathrm{TM}})}{\mathfrak{Re}(Y_{00}^{\mathrm{TM}})}}.$$

The squared magnitude of each scattering coefficient gives the diffraction efficiency into a particular diffraction order for a specific input/output polarization, thus the fraction of incident power diffracted into that order [56].

3.2. Gaussian Beam Diffraction

From the knowledge of the scattering amplitudes $\tilde{\mathbb{A}}$ and $\tilde{\mathbb{B}}$, we can compute the scattered field over the surface of a single unit cell. For a specific Floquet mode (m, n), the transverse-to-z scattered electric field evaluated at the surface ($z = 0$) is given by:

$$\begin{aligned}\mathbf{E}_{mn}^{-} &= \mathbf{E}_{mn}^{\mathrm{TM}} + \mathbf{E}_{mn}^{\mathrm{TE}} = \tilde{B}_{mn}\tilde{\mathbf{e}}_{mn}^{\mathrm{TM}} + \tilde{A}_{mn}\tilde{\mathbf{e}}_{mn}^{\mathrm{TE}} \\ &= \tilde{B}_{mn}\frac{\hat{\boldsymbol{\tau}}_{mn}}{\sqrt{ab}}e^{-j\boldsymbol{\tau}_{mn}\cdot\mathbf{r}_{uv}} + \tilde{A}_{mn}\frac{\hat{\boldsymbol{\tau}}_{mn}\times\boldsymbol{i}_z}{\sqrt{ab}}e^{-j\boldsymbol{\tau}_{mn}\cdot\mathbf{r}_{uv}},\end{aligned} \tag{3.43}$$

where $\mathbf{r}_{uv} = \boldsymbol{i}_x x_u + \boldsymbol{i}_y y_v$ denotes the source coordinates on the plane.

To reconstruct the total scattered field of an incident finite Gaussian beam, we use a local plane wave assumption

- The beam is highly collimated with a low far-field divergence angle: $\theta_R \ll 20°$.
- The beam waists are significantly larger than the unit cell dimensions: $w_x, w_y \gg a$.

Under these assumptions the Gaussian scattered field is obtained by modulating the plane wave scattering coefficients $(\tilde{A}_{mn}, \tilde{B}_{mn})$ by the incident Gaussian envelope $E_G(x, y, z)$

(modulus and phase):

$$\tilde{A}_{mn}^{(G)} = E_G(x,y,z)\tilde{A}_{mn}, \tag{3.44a}$$

$$\tilde{B}_{mn}^{(G)} = E_G(x,y,z)\tilde{B}_{mn}. \tag{3.44b}$$

To compute the radiation patterns, it is possible to use the field equivalence principle on the surface of the grating mirror. Using the aperture-field method, the scattered field can be substituted by equivalent electric and magnetic surface currents:

$$\mathbf{J}_s = 0, \tag{3.45a}$$

$$\mathbf{J}_{sm} = -2(\boldsymbol{i}_z \times \mathbf{E}_{m0}^{-}). \tag{3.45b}$$

Eq.3.45b is equivalent to:

$$\mathbf{J}_{sm} = 2(\tilde{B}_{m0}^{(G)}\tilde{\mathbf{e}}_{m0}^{\mathrm{TE}} - \tilde{A}_{m0}^{(G)}\tilde{\mathbf{e}}_{m0}^{\mathrm{TM}}). \tag{3.46}$$

The continuous aperture field can be discretized into a grid of equivalent magnetic sources, each possessing an area $\Omega = \Delta x \Delta y$. The far-field magnetic dipole expression is

$$\mathbf{E}_{\mathrm{dip}} = jk\frac{e^{-jkr}}{4\pi r}\boldsymbol{i}_r \times \mathbf{J}_{sm}\Omega, \tag{3.47}$$

and is valid when

$$r \gg \frac{2\max(\Delta x, \Delta y)^2}{\lambda}, \tag{3.48a}$$

$$r \gg \lambda, \tag{3.48b}$$

which are conditions that are easily satisfied in our simulations. Substituting the expression for $\mathbf{J}_{sm}$, the vector cross-product $\boldsymbol{i}_r \times \mathbf{J}_{sm}$ decouples the electric field into the three Cartesian components:

$$\begin{aligned}\mathbf{E}_{\mathrm{dip}} = j\frac{e^{-jkr}}{4\pi r}(\boldsymbol{i}_x k\sin\theta\cos\phi + \boldsymbol{i}_y k\sin\theta\sin\phi + \boldsymbol{i}_z k\cos\theta)\times \\ 2(\tilde{B}_{m0}^{(G)}\tilde{\mathbf{e}}_{m0}^{\mathrm{TE}} - \tilde{A}_{m0}^{(G)}\tilde{\mathbf{e}}_{m0}^{\mathrm{TM}})\Omega,\end{aligned} \tag{3.49}$$

which are expressed as:

$$\mathbf{E}_{\text{x,dip}} = 2\Omega j \frac{e^{-jkr}}{4\pi r} k\cos\theta \times \left(\frac{k_{xm}}{k_{c,m0}} \tilde{B}_{m0}^{(G)} \frac{1}{\sqrt{ab}} e^{-j\boldsymbol{\tau}_{m0}\cdot\mathbf{r}_{uv}} + \tilde{A}_{m0}^{(G)} \frac{k_{y0}}{k_{c,m0}\sqrt{ab}} e^{-j\boldsymbol{\tau}_{m0}\cdot\mathbf{r}_{uv}} \right), \tag{3.50a}$$

$$\mathbf{E}_{\text{y,dip}} = 2\Omega j \frac{e^{-jkr}}{4\pi r} k\cos\theta \times \left(\frac{k_{y0}}{k_{c,m0}} \tilde{B}_{m0}^{(G)} \frac{1}{\sqrt{ab}} e^{-j\boldsymbol{\tau}_{m0}\cdot\mathbf{r}_{uv}} + \tilde{A}_{m0}^{(G)} \frac{-k_{xm}}{k_{c,m0}\sqrt{ab}} e^{-j\boldsymbol{\tau}_{m0}\cdot\mathbf{r}_{uv}} \right), \tag{3.50b}$$

$$\begin{aligned}\mathbf{E}_{\text{z,dip}} = {} & 2\Omega j \frac{e^{-jkr}}{4\pi r} k\sin\theta\cos\phi \\ & \times \left(\frac{-k_{xm}}{k_{c,m0}} \tilde{B}_{m0}^{(G)} \frac{1}{\sqrt{ab}} e^{-j\boldsymbol{\tau}_{m0}\cdot\mathbf{r}_{uv}} + \tilde{A}_{m0}^{(G)} \frac{-k_{y0}}{k_{c,m0}\sqrt{ab}} e^{-j\boldsymbol{\tau}_{m0}\cdot\mathbf{r}_{uv}} \right) \\ & + 2\Omega j \frac{e^{-jkr}}{4\pi r} k\sin\theta\sin\phi \\ & \times \left(\frac{-k_{y0}}{k_{c,m0}} \tilde{B}_{m0}^{(G)} \frac{1}{\sqrt{ab}} e^{-j\boldsymbol{\tau}_{m0}\cdot\mathbf{r}_{uv}} + \tilde{A}_{m0}^{(G)} \frac{k_{xm}}{k_{c,m0}\sqrt{ab}} e^{-j\boldsymbol{\tau}_{m0}\cdot\mathbf{r}_{uv}} \right).\end{aligned} \tag{3.50c}$$

To accurately capture the phase variation of the wave and reduce numerical errors, the dipole grid sampling requirement is chosen with the rule of thumb $\Delta x, \Delta y \leq \lambda/10$ that is often used in computational electromagnetics. Thus, the number of dipoles placed along the dimensions a and b of the unit cell should be:

$$N_x, N_y \geq 10\frac{a}{\lambda}, \tag{3.51}$$

yielding a 2D mesh of $N_x \times N_y$ equivalent dipoles per periodic unit cell. The total reflected field at any observation point (x, y, z) is given by the discrete sum over all grid elements:

$$\mathbf{E}(x,y,z) = \sum_{u=1}^{N_x} \sum_{v=1}^{N_y} \mathbf{E}_{\text{dip}}^{(x_u,y_v)}(x,y,z), \tag{3.52}$$

where (x_u, y_v) are the local transverse coordinates of the (u, v)-th equivalent magnetic dipole on the aperture.

3.3. MATLAB Implementation and Convergence

Eqs. 3.40 and 3.52 are implemented in MATLAB to compute the diffraction efficiencies and to reconstruct the scattered Gaussian fields. The accuracy of the implementation is governed by two convergence parameters and one resolution parameter: the number of slot modes P, the number of equivalent dipoles per unit cell N_{dip}, and the spatial resolution of the reconstructed field. These parameters are analyzed for a lamellar grating geometry with a period $a = 2$ mm, slot width $w = a/8$, and depth $d = a/20$, and for a Gaussian beam at incidence angles $\theta = 20°$, $\phi = 40°$, and frequency 170 GHz. The convergence of the parameter P was assessed by monitoring the relative error of the scattering coefficients computed by our solver against reference HFSS simulations. The HFSS model used for this benchmark is shown in Fig. 3.2.

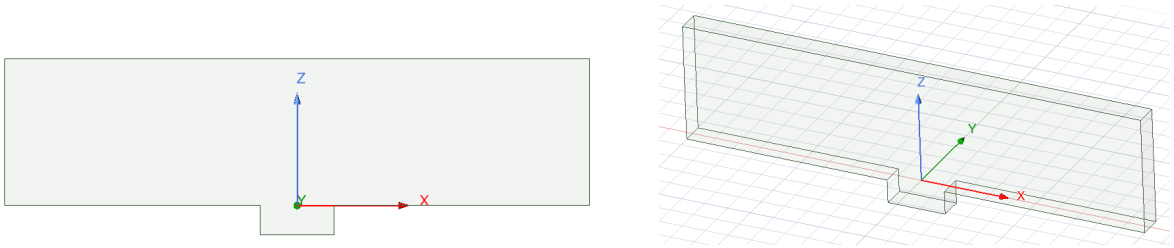


Figure 3.2: HFSS model used as a benchmark for the lamellar grating ($a = 2$ mm, $w = a/8$, $d = a/20$, $\theta = 20°$, $\phi = 40°$). Single unit cell with periodic boundary conditions on the lateral walls and a Floquet port for the incident and diffracted modes.

Fig. 3.3 shows the polar plot of the propagating diffracted orders, reporting the scattering angles $(\theta_{\text{out}}, \phi_{\text{out}})$ for each order under TE and TM polarizations. With this geometry, only the specular reflection and the $m = 1$ order are excited.

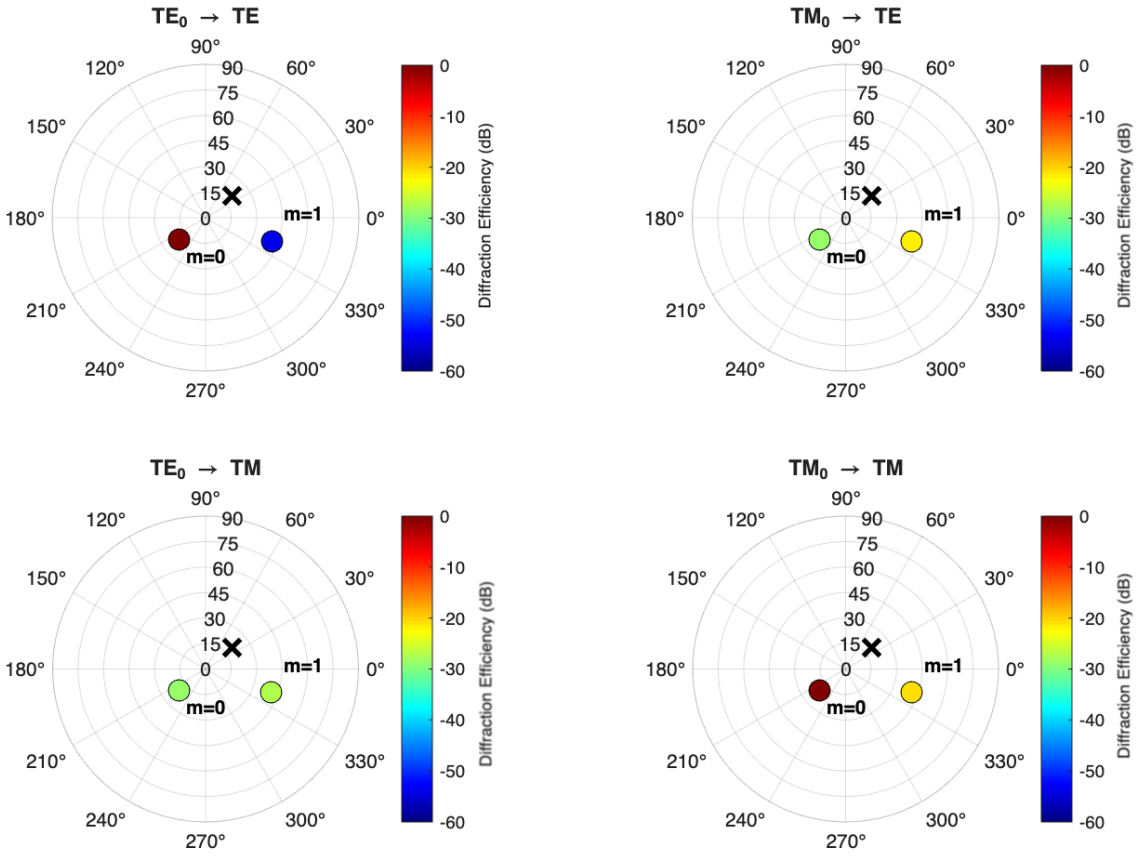


Figure 3.3: Polar plot of the propagating diffracted orders for the example grating ($a = 2$ mm, $w = a/8$, $d = a/20$, $\theta = 20°$, $\phi = 40°$), showing the scattering angles $(\theta_{\text{out}}, \phi_{\text{out}})$ of each order. The incident wave is indicated by the black cross, and propagating orders are denoted by colored circles. The colors represent the diffraction efficiencies in dB ($P = 17$).

As a practical convergence criterion for our solver, we select the smallest P for which the relative change in the scattering coefficients between successive values of P satisfies $\delta S_{dB} < 1\%$. For the grating considered here, this criterion is first met at $P = 17$. The reference HFSS simulations were configured with a strict convergence criterion for the maximum magnitude change in the scattering parameters of $\Delta S_{\text{HFSS}} = 10^{-5}$. Overall, the scattering parameters computed by our mode-matching method show excellent agreement with the HFSS predictions, as shown in Fig. 3.4. The HFSS value is taken as a reference for comparison, not as an exact analytical limit that our simulation is expected to reach for a sufficiently large P. Because the two codes rely on fundamentally different numerical methods, a small residual difference is expected and does not indicate a lack of convergence

in our modal method. To make this agreement explicit, a 1 dB interval centered on each HFSS value is shown as a shaded band in Fig. 3.5.

The diffraction efficiency that exhibits the largest relative difference corresponds to the lowest absolute value in dB (the $TE_0 \rightarrow TE_1$ coupling coefficient, < -50 dB). This deviation is primarily attributed to the mesh discretization limits of the FEM solver; achieving strict convergence in HFSS beyond 10^{-5} for this specific geometry is highly difficult and requires prohibitive computational time. This limitation strongly motivates the development and use of a highly efficient alternative tool like the one presented in this work.

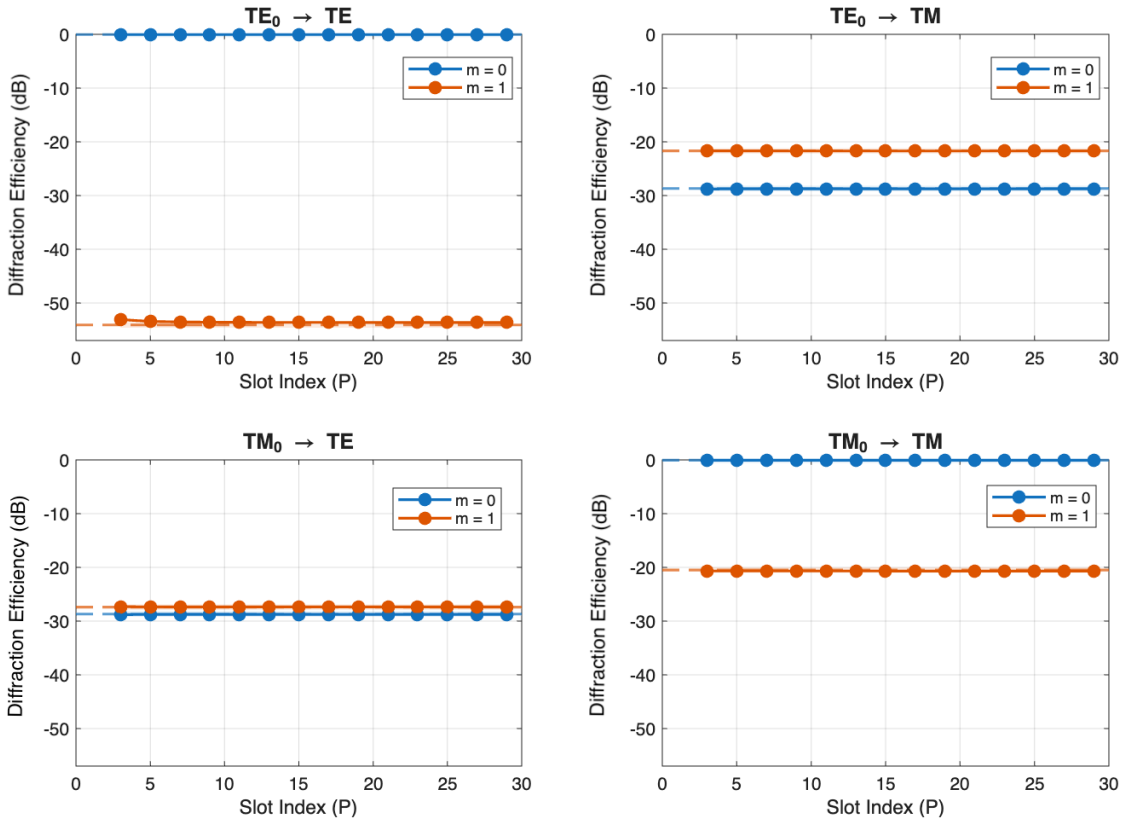


Figure 3.4: Convergence of the scattering coefficients with the number of slot modes P, compared to the reference HFSS values (dashed lines).

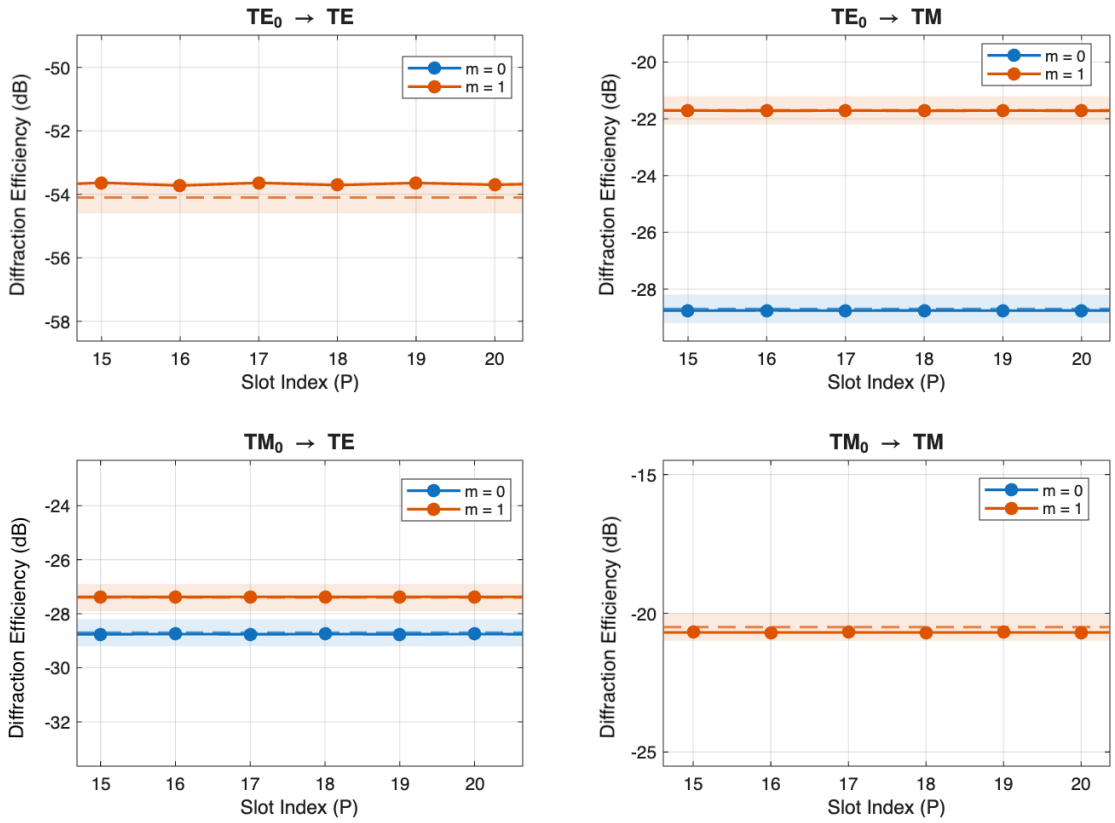


Figure 3.5: Detailed view of the scattering coefficient convergence as a function of slot modes P. The shaded bands indicate a 1 dB interval centered on the HFSS reference values to explicitly illustrate the agreement between the two numerical methods.

The second convergence parameter investigated is the number of equivalent dipoles per unit cell, N_{dip}. With the number of slot modes fixed at its converged value ($P = 17$), N_{dip} was varied to evaluate the accuracy of the reconstructed scattered field. The resulting beams were compared against the analytical predictions derived from the tensor ABCD propagation law. Because the incident Gaussian beam is initially stigmatic and impinges on the reflector exactly at its waist, the tensorial matrices predict that the off-axis diffraction will produce a strictly simple astigmatic beam, rather than a general astigmatic one. To evaluate this, a Gaussian beam incident directly at its waist ($w_{0x} = w_{0y} = 25$ mm) on a flat grating reflector was simulated. To avoid beam truncation effects, the diameter of the reflector D is chosen to be five times the incident beam waist:

$$D = 5w_0 = 125 \text{ mm}. \tag{3.53}$$

The power coupling efficiency η (evaluated using Eq. 1.20a) was computed alongside the beam radii and radii of curvature along the principal astigmatic axes. Moreover, the numerical estimates for the beam radii w are extracted via a Gaussian fit along the major and minor axes of the reconstructed field's amplitude contour ellipses. Because the beam exhibits strictly simple astigmatism, these principal axes perfectly coincide with the principal axes of the phase wavefronts (isophases). This alignment allows for a direct evaluation of both w and R along the exact same transverse coordinate system. To accurately compare the reconstructed field against the theoretical predictions, these spatial parameters are evaluated at an observation plane located 500 mm away from the reflector.

At convergence, the numerically reconstructed fields show a power coupling efficiency of $\eta \simeq 1$ for both TE and TM incident polarizations. Furthermore, because the computed spatial beam parameters are practically identical for both polarizations, Table 3.1 reports only the TM results.

Order	Parameter	$N_{\text{dip}} = 2$	$N_{\text{dip}} = 6$	$N_{\text{dip}} = 12$	Tensor ABCD
$m = 0$	w_{minor} (mm)	27.434	27.434	27.434	27.451
	w_{major} (mm)	27.437	27.437	27.437	27.451
	R_{minor} (mm)	2964.1	2963.8	2963.8	2959.8
	R_{major} (mm)	2964.8	2964.6	2964.6	2959.8
$m = 1$	w_{minor} (mm)	24.140	24.140	24.140	24.149
	w_{major} (mm)	28.370	28.370	28.370	28.385
	R_{minor} (mm)	1342.9	1343.0	1343.1	1341.4
	R_{major} (mm)	3493.9	3493.8	3493.8	3484.3

Table 3.1: Reconstructed beam parameters (minor/major waist w and radius of curvature R) as a function of the number of dipoles per cell N_{dip}, compared with the tensor ABCD law, for the specular ($m = 0$) and diffracted ($m = 1$) orders. Values are reported for TM incidence. The power coupling efficiency at convergence is $\eta \simeq 1$ for both polarizations and both orders.

The results demonstrate excellent agreement between the numerically reconstructed fields and the theoretical predictions. A minor discrepancy between the converged numerical parameters and the ABCD prediction is expected; our numerical model accurately accounts for a reflector of finite extent, whereas the analytical tensor ABCD propagation assumes an infinite reflection plane. For the $D = 5w_0$ configuration, the computed beam

parameters are highly accurate even for N_{dip} values as low as 2. This robust performance is primarily attributable to the planar configuration of the reflector. Because the reflector surface is flat, the phase across the aperture is smooth and highly linear. Given the operating frequency of 170 GHz and the unit cell period $a = 2$ mm, the $\lambda/10$ spatial sampling rule of thumb yields:

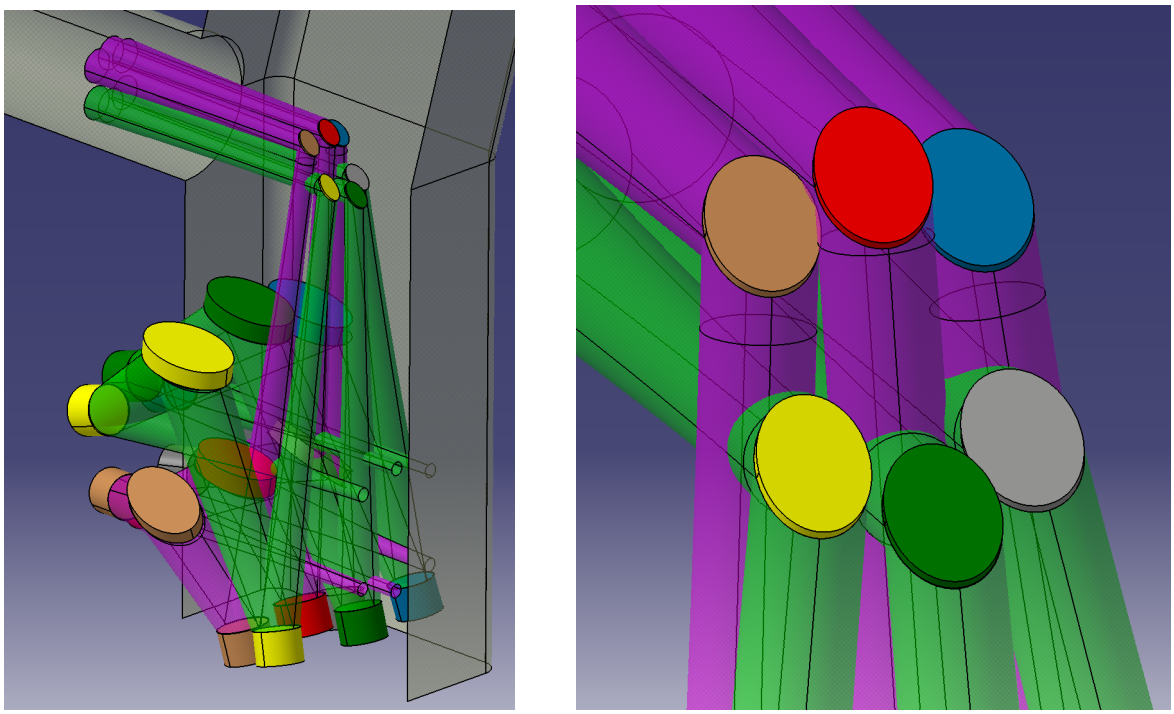
$$N_{\text{dip}} = \left\lceil 10\frac{a}{\lambda} \right\rceil = \lceil 11.3 \rceil = 12 \tag{3.54}$$

The robust early convergence observed in Table 3.1 demonstrates that the standard $\lambda/10$ rule of thumb can be safely relaxed in the case of non-concave reflectors. In order to illustrate the effects of edge diffraction and beam truncation, an additional evaluation was performed using a reflector diameter of $D = 2w_0$ (evaluated at $N_{\text{dip}} = 6$, $P = 17$, under TM polarization). In this scenario, the coupling with the ideal Gaussian beam is worse: the efficiency for the specular order ($m = 0$) falls to $\eta \simeq 0.990$, and for the diffracted order ($m = 1$), it drops to $\eta \simeq 0.943$. It has to be noted that even if the coupling with the ideal Gaussian beam is good, the power lost due to truncation is not negligible, $P_{loss} \simeq 0.135 P_0$.

Finally, the spatial resolution parameter dictates the minimum grid spacing between two consecutive evaluation points of the reconstructed field in the 3D space. Because it only governs the sampling density of the output field, and does not alter the computed beam parameters, it was kept fixed at λ for all simulations presented in this work.

4 | DTT Grating Couplers Design

In this chapter, the numerical tool developed and validated in Chapter 3 is employed to design the grating couplers located at the termination of the multi-beam (MB) transmission line of the ECRH system of the Divertor Tokamak Test [51]. The scattered fields can be rigorously evaluated at an arbitrary observation plane, where a focusing mirror or a horn antenna could be placed. The grating couplers have been optimized to simultaneously satisfy the spatial constraints of the transmission line architecture and the target power coupled into the desired diffraction order. To accommodate the incident footprint without inducing truncation losses, the reflectors are designed with an ellipsoidal shape with a minor axis of $D_x = 102$ mm and a major axis of $D_y = 144$ mm.



(a) MB transmission line exit

(b) Equatorial reflectors detail

Figure 4.1: DTT top (green) and bottom (magenta) equatorial lines. The beams exiting the multi-beam (MB) transmission line are reflected by the planar splitters toward the equatorial ports (a). A detailed close-up of the six equatorial reflectors (b).

4.1. Geometrical parameters

The ECRH system of DTT employs gyrotrons operating at $f = 170$ GHz ($\lambda \simeq 1.76$ mm). Exiting the MB transmission line, the planar splitting mirrors are positioned approximately at the beam waist of the incident beams. The incidence angle is fixed at roughly $\theta \simeq 45°$, for each mirror to properly redirect the energy of the specular reflection toward the launchers. Consequently, the azimuthal angle ϕ, defined as the angle between the plane of incidence and the lamellar grating grooves, becomes a primary design parameter. Three specific mirrors, corresponding to the DTT top equatorial lines, are studied as the reference design cases. Due to the $\theta = 45°$ incidence angle, both the mode propagation map and the efficiency curves exhibit perfect symmetry between 0° and 180°. As discussed in Chapter 2, the fundamental region permitting the propagation of only a single diffracted order, other than the specular reflection, spans roughly one wavelength; however, the exact boundaries of this domain are highly dependent on the grating period a and the azimuthal angle ϕ, as shown in Fig. 4.2.

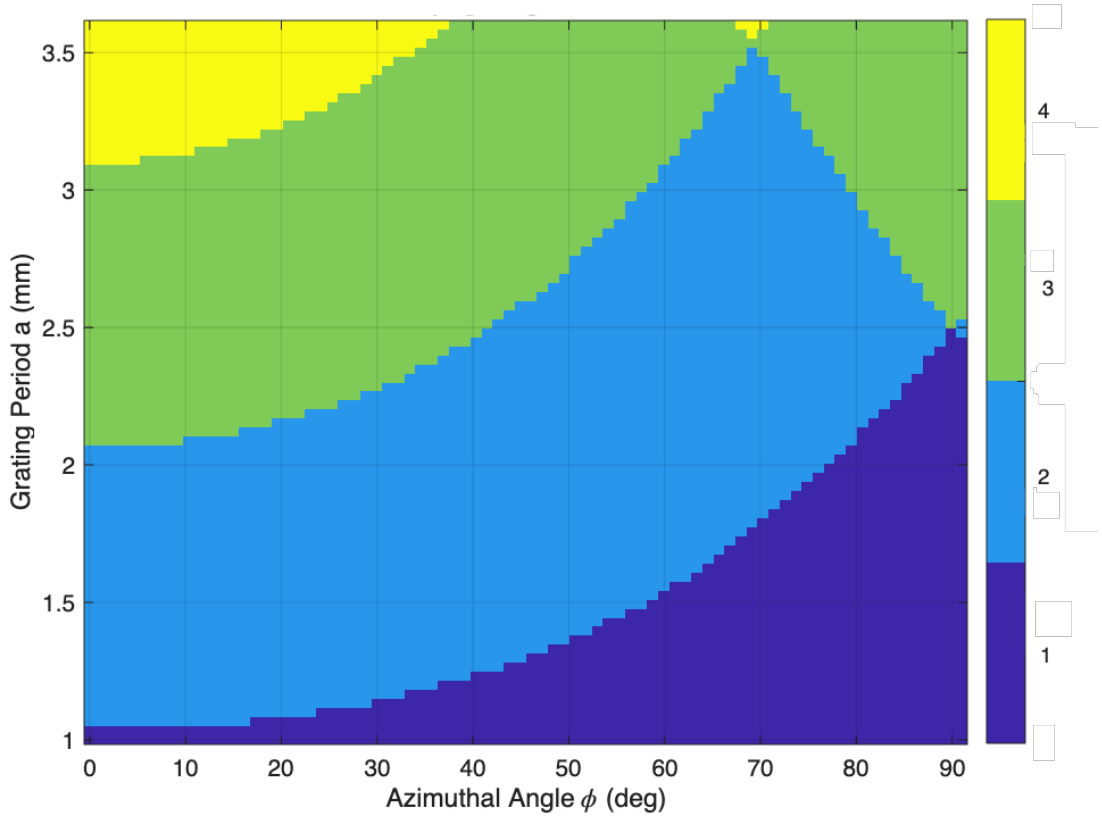


Figure 4.2: Number of propagating modes as a function of the grating period a and azimuthal angle ϕ, at $\theta = 45°$. The light blue area highlights the region where only the specular reflection ($m = 0$) and a single diffracted mode ($m = +1$ or $m = -1$) propagate.

This symmetry facilitates the design of the lateral grating couplers, as they can be synthesized using identical geometrical profiles simply by adding an azimuthal rotation of 180°. The central reflector is required to diffract the beam strictly within the plane of incidence (classical mounting), while the lateral modules must redirect their respective beams out-of-plane (conical mounting). The lateral reflectors are optimized to achieve a precise angle of diffraction that complies with the spatial constraints of the transmission lines and prevents beam interference with adjacent lines. A target diffraction efficiency for the 1st or -1st orders (for any state of polarization), corresponding to < -50 dB, is imposed for these designs. This value guarantees that the scattered total power of mode $m = 1$ is ≤ 10 W, compared to the ~ 1 MW of the specular reflection. The minimum diffraction efficiency coupled into the diagnostic order must remain sufficiently high to ensure reliable detection and measurement by a detector, and is set in our case to > -70 dB.

4.2. Splitting Mirrors Design

In order to evaluate the grating performance and accommodate potential manufacturing variations, the groove width w and depth d must be carefully optimized with a parametric analysis. The maximum achievable diffraction efficiency decreases as the groove depth d is reduced. Furthermore, the efficiency exhibits a localized peak with respect to the groove width w, decreasing when the grooves become either wider or narrower. Repeating the convergence analysis shown in Chapter 3 for our specific geometries, all numerical simulations presented in this section were evaluated using a fixed number of slot modes ($P = 25$, $\delta S_{dB} < 0.1\%$) and equivalent dipoles per cell ($N_{\text{dip}} = 6$). The diffraction efficiencies for each input/output polarization state are shown in Fig. 4.3 for the case of $w = \lambda/22$ and $d = 20$ μm.

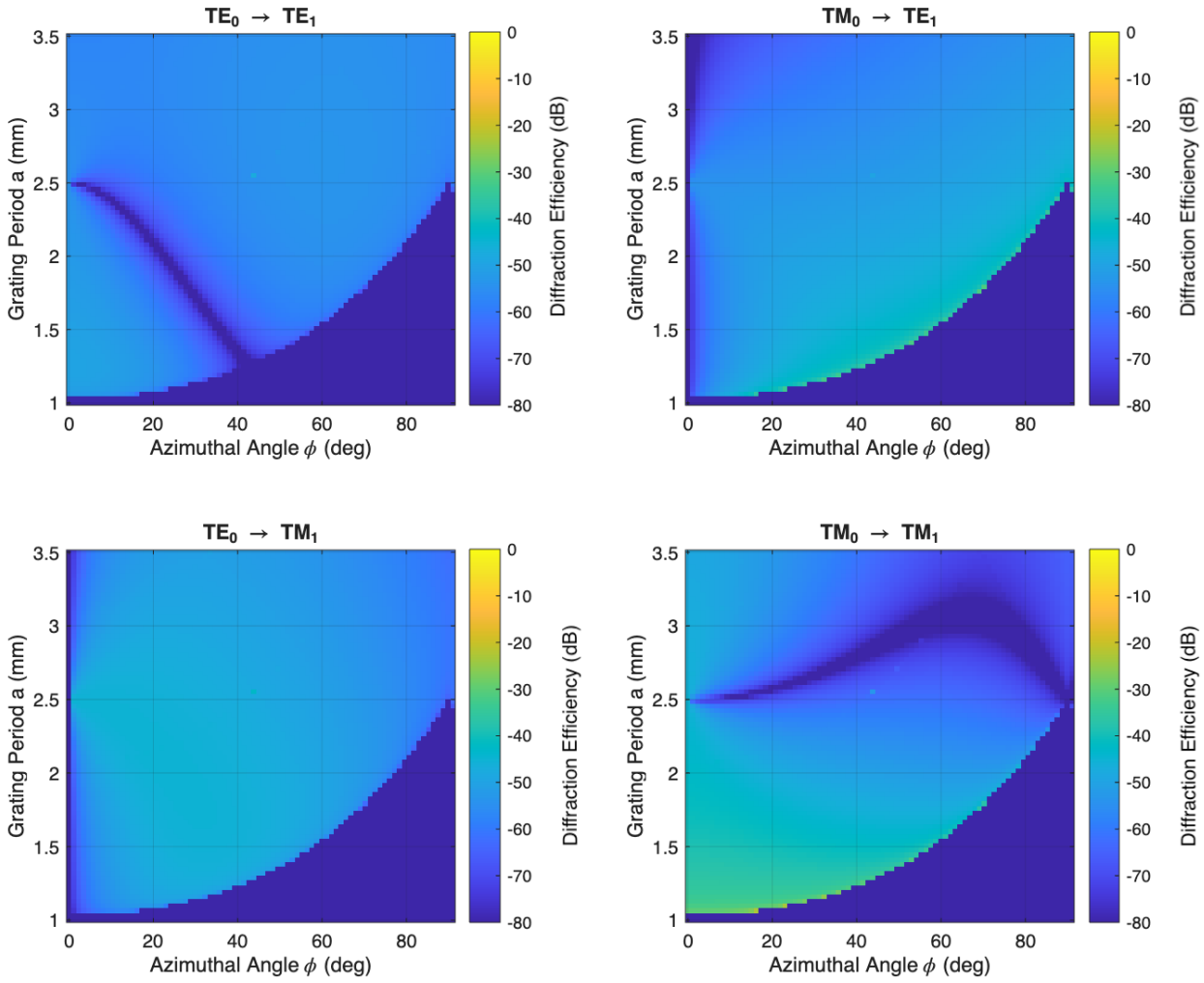


Figure 4.3: Diffraction efficiency as a function of the grating period a and azimuthal angle ϕ. At specific parameter combinations, cross-polarization is negligible. The maps are evaluated for $w = \lambda/22$, $d = 20$ μm and $\theta = 45°$.

Although the magnitude of the diffraction efficiencies changes for varying widths and depths, the overall trend with respect to a and ϕ remains similar for any geometry. In order to have a polarization-independent design criterion for the diffraction efficiency, an additional map is evaluated with the highest diffraction efficiency among all input/output polarizations at each (a, ϕ) coordinate, as shown in Fig. 4.4. The highest diffraction efficiency decreases monotonically as both a and ϕ increase toward the cut-off of the mode $m = 2$ (green area in Fig. 4.2).

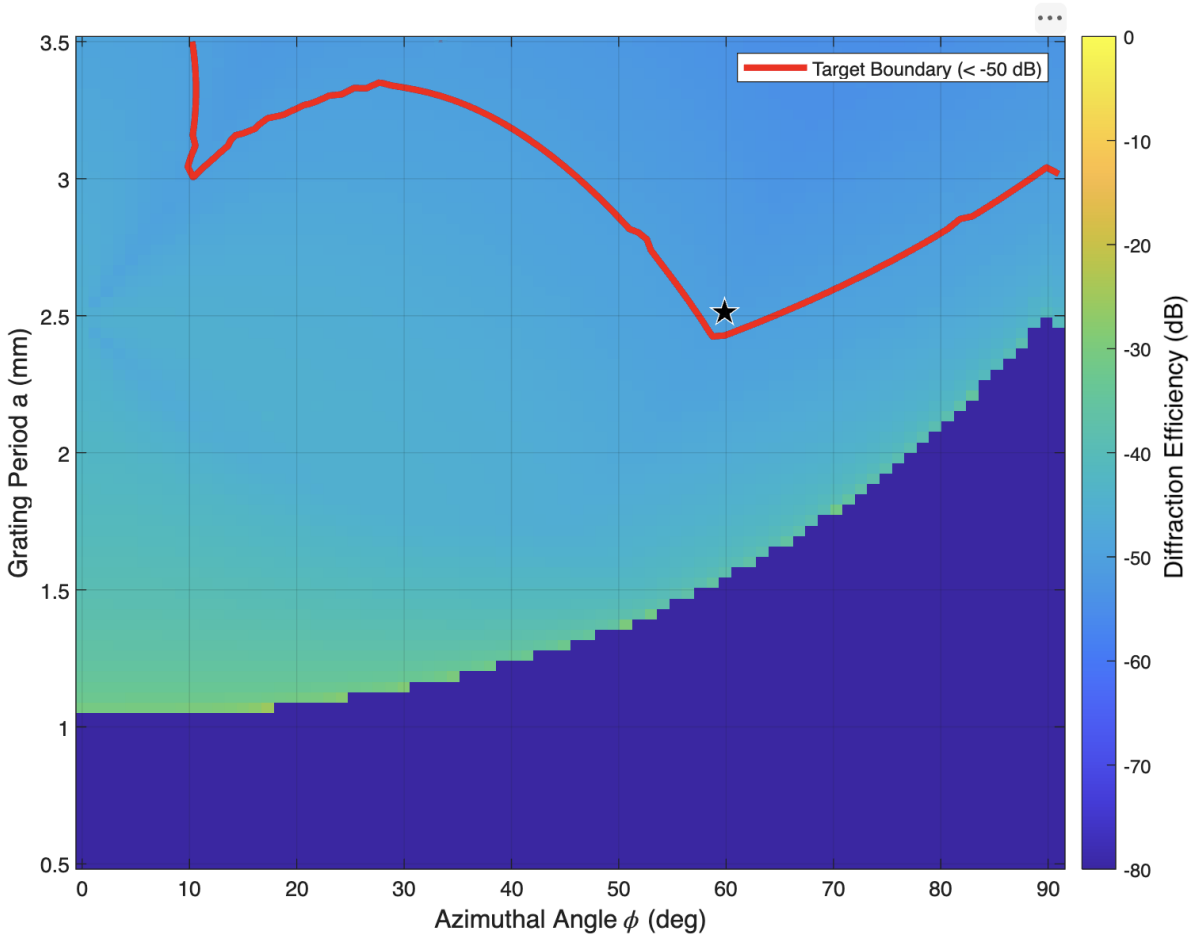


Figure 4.4: Highest diffraction efficiency among all polarizations as a function of a and ϕ. The red line shows the boundary for < -50 dB geometries. The star symbol corresponds to the selected geometry for the lateral couplers. Evaluated for $w = \lambda/22$, $d = 20$ μm and $\theta = 45°$.

For the mode $m = 0$, any polarization variation induced by the grating reflector will be corrected by dedicated grating polarizers, which ensure the main beams are injected into the plasma with the exact required polarization, as described in Sec. 2.3.2. Based on these efficiency maps and target diffraction output angles, the design analysis following in the next paragraphs is performed separately for the central reflector and the lateral grating couplers.

4.2.1. Central Splitting Mirror

The central reflector requires the diffracted beams to propagate in the plane of incidence. An optimal geometry that satisfies this spatial constraint yields a diffraction angle of

$\theta_{out} = 27.9°$. Because the azimuthal orientation is strictly fixed at $\phi = 0°$, the grating operates in a classical mounting configuration. As demonstrated in previous grating coupler designs, such as those studied for the Wendelstein 7-X ECRH system [43], this specific mounting ensures that cross-polarization coupling ($TE_0 \rightarrow TM_1$ and $TM_0 \rightarrow TE_1$) is minimal. With the azimuthal angle constrained, the grating period a is the only geometric degree of freedom available to steer the $m = 1$ mode. To achieve the required target diffraction angle $\theta_{out} = 27.9°$, the period is chosen as $a = 1.5$ mm. The resulting angles of the beams are shown in the polar plots of Fig. 4.5.

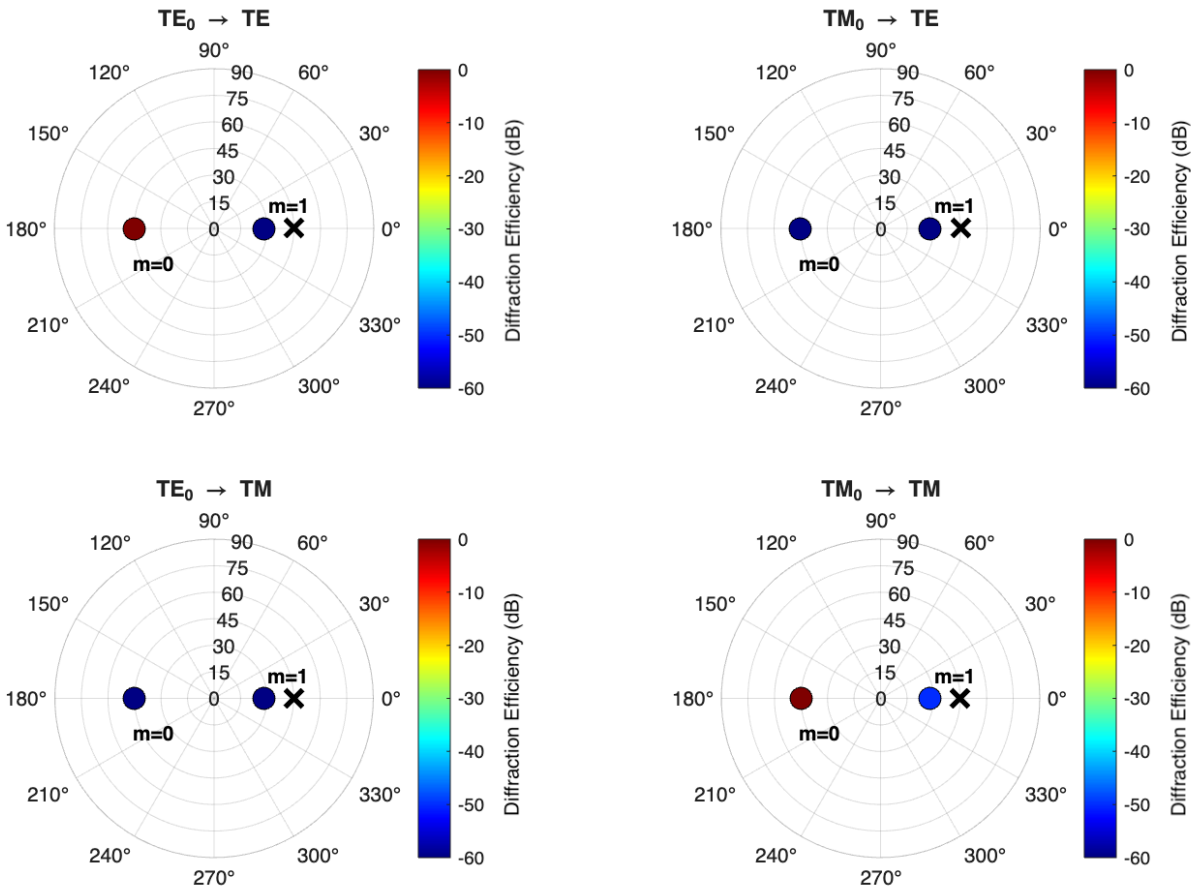


Figure 4.5: Polar representation of the diffracted beams output angles (θ_{out}, ϕ_{out}) for the central reflector ($a = 1.5$ mm, $\phi = 0°$). The diagnostic mode propagates with direction $\theta_{out} = 27.9°$, $\phi_{out} = 0°$.

Fig. 4.6 shows the evaluation of the efficiency of the central mirror as a function of varying

groove widths w and depths d. Because the geometry lacks the azimuthal rotational degree of freedom, achieving an adequate diagnostic coupling efficiency near the -50 dB target is inherently much more difficult. However, through parametric optimization, acceptable performance is achieved by employing a narrow groove width of $w = \lambda/72$ and a depth of $d = 20$ μm.

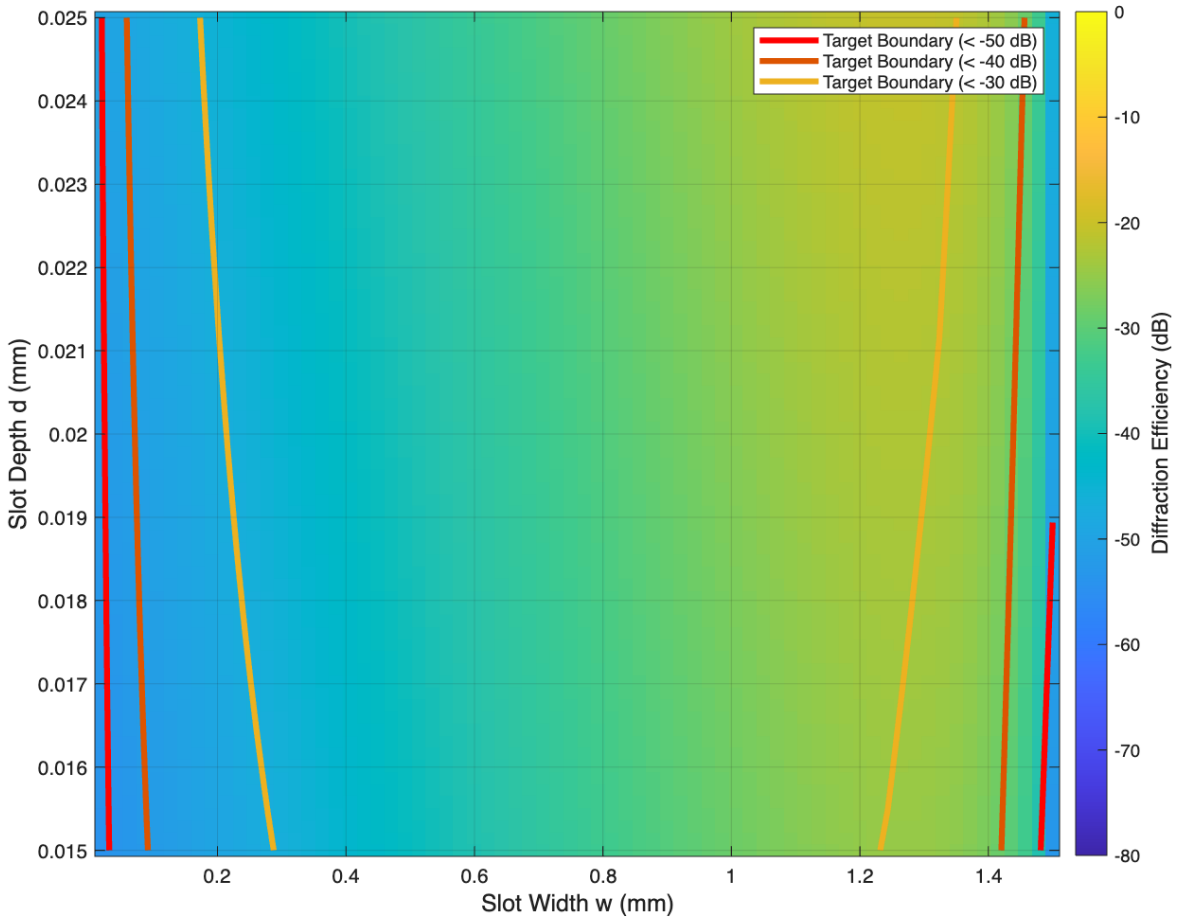


Figure 4.6: Highest diffraction efficiency for the central splitting mirror ($\phi = 0°$) as a function of the groove width w and depth d. Target values are found below the target boundary curves. Classical mounting limits the geometries that achieve a low maximum grating efficiency.

To validate the results of the mode-matching solver, the optimized central reflector configuration was benchmarked against FEM simulations performed with ANSYS HFSS. To ensure good reliability at these low grating efficiencies, the numerical convergence criterion for all scattering parameters within the HFSS solver was set to a maximum variation

$\Delta S_{\text{HFSS}} < 10^{-6}$. Table 4.1 reports the grating efficiency for the mode $m = 1$. Our results are in excellent agreement with HFSS simulations, with only a ~ 1 dB difference for the worst case.

Output Polarization ($m = 1$)	Method	TE Incidence	TM Incidence
TE (dB)	Mode-Matching	-68.95	< -120
	FEM	-70.00	< -120
	Δ	1.05	–
TM (dB)	Mode-Matching	< -120	-50.01
	FEM	< -120	-50.10
	Δ	–	0.09

Table 4.1: Scattering coefficients (dB) for the optimized central reflector ($a = 1.5$ mm, $\phi = 0°$, $w = \lambda/72$, $d = 20$ μm). Comparison between the numerical mode-matching predictions and FEM (ANSYS HFSS) results for the diagnostic diffracted order ($m = 1$).

4.2.2. Lateral Splitting Mirrors

The lateral splitters are designed to deflect the $m = 1$ mode out of the plane of incidence. Unlike the central module, the lateral reflectors can be designed with both the grating period a and the azimuthal orientation ϕ as degrees of freedom. A necessary compromise between diffraction efficiency and the required lateral deflection is achieved using a grating period of $a = 2.5$ mm and an azimuthal angle of $\phi = 60°$. This geometry avoids the excitation of unwanted higher-order modes, keeping only the desired $m = 0$ and $m = 1$ orders. The conical trajectory of the diffracted beams is shown in Fig. 4.7. Furthermore, due to the geometric symmetry of the grating, applying an azimuthal rotation to $\phi = 240°$ ($60° + 180°$) yields the same grating efficiencies and specular diffraction directions. This means that, in the specular case, the diffracted energy is entirely coupled into the $m = -1$ order rather than $m = 1$.

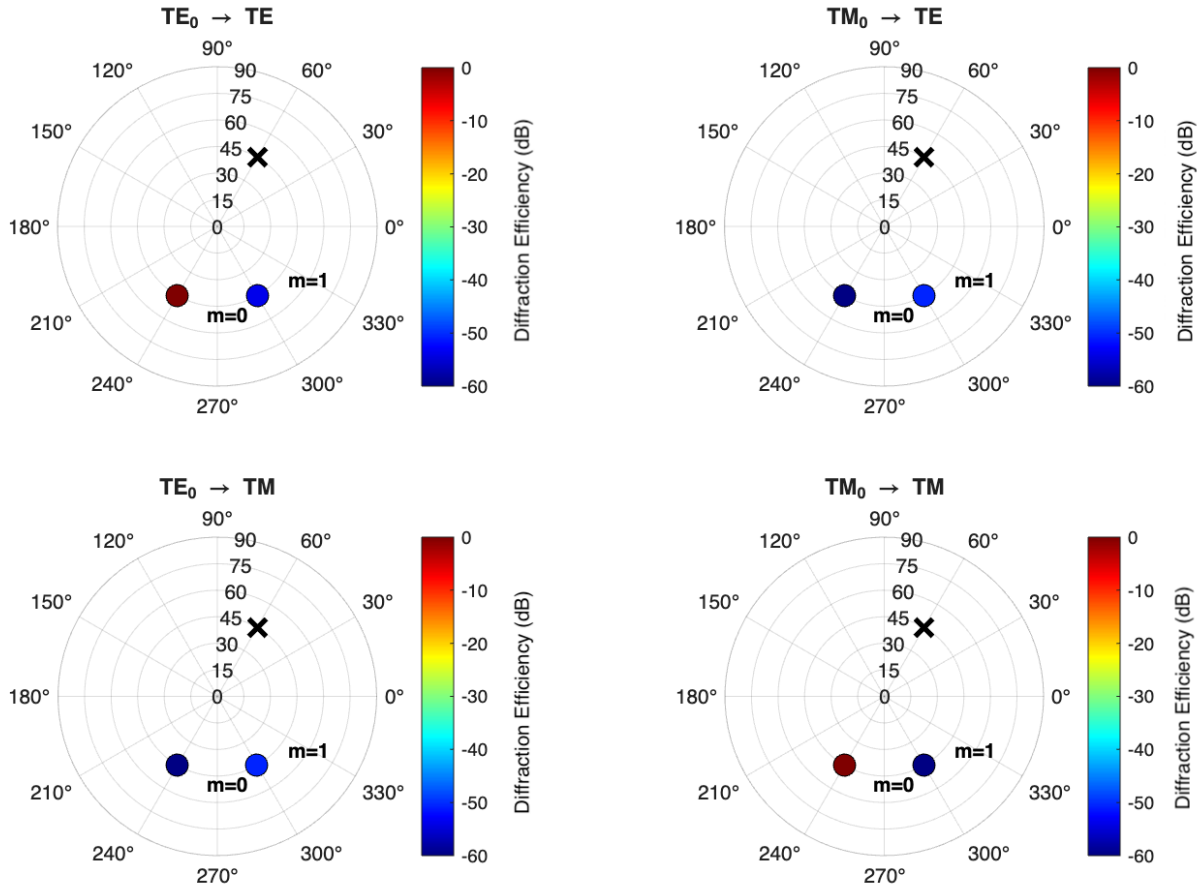


Figure 4.7: Polar representation of the diffracted beams trajectory (θ_{out}, ϕ_{out}) for the lateral reflector ($a = 2.5$ mm, $\phi = 60°$). The diagnostic mode propagates with direction $\theta_{\text{out}} = 44.9°$, $\phi_{\text{out}} = -60.1°$.

Fig. 4.8 shows the grating efficiency for the lateral reflectors as a function of the groove width and depth. Thanks to conical mounting ($\phi = 60°$), these lateral mirrors can achieve lower diffraction efficiencies with higher values d and intermediate values of w.

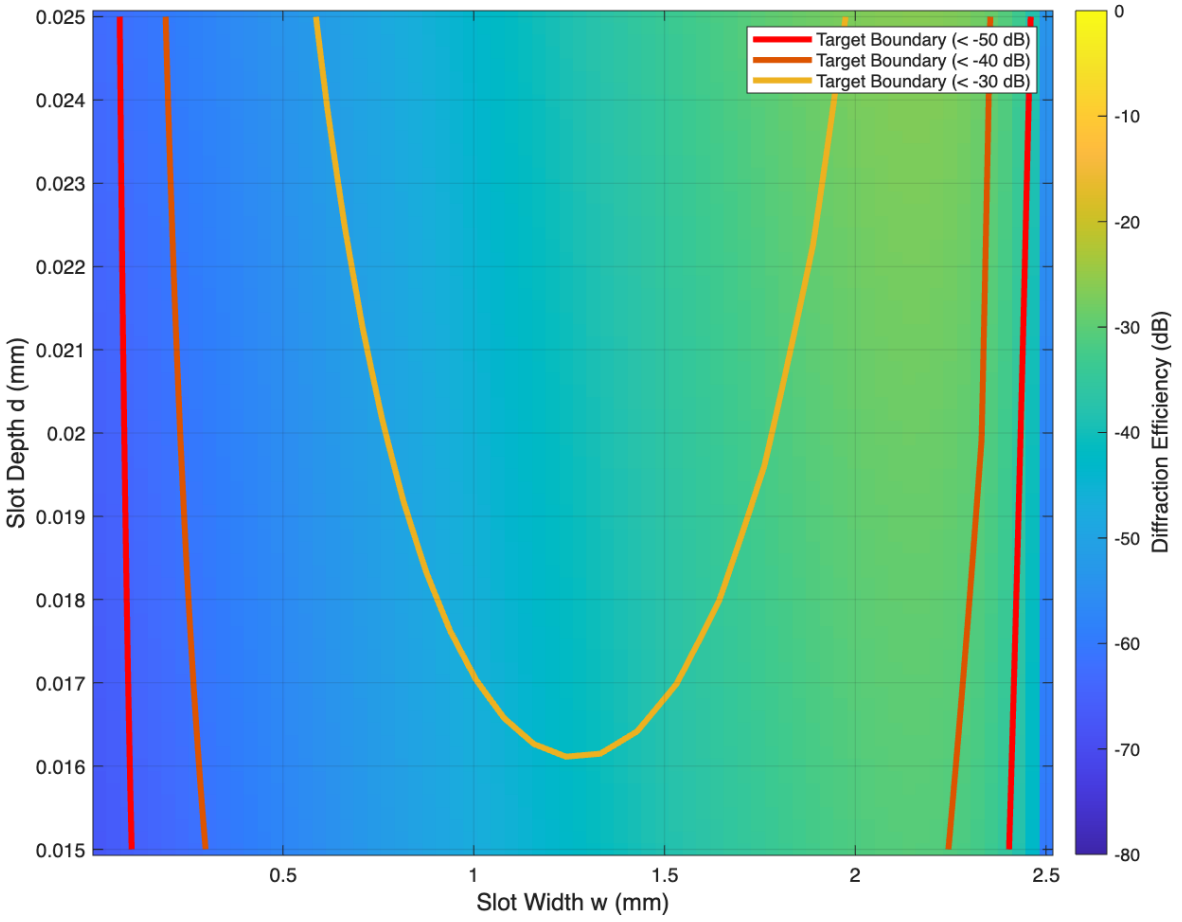


Figure 4.8: Highest diffraction efficiency for the lateral splitting mirrors ($\phi = 60°$) as a function of the groove width w and depth d. Target values are found below the target boundary curves. Conical mounting allows for lower efficiencies than classical mounting.

Similar to the central module, the lateral reflector design was validated against HFSS simulations, with $\Delta S_{\text{HFSS}} < 10^{-6}$. Table 4.2 summarizes the $m = 1$ diffracted scattering coefficients (expressed in dB) for the optimized geometry, explicitly reporting the mode-matching results, the FEM reference values, and the corresponding absolute difference Δ. The results are in excellent agreement, with a maximum difference of 0.11 dB of grating efficiency.

Output Polarization ($m = 1$)	Method	TE Incidence	TM Incidence
TE	Mode-Matching	-53.76	-50.51
	FEM	-53.70	-50.50
	Δ (dB)	0.06	0.01
TM	Mode-Matching	-50.49	-61.78
	FEM	-50.60	-61.70
	Δ (dB)	0.11	0.08

Table 4.2: Scattering coefficients (dB) for the optimized lateral reflectors ($a = 2.5$ mm, $\phi = 60°$, $w = \lambda/22$, $d = 20$ μm). Comparison between the mode-matching predictions and FEM (ANSYS HFSS) results for the diagnostic diffracted order ($m = 1$).

4.3. Gaussian Beam Parameters

The incident Gaussian beams exiting the multi-beam transmission line impinge on the grating couplers approximately at their waist ($w_{0x} = w_{0y} \simeq 25$ mm). Because grating diffraction inherently introduces astigmatism (in this case only simple astigmatism), the spatial characteristics of the Gaussian beams must be evaluated along their principal major and minor axes. The Gaussian beam spatial parameters were evaluated at an observation plane situated exactly 1000 mm (1 m) away from the grating surface. Table 4.3 summarizes the computed beam radii (w) and radii of curvature (R) for the central splitting mirror, for both the primary specular reflection ($m = 0$) and the diagnostic order ($m = 1$). To provide a rigorous benchmark, the numerical results for both TE and TM incident polarizations are compared directly against the predictions derived from the tensor ABCD law.

Order	Method / Polarization	w_{minor} (mm)	w_{major} (mm)	R_{minor} (mm)	R_{major} (mm)
$m = 0$	Tensor ABCD	33.678	33.678	2238.5	2238.5
	Numerical (TE)	33.691	34.560	2153.0	2239.6
	Numerical (TM)	33.682	34.605	2155.8	2240.0
$m = 1$	Tensor ABCD	33.678	36.106	2238.5	4004.9
	Numerical (TE)	33.690	36.492	2234.8	3902.1
	Numerical (TM)	33.685	36.510	2236.0	3908.9

Table 4.3: Gaussian beam parameters (minor/major beam radii w and radii of curvature R) for the central splitting mirror. Values are evaluated at a propagation distance of 1000 mm. The mode-matching solver results for both TE and TM incident polarizations are compared against the tensor ABCD law for the $m = 0$ and $m = 1$ orders.

Similarly, the spatial profiles of the scattered fields were evaluated for the lateral reflector configurations. Because these mirrors employ an azimuthal rotation ($\phi = 60°$) to achieve their conical trajectory, the resulting beams undergo a more severe astigmatic transformation compared to the central mirror. Table 4.4 shows the resulting beam parameters at the 1000 mm observation plane. The excellent agreement between the numerical reconstruction and the tensor ABCD prediction confirms that the reflector preserves the shape of the Gaussian beams. Furthermore, it is worth noting that in all evaluated cases, the coupling efficiency η to the (ideal) fundamental Gaussian mode calculated with the tensor ABCD law is $\eta > 0.999$.

Order	Method / Polarization	w_{minor} (mm)	w_{major} (mm)	R_{minor} (mm)	R_{major} (mm)
$m = 0$	Tensor ABCD	33.678	33.678	2238.5	2238.5
	Numerical (TE)	33.689	33.781	2224.5	2241.1
	Numerical (TM)	33.688	33.780	2227.0	2240.9
$m = 1$	Tensor ABCD	35.592	37.721	1375.0	5109.3
	Numerical (TE)	35.701	37.726	1372.2	5162.8
	Numerical (TM)	35.686	37.730	1373.0	5163.5

Table 4.4: Gaussian beam parameters (minor/major beam radii w and radii of curvature R) for the lateral splitting mirrors. Values are evaluated at a propagation distance of 1000 mm. The mode-matching solver results for both TE and TM incident polarizations are compared against the tensor ABCD law for the $m = 0$ and $m = 1$ orders.

4.4. Fabrication Tolerances and Alternative Designs

For the selected configurations, a sensitivity analysis was performed to evaluate the electromagnetic impact of mechanical fabrication errors. A dimensional variation of $\pm 1\%$ in either the groove width w or the depth d introduces a minor deviation of approximately ± 0.05 to 0.1 dB in the diffraction efficiency, while a larger manufacturing error of $\pm 10\%$ in these parameters results in a broader variation of approximately ± 0.5 to 1 dB. If the precise machining tolerances of the designated manufacturer were explicitly known, the structural parameters w and d could be further optimized. This secondary refinement would guarantee that the coupled diagnostic power strictly remains within the acceptable operational boundaries of -70 dB and -50 dB, even when fabrication errors occur. Moreover, the impact of variations in the grating period a can also be computed. Being a macroscopic parameter with respect to the groove width w and depth d, the grating period a can be easily controlled during manufacturing. For the lateral reflectors ($a = 2.5$ mm), a variation of $\pm 1\%$ in the grating period introduces a deviation of approximately ∓ 0.05 to 0.5 dB in the diffraction efficiency, together with an angular shift of the diffracted order of about $\mp 0.2°$ in θ_{out} and $\mp 0.5°$ in ϕ_{out}; a tighter tolerance of $\pm 0.1\%$ reduces these to a negligible angular shift and a maximum efficiency variation of ∓ 0.05 dB. For the central reflector ($a = 1.5$ mm), a 1% variation produces a deviation of approximately ∓ 0.015 to 0.05 dB in diffraction efficiency and an angular shift of about $\mp 0.7°$ in θ_{out} (with ϕ_{out} unchanged, as the grating operates in classical mounting), while a 0.1% tolerance limits these to $\mp 0.1°$ in θ_{out} and ∓ 0.01 dB in diffraction efficiency. It should also be noted that excessively large variations of a and ϕ may change the number of propagating diffracted orders, by bringing additional orders above cut-off or pushing the desired one below it. Beyond the standard lamellar (rectangular) grooves explored in this work, future investigations could explore alternative geometrical profiles. For instance, a sinusoidal profile could be employed to further optimize the diffraction efficiency, as shown in Fig. 4.9.

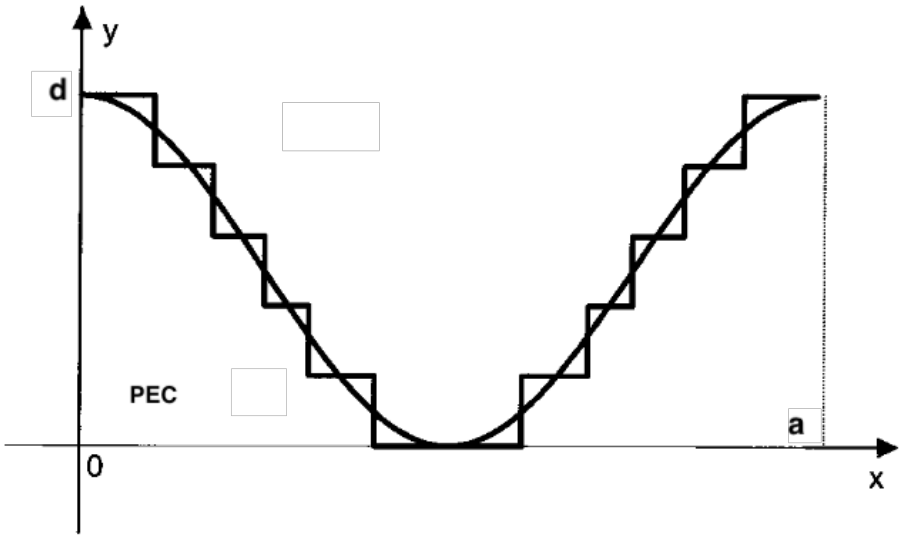


Figure 4.9: Example of a staircase approximation of a sinusoidal profile [83].

Furthermore, another optimization to avoid arcing could be the use of a lamellar shape with rounded edges. Alternatively, employing significantly wider lamellar grooves rather than the highly narrow profiles currently selected could also be considered. However, the physical viability of this wide-groove alternative depends on the specific manufacturing process. Wide-groove geometries require the milling machine to actively remove a substantially larger volume of material from the reflector, increasing both the machining time per mirror and the associated fabrication costs. Finally, the selection of the grating profile must also be evaluated in the context of ohmic losses. The mode-matching theory employed in this work assumes a perfect electric conductor boundary condition. In reality, the physical reflectors will be manufactured from materials like copper, which will experience ohmic heating due to its finite conductivity. Therefore, it is expected that the scattered modes will suffer further power losses in the final implementation.

5 | Conclusions and Future Developments

In this thesis, a rigorous numerical tool based on mode-matching theory was developed and applied to the design of metallic grating couplers for the Electron Cyclotron Resonance Heating (ECRH) system of the Divertor Tokamak Test (DTT) facility. The primary objective of establishing a practical, self-consistent computational tool to evaluate both the diffraction efficiencies and the spatial characteristics of the diffracted Gaussian beams was fully achieved. The accuracy of the developed code was validated through Finite Element Method (FEM) simulations in ANSYS HFSS, demonstrating excellent agreement in predicting the diffraction efficiencies. Furthermore, the tool successfully computed the spatial features of the scattered Gaussian beams, which well-matched the analytical predictions derived from the tensor ABCD law. Although the scope of this work was focused on the design of grating couplers, the mathematical formulation is highly versatile and can be directly utilized for the design of grating polarizers. Furthermore, the tool is independent of the geometry of the reflector, so it can be used to evaluate the scattered fields for any arbitrary mirror shape and to compute any characteristic of the scattered electromagnetic waves. The developed tool is highly efficient for rapid parametric sweeps and optimization loops. Future developments could further expand the features of the code. Currently, only 1D lamellar (rectangular) groove geometries can be simulated. A natural extension would be to generalize the boundary matching conditions to account for any arbitrary groove shape. For instance, sinusoidal profiles could be simulated through a staircase approximation. Moreover, evaluating lamellar shapes with rounded edges could be implemented to model manufacturing optimizations designed to prevent electromagnetic arcing. While the current model operates under the theoretical assumption of a perfect electric conductor (PEC), additional analyses should consider the effect of the finite conductivity of real materials, such as copper. Evaluating the resultant ohmic losses will be a critical next step in accurately assessing the power dissipation and the associated thermal loads on the mirrors under the high-power, continuous-wave operation typical of modern ECRH systems. Moreover, while the current tool effectively evaluates individual

quasi-optical reflectors, it could eventually be expanded to simulate the beam propagation and polarization evolution across the transmission line of the diagnostic. Therefore, future work will extend to modeling the entire diagnostic system, including intermediate focusing mirrors and matching to horn antennas. The goal of this system is to accurately measure the key features of the electron cyclotron waves traveling towards the fusion plasma, such as their power, alignment, mode purity, and polarization.

Bibliography

[1] T. K. Fowler, "Nuclear power—fusion," *Reviews of Modern Physics*, vol. 71, no. 2, p. S456, 1999.

[2] J. Ongena, R. Koch, R. Wolf, and H. Zohm, "Magnetic-confinement fusion," *Nature Physics*, vol. 12, no. 5, pp. 398–410, 2016.

[3] S. Atzeni, "Fusion energy: from basic research to commercialization," *Rendiconti Lincei. Scienze Fisiche e Naturali*, vol. 36, no. 2, pp. 407–416, 2025.

[4] A. Donné, "The european roadmap towards fusion electricity," *Philosophical Transactions of the Royal Society A*, vol. 377, no. 2141, p. 20170432, 2019.

[5] G. Granucci, F. Auriemma, L. Aucone, B. Baiocchi, N. Bonanomi, F. Braghin, A. Bruschi, D. Busi, I. Casiraghi, L. Di Grazia *et al.*, "Roles of ech system in DTT plasma operations," *Nuclear Fusion*, vol. 64, no. 12, p. 126036, 2024.

[6] P. Agostinetti, E. Benedetti, R. Bonifetto, M. Bonesso, M. Cavenago, S. Dal Bello, M. Dalla Palma, D. D'Ambrosio, R. Dima, G. Favero *et al.*, "Improved conceptual design of the beamline for the DTT neutral beam injector," *IEEE Transactions on Plasma Science*, vol. 50, no. 11, pp. 4027–4032, 2022.

[7] Y. Xu, "A general comparison between tokamak and stellarator plasmas," *Matter and Radiation at Extremes*, vol. 1, no. 4, pp. 192–200, 2016.

[8] C. Huang and L. Li, "Magnetic confinement fusion: a brief review," *Frontiers in Energy*, vol. 12, no. 2, pp. 305–313, 2018.

[9] V. Erckmann and U. Gasparino, "Electron cyclotron resonance heating and current drive in toroidal fusion plasmas," *Plasma physics and controlled fusion*, vol. 36, no. 12, pp. 1869–1962, 1994.

[10] H. Zohm, "Recent experimental progress in electron cyclotron resonance heating and electron cyclotron current drive in magnetically confined fusion plasmas," *Fusion Science and Technology*, vol. 52, no. 2, pp. 134–144, 2007.

[11] M. Thumm and W. Kasparek, "Recent advanced technology in electron cyclotron heating systems," *Fusion Engineering and Design*, vol. 26, no. 1-4, pp. 291–317, 1995.

[12] M. Thumm, "State-of-the-art of high-power gyro-devices: 2025 update of experimental results," *Journal of Infrared, Millimeter, and Terahertz Waves*, vol. 46, no. 6, p. 35, 2025.

[13] R. Prater, "Heating and current drive by electron cyclotron waves," *Physics of plasmas*, vol. 11, no. 5, pp. 2349–2376, 2004.

[14] M. K. Thumm and W. Kasparek, "Passive high-power microwave components," *IEEE transactions on plasma science*, vol. 30, no. 3, pp. 755–786, 2003.

[15] M. Thumm, "Modes and mode conversion in microwave devices," in *Generation and Application of High Power Microwaves*. CRC Press, 2020, pp. 121–171.

[16] T. H. Stix, *Waves in plasmas*. Springer Science & Business Media, 1992.

[17] J. Hoekzema, "Electron cyclotron waves," *Fusion science and technology*, vol. 41, no. 2T, pp. 191–196, 2002.

[18] G. S. Nusinovich, M. K. Thumm, and M. I. Petelin, "The gyrotron at 50: Historical overview," *Journal of Infrared, Millimeter, and Terahertz Waves*, vol. 35, no. 4, pp. 325–381, 2014.

[19] K. Felch, H. Huey, and H. Jory, "Gyrotrons for ECH applications," *Journal of Fusion Energy*, vol. 9, no. 1, pp. 59–75, 1990.

[20] M. Thumm, "The gyrotron at 60: Historical overview," in *2025 50th International Conference on Infrared, Millimeter, and Terahertz Waves (IRMMW-THz)*. IEEE, 2025, pp. 1–4.

[21] P. Sprangle, V. L. Granatstein, and A. Drobot, "The electron cyclotron maser instability," *Le Journal de Physique Colloques*, vol. 38, no. C6, pp. C6–135, 1977.

[22] M. Thumm, "Gyro-devices and their applications," in *2011 IEEE International Vacuum Electronics Conference (IVEC)*, Bangalore, India, 2011, pp. 521–524.

[23] A. Tsvetkov, A. Fokin, A. Sedov, and M. Y. Glyavin, "Using a gyrotron as a source of modulated radiation for data transmission systems in the terahertz range," in *EPJ Web of Conferences*, vol. 195. EDP Sciences, 2018, p. 09006.

[24] J. L. Doane, "Propagation and mode coupling in corrugated and smooth-wall circu-

lar waveguides," in *Infrared and Millimeter Waves*, K. J. Button, Ed. New York: Academic, 1985, vol. 13, ch. 5.

[25] E. J. Kowalski, D. S. Tax, M. A. Shapiro, J. R. Sirigiri, R. J. Temkin, T. S. Bigelow, and D. A. Rasmussen, "Linearly polarized modes of a corrugated metallic waveguide," *IEEE Transactions on microwave theory and techniques*, vol. 58, no. 11, pp. 2772–2780, 2010.

[26] G. Keiser, *Fiber Optic Communications*. Singapore: Springer Singapore, 2021.

[27] M. Shapiro and R. Temkin, "Calculation of a hyperbolic corrugated horn converting the TEM00 mode to the HE11 mode," *Journal of Infrared, Millimeter, and Terahertz Waves*, vol. 32, no. 3, pp. 283–294, 2011.

[28] P. F. Goldsmith, *Quasioptical systems*. Chapman & Hall New York, 1998.

[29] H. Kogelnik and T. Li, "Laser beams and resonators," *Applied optics*, vol. 5, no. 10, pp. 1550–1567, 1966.

[30] G. Vallone, "On the properties of circular beams: normalization, Laguerre–Gauss expansion, and free-space divergence," *Optics letters*, vol. 40, no. 8, pp. 1717–1720, 2015.

[31] J. E. Degenford, M. Sirkis, and W. Steier, "The reflecting beam waveguide," *IEEE Transactions on Microwave Theory and Techniques*, vol. 12, no. 4, pp. 445–453, 1964.

[32] L. Empacher and W. Kasparek, "Analysis of a multiple-beam waveguide for free-space transmission of microwaves," *IEEE Transactions on antennas and propagation*, vol. 49, no. 3, pp. 483–493, 2001.

[33] A. Pagliaro *et al.*, "Fluid-dynamic and thermo-mechanical analyses of the metallic steering mirror for the ECRH system of DTT," *Fusion Engineering and Design*, vol. 222, p. 115508, 2026.

[34] C. Zhang *et al.*, "Conceptual design and analysis of remote steering system for CFETR ECRH system," *Nuclear Engineering and Technology*, vol. 56, no. 2, pp. 451–462, 2024.

[35] A. Bruschi *et al.*, "A new launcher for real-time ECRH experiments on FTU," *Fusion Science and Technology*, vol. 55, no. 1, pp. 94–107, Jan. 2009.

[36] J. Doane, J. Anderson, H. Grunloh, and W. Wu, "Power monitor miter bends for high-power microwave transmission," *Fusion Engineering and Design*, vol. 93, pp. 1–8, Apr. 2015.

[37] J. Ruiz, W. Kasparek, C. Lechte, B. Plaum, and H. Idei, "Numerical and experimental investigation of a 5-port mitre-bend directional coupler for mode analysis in corrugated waveguides," *Journal of Infrared, Millimeter, and Terahertz Waves*, vol. 33, no. 5, pp. 491–504, 2012.

[38] W. Weng, D. Xia, Y. Tian, X. Chen, Z. Wang, and Y. Pan, "Investigation on the multi-hole directional coupler for power measurement of the J-TEXT ECRH system," *Plasma Sci. Technol.*, vol. 24, no. 6, p. 065602, Jun. 2022.

[39] D. Wu *et al.*, "The design of directional coupler for ECRH system," *IEEE Access*, vol. 5, pp. 6187–6191, 2017.

[40] A. Zach *et al.*, "In-situ real-time monitoring of spurious modes in HE11 transmission lines using multi-hole couplers in miter bends," *EPJ Web Conf.*, vol. 203, p. 04018, 2019.

[41] T. Notake *et al.*, "Real time polarization monitor developed for high power electron cyclotron resonance heating and current drive experiments in large helical device," *Review of Scientific Instruments*, vol. 76, no. 2, p. 023504, Feb. 2005.

[42] S. Bertolami, F. Di Paolo, A. Bruschi, F. Fanale, A. Moro, S. Garavaglia, G. Granucci, A. Romano, and A. Simonetto, "Mathematical modeling and design of a microwave polarizer for DTT ECRH applications," *Fusion Engineering and Design*, vol. 223, p. 115552, 2026.

[43] J. Shi and W. Kasparek, "A grating coupler for in-situ alignment of a Gaussian beam—principle, design, and low-power test," *IEEE transactions on antennas and propagation*, vol. 52, no. 10, pp. 2517–2524, 2004.

[44] W. Joyce and B. DeLoach, "Alignment of Gaussian beams," *Applied optics*, vol. 23, no. 23, pp. 4187–4196, 1984.

[45] W. Bin *et al.*, "Operations with spherical calorimetric loads in different configurations at gyrotron test stands at EPFL and QST," in *AIP Conference Proceedings*, vol. 2254, no. 1. AIP Publishing LLC, 2020.

[46] A. Bruschi *et al.*, "Calorimetric loads for high power transmission lines at millimeter wavelengths," *Fusion Engineering and Design*, vol. 56, pp. 649–654, Oct. 2001.

[47] A. Bruschi, S. Cirant, F. Gandini, G. Granucci, V. Mellera, V. Muzzini, A. Nardone, A. Simonetto, C. Sozzi, and N. Spinicchia, "Design of a high-power load for millimetre-wave gaussian beams," *Nuclear fusion*, vol. 43, no. 11, pp. 1513–1519, 2003.

[48] A. V. Melnikov, "Applied and fundamental aspects of fusion science," *Nature physics*, vol. 12, no. 5, pp. 386–390, 2016.

[49] F. Romanelli *et al.*, "Divertor tokamak test facility project: status of design and implementation," *Nuclear Fusion*, vol. 64, no. 11, p. 112015, 2024.

[50] S. Garavaglia *et al.*, "Development of the electron cyclotron resonance heating system for Divertor Tokamak Test," *Journal of Vacuum Science Technology B*, vol. 41, no. 4, Jul. 2023.

[51] S. Garavaglia, A. Bruschi, F. Fanale, G. Granucci, A. Moro, P. Platania, A. Romano, S. Schmuck, A. Simonetto, and E. Vassallo, "Development of the multi-beam transmission line for DTT ECRH system," in *EPJ Web of Conferences*, vol. 277. EDP Sciences, 2023, p. 04006.

[52] A. Bruschi *et al.*, "Conceptual design of the DTT ECRH quasi-optical transmission line," *Fusion Engineering and Design*, vol. 194, p. 113727, 2023.

[53] F. Fanale *et al.*, "Status of DTT ECH transmission lines and antennae," *IEEE Transactions on Plasma Science*, vol. 52, no. 9, pp. 3778–3784, 2024.

[54] A. Moro *et al.*, "Progress and challenges of the ECH transmission line design for DTT," *Fusion Engineering and Design*, vol. 202, p. 114391, 2024.

[55] M. C. Hutley, *Diffraction Gratings*. London: Academic Press, 1982.

[56] E. Popov, Ed., *Gratings: Theory and Numeric Applications*, 2nd ed. Institut Fresnel, 2014, iSBN: 978-2-85399-860-4.

[57] S. Vignolini, E. Moyroud, B. J. Glover, and U. Steiner, "Analysing photonic structures in plants," *Journal of the Royal Society Interface*, vol. 10, no. 87, p. 20130394, 2013.

[58] E. Moyroud *et al.*, "Cuticle chemistry drives the development of diffraction gratings on the surface of Hibiscus trionum petals," *Current Biology*, vol. 32, no. 24, pp. 5323–5334, 2022.

[59] E. G. Loewen and E. Popov, *Diffraction Gratings and Applications*. New York: Marcel Dekker, 1997.

[60] H. M. Hoffmann, "Theoretical and experimental studies of the ITER ECRH polarizer and rotator gratings," Ph.D. dissertation, Massachusetts Institute of Technology, 2017.

[61] C. Lechte *et al.*, "Simulation of polarising and reflector gratings for high power mm waves," in *EPJ Web of Conferences*, vol. 203. EDP Sciences, 2019, p. 04010.

[62] T. Harada and T. Kita, "Mechanically ruled aberration-corrected concave gratings," *Applied Optics*, vol. 19, no. 23, pp. 3987–3993, 1980.

[63] D. Fattal, J. Li, Z. Peng, M. Fiorentino, and R. G. Beausoleil, "Flat dielectric grating reflectors with focusing abilities," *Nature Photonics*, vol. 4, no. 7, pp. 466–470, 2010.

[64] Ansys Inc., "ANSYS HFSS (High Frequency Structure Simulator)," 2023. [Online]. Available: https://www.ansys.com/products/electronics/ansys-hfss

[65] D. H. Martin and J. W. Bowen, "Long-wave optics," *IEEE Transactions on Microwave Theory and Techniques*, vol. 41, no. 10, pp. 1676–1690, 1993.

[66] A. E. Siegman, "ABCD-matrix elements for a curved diffraction grating," *Journal of the Optical Society of America A*, vol. 2, no. 10, pp. 1793–1793, 1985.

[67] C. Palmer, *Diffraction Grating Handbook*, 8th ed. MKS Instruments, 2020.

[68] A. A. Tovar and L. W. Casperson, "Generalized beam matrices: Gaussian beam propagation in misaligned complex optical systems," *Journal of the Optical Society of America A*, vol. 12, no. 7, pp. 1522–1533, 1995.

[69] T. A. Corcovilos, "Beyond the ABCDs: A better matrix method for geometric optics by using homogeneous coordinates," *American Journal of Physics*, vol. 91, no. 6, pp. 449–457, 2023.

[70] A. A. Tovar and L. W. Casperson, "Generalized beam matrices IV optical system design," *Journal of the Optical Society of America A*, vol. 14, no. 4, pp. 882–894, 1997.

[71] A. E. Siegman, *Lasers*. University science books, 1986.

[72] J. Alda, "Laser and Gaussian beam propagation and transformation." New York, 2003, vol. 999, p. 1013.

[73] J. Alda, S. Wang, and E. Bernabeu, "Analytical expression for the complex radius of curvature tensor Q for generalized Gaussian beams," *Optics communications*, vol. 80, no. 5-6, pp. 350–352, 1991.

[74] J. A. Arnaud and H. Kogelnik, "Gaussian light beams with general astigmatism," *Applied optics*, vol. 8, no. 8, pp. 1687–1693, 1969.

[75] N. Hodgson and H. Weber, *Laser resonators and beam propagation: fundamentals, advanced concepts and applications*. Springer, 2005.

[76] G. Fortin and N. McCarthy, "4×4 ray matrix for a curved chirped grating at oblique

incidence," *Journal of the Optical Society of America A*, vol. 25, no. 8, pp. 2139–2148, 2008.

[77] Q. Lin *et al.*, "Transformation of non-symmetric Gaussian beam into symmetric one by means of tensor ABCD law," *Optik*, vol. 85, no. 2, pp. 67–72, 1990.

[78] H. G. Beutler, "The theory of the concave grating," *Journal of the Optical Society of America*, vol. 35, no. 5, pp. 311–350, 1945.

[79] V. Erckmann *et al.*, "ECRH for W7-X: Transmission losses of high-power 140-GHz wave beams," *Fusion science and technology*, vol. 55, no. 1, pp. 16–22, 2009.

[80] L. Li, "Use of Fourier series in the analysis of discontinuous periodic structures," *Journal of the Optical Society of America A*, vol. 13, no. 9, pp. 1870–1876, 1996.

[81] L. Li, "Mathematical reflections on the fourier modal method in grating theory," in *Mathematical modeling in optical science*. SIAM, 2001, pp. 111–139.

[82] S.-E. Sandström, G. Tayeb, and R. Petit, "Lossy multistep lamellar gratings in conical diffraction mountings: An exact eigenfunction solution," *Journal of Electromagnetic Waves and Applications*, vol. 7, no. 5, pp. 631–649, 1993.

[83] E. Popov, M. Nevière, B. Gralak, and G. Tayeb, "Staircase approximation validity for arbitrary-shaped gratings," *Journal of the Optical Society of America A*, vol. 19, no. 1, p. 33, 2002.

[84] G. G. Gentili, "Properties of TE-TM mode-matching techniques," *IEEE Transactions on Microwave Theory and Techniques*, vol. 39, no. 9, pp. 1669–1673, Sep. 1991.

[85] The MathWorks Inc., "MATLAB version: 26.1.0.3251617 (R2026a)," Natick, Massachusetts, United States, 2026. [Online]. Available: https://www.mathworks.com

A | Appendix A

The integral projections from Chapter 3 are calculated in this appendix. To simplify the expressions we define:

$$c_{xp} = \cos p\xi, \qquad s_{xp} = \sin p\xi, \tag{A.1}$$

$$c_{zp} = \cos(k_{z,p0}d), \qquad s_{zp} = \sin(k_{z,p0}d), \tag{A.2}$$

$$e^{+}_{xm} = e^{jk_{xm}x}, \qquad e^{-}_{xm} = e^{-jk_{xm}x}, \tag{A.3}$$

and

$$C^{\pm}_{p} = C^{\pm}_{p}(k_x) = \int_{x_1}^{x_2} \cos p\xi e^{\pm jk_x x} dx, \qquad S^{\pm}_{p} = S^{\pm}_{p}(k_x) = \int_{x_1}^{x_2} \sin p\xi e^{\pm jk_x x} dx. \tag{A.4}$$

By orthogonality, we obtain the following conditions:

$$\mathbb{E}^{\mathrm{TE,TE}}_{11} = \frac{1}{ab}\int_{S_{ab}} \tilde{\mathbf{e}}^{\mathrm{TE}*}_{m'0} \cdot \tilde{\mathbf{e}}^{\mathrm{TE}}_{m0}\, dS = \delta_{m'm}, \tag{A.5a}$$

$$\mathbb{E}^{\mathrm{TM,TM}}_{11} = \frac{1}{ab}\int_{S_{ab}} \tilde{\mathbf{e}}^{\mathrm{TM}*}_{m'0} \cdot \tilde{\mathbf{e}}^{\mathrm{TM}}_{m0}\, dS = \delta_{m'm}, \tag{A.5b}$$

$$\mathbb{E}^{\mathrm{TM,TE}}_{11} = \mathbb{E}^{\mathrm{TE,TM}}_{11} = \frac{1}{ab}\int_{S_{ab}} \tilde{\mathbf{e}}^{\mathrm{TM}*}_{m'0} \cdot \tilde{\mathbf{e}}^{\mathrm{TE}}_{m0}\, dS = \frac{1}{ab}\int_{S_{ab}} \tilde{\mathbf{e}}^{\mathrm{TE}*}_{m'0} \cdot \tilde{\mathbf{e}}^{\mathrm{TM}}_{m0}\, dS = 0, \tag{A.5c}$$

$$\mathbb{H}_{22}^{\mathrm{TE,TE}} = \int_{S_{wb}} \mathbf{h}_{p'0}^{\mathrm{TE}*} \cdot \mathbf{h}_{p0}^{\mathrm{TE}}\, dS = \delta_{p'p}\, b \left[k_{y0}^2 \frac{w}{2-\delta_{p0}} + \kappa_{xp}^2 \frac{w}{2-\delta_{p0}} \right] \left| \frac{k_{z,p0}}{\omega\mu} \right|^2 |\cos(k_{z,p0}d)|^2, \tag{A.5d}$$

$$\mathbb{H}_{22}^{\mathrm{TM,TM}} = \int_{S_{wb}} \mathbf{h}_{p'0}^{\mathrm{TM}*} \cdot \mathbf{h}_{p0}^{\mathrm{TM}}\, dS = \delta_{p'p}\, b \left[k_{y0}^2 \frac{w(1-\delta_{p0})}{2-\delta_{p0}} + \kappa_{xp}^2 \frac{w}{2-\delta_{p0}} \right] |\cos(k_{z,p0}d)|^2, \tag{A.5e}$$

$$\mathbb{H}_{22}^{\mathrm{TM,TE}} = \mathbb{H}_{22}^{\mathrm{TE,TM}} = \int_{S_{wb}} \mathbf{h}_{p'0}^{\mathrm{TE}*} \cdot \mathbf{h}_{p0}^{\mathrm{TM}}\, dS = \int_{S_{wb}} \mathbf{h}_{p'0}^{\mathrm{TM}*} \cdot \mathbf{h}_{p0}^{\mathrm{TE}}\, dS = 0. \tag{A.5f}$$

and we can observe that the integrals simplify as follows:

$$\int_{S_{ab}} (\cdot) dS = \int_0^b (\cdot) dy \int_0^a (\cdot) dx = b \int_0^a (\cdot) dx, \tag{A.6}$$

$$\int_{S_{wb}} (\cdot) dS = \int_0^b (\cdot) dy \int_{x_1}^{x_2} (\cdot) dx = b \int_{x_1}^{x_2} (\cdot) dx, \tag{A.7}$$

$$\begin{aligned} \mathbb{E}^{+,\mathrm{TE}} &= \int_{S_{ab}} \frac{\tilde{\mathbf{e}}_{m0}^{\mathrm{TE}*}}{\sqrt{ab}} e^{j\boldsymbol{\tau}_{m0}\cdot\mathbf{r}} \cdot \mathbf{E}_t^+ dS \\ &= b \frac{\tilde{\mathbf{e}}_{m0}^{\mathrm{TE}}}{ab} \cdot [\hat{\mathbf{e}}_{\mathrm{TE}}^+ E_0^{+\mathrm{TE}} + \hat{\mathbf{e}}_{\mathrm{TM}}^+ E_0^{+\mathrm{TM}}] \int_0^a e^{jk_{xm}x} e^{-jk_x^+ x} dx \\ &= -\delta_{m0} E_0^{+\mathrm{TE}}, \end{aligned} \tag{A.8}$$

$$\begin{aligned} \mathbb{E}^{+,\mathrm{TM}} &= \int_{S_{ab}} \frac{\tilde{\mathbf{e}}_{m0}^{\mathrm{TM}*}}{\sqrt{ab}} e^{j\boldsymbol{\tau}_{m0}\cdot\mathbf{r}} \cdot \mathbf{E}_t^+ dS \\ &= b \frac{\tilde{\mathbf{e}}_{m0}^{\mathrm{TM}}}{ab} \cdot [\hat{\mathbf{e}}_{\mathrm{TE}}^+ E_0^{+\mathrm{TE}} + \hat{\mathbf{e}}_{\mathrm{TM}}^+ E_0^{+\mathrm{TM}}] \int_0^a e^{jk_{xm}x} e^{-jk_x^+ x} dx \\ &= \delta_{m0} E_0^{+\mathrm{TM}}, \end{aligned} \tag{A.9}$$

$$
\begin{aligned}
\mathbb{H}^{+,\mathrm{TE}} &= \int_{S_{wb}} \mathbf{h}_{p0}^{\mathrm{TE}*} \cdot \mathbf{H}_t^{+} dS \\
&= \frac{b}{\sqrt{ab}} \frac{k_{z,p0}^{*}}{j\omega\mu} \cos^{*}(k_{z,p0}d) \left(\hat{\boldsymbol{\tau}}^{+} \frac{E_0^{+\mathrm{TE}}}{\eta_{\mathrm{TE}}} - \boldsymbol{i}_z \times \hat{\boldsymbol{\tau}}^{+} \frac{E_0^{+\mathrm{TM}}}{\eta_{\mathrm{TM}}} \right) \cdot \\
&\int_{x_1}^{x_2} \left(\boldsymbol{i}_x \kappa_{xp} \sin p\xi - \boldsymbol{i}_y j k_{y0} \cos p\xi \right) e^{-jk_x^{+}x} dx \\
&= \frac{b}{\sqrt{ab}} \frac{k_{z,p0}^{*}}{j\omega\mu} \cos^{*}(k_{z,p0}d) \left(\hat{\mathbf{h}}_{\mathrm{TE}}^{+} \frac{E_0^{+\mathrm{TE}}}{\eta_{\mathrm{TE}}} + \hat{\mathbf{h}}_{\mathrm{TM}}^{+} \frac{E_0^{+\mathrm{TM}}}{\eta_{\mathrm{TM}}} \right) \cdot \left(\boldsymbol{i}_x \kappa_{xp} S_p^{-} - \boldsymbol{i}_y j k_{y0} C_p^{-} \right),
\end{aligned}
\tag{A.10}
$$

$$
\begin{aligned}
\mathbb{H}^{+,\mathrm{TM}} &= \int_{S_{wb}} \mathbf{h}_{p0}^{\mathrm{TM}*} \cdot \mathbf{H}_t^{+} dS \\
&= \frac{b}{\sqrt{ab}} \cos^{*}(k_{z,p0}d) \left(\hat{\boldsymbol{\tau}}^{+} \frac{E_0^{+\mathrm{TE}}}{\eta_{\mathrm{TE}}} - \boldsymbol{i}_z \times \hat{\boldsymbol{\tau}}^{+} \frac{E_0^{+\mathrm{TM}}}{\eta_{\mathrm{TM}}} \right) \cdot \\
&\int_{x_1}^{x_2} \left(-\boldsymbol{i}_x j k_{y0} \sin p\xi + \boldsymbol{i}_y \kappa_{xp} \cos p\xi \right) e^{-jk_x^{+}x} dx \\
&= \frac{b}{\sqrt{ab}} \cos^{*}(k_{z,p0}d) \left(\hat{\mathbf{h}}_{\mathrm{TE}}^{+} \frac{E_0^{+\mathrm{TE}}}{\eta_{\mathrm{TE}}} + \hat{\mathbf{h}}_{\mathrm{TM}}^{+} \frac{E_0^{+\mathrm{TM}}}{\eta_{\mathrm{TM}}} \right) \cdot \left(-\boldsymbol{i}_x j k_{y0} S_p^{-} + \boldsymbol{i}_y \kappa_{xp} C_p^{-} \right),
\end{aligned}
\tag{A.11}
$$

$$
\begin{aligned}
\mathbb{E}_{12}^{\mathrm{TE,TE}} &= \int_{S_{ab}} \frac{\tilde{\mathbf{e}}_{m0}^{\mathrm{TE}*} e_{xm}^{+}}{\sqrt{ab}} \cdot \mathbf{e}_{p0}^{\mathrm{TE}} dS \\
&= b \sin(k_{z,p0}d) \frac{\hat{\boldsymbol{\tau}}_{m0} \times \boldsymbol{i}_z}{\sqrt{ab}} \cdot \int_{x_1}^{x_2} \left[\boldsymbol{i}_x j k_{y0} \cos p\xi - \boldsymbol{i}_y \kappa_{xp} \sin p\xi \right] e^{jk_{xm}x} dx \\
&= \frac{b}{\sqrt{ab}} \sin(k_{z,p0}d) \tilde{\mathbf{e}}_{m0}^{\mathrm{TE}} \cdot \left(\boldsymbol{i}_x j k_{y0} C_p^{+} - \boldsymbol{i}_y \kappa_{xp} S_p^{+} \right),
\end{aligned}
\tag{A.12}
$$

$$\begin{aligned}\mathbb{E}_{12}^{\mathrm{TM,TE}} &= \int_{S_{ab}} \frac{\tilde{\mathbf{e}}_{m0}^{\mathrm{TM}*} e_{xm}^{+}}{\sqrt{ab}} \cdot \mathbf{e}_{p0}^{\mathrm{TE}} dS \\ &= b \sin(k_{z,p0} d) \frac{\hat{\boldsymbol{\tau}}_{m0}}{\sqrt{ab}} \cdot \int_{x_1}^{x_2} \left[\boldsymbol{i}_x j k_{y0} \cos p\xi - \boldsymbol{i}_y \kappa_{xp} \sin p\xi \right] e^{j k_{xm} x} dx \\ &= \frac{b}{\sqrt{ab}} \sin(k_{z,p0} d) \tilde{\mathbf{e}}_{m0}^{\mathrm{TM}} \cdot \left(\boldsymbol{i}_x j k_{y0} C_p^{+} - \boldsymbol{i}_y \kappa_{xp} S_p^{+} \right),\end{aligned} \tag{A.13}$$

$$\begin{aligned}\mathbb{E}_{12}^{\mathrm{TE,TM}} &= \int_{S_{ab}} \frac{\tilde{\mathbf{e}}_{m0}^{\mathrm{TE}*} e_{xm}^{+}}{\sqrt{ab}} \cdot \mathbf{e}_{p0}^{\mathrm{TM}} dS \\ &= b \sin(k_{z,p0} d) \frac{k_{z,p0}}{j\omega\epsilon} \frac{\hat{\boldsymbol{\tau}}_{m0} \times \boldsymbol{i}_z}{\sqrt{ab}} \cdot \int_{x_1}^{x_2} \left[\boldsymbol{i}_x \kappa_{xp} \cos p\xi - \boldsymbol{i}_y j k_{y0} \sin p\xi \right] e^{j k_{xm} x} dx \\ &= \frac{b}{\sqrt{ab}} \frac{k_{z,p0}}{j\omega\epsilon} \sin(k_{z,p0} d) \tilde{\mathbf{e}}_{m0}^{\mathrm{TE}} \cdot \left(\boldsymbol{i}_x \kappa_{xp} C_p^{+} - \boldsymbol{i}_y j k_{y0} S_p^{+} \right),\end{aligned} \tag{A.14}$$

$$\begin{aligned}\mathbb{E}_{12}^{\mathrm{TM,TM}} &= \int_{S_{ab}} \frac{\tilde{\mathbf{e}}_{m0}^{\mathrm{TM}*} e_{xm}^{+}}{\sqrt{ab}} \cdot \mathbf{e}_{p0}^{\mathrm{TM}} dS \\ &= b \sin(k_{z,p0} d) \frac{k_{z,p0}}{j\omega\epsilon} \frac{\hat{\boldsymbol{\tau}}_{m0}}{\sqrt{ab}} \cdot \int_{x_1}^{x_2} \left[\boldsymbol{i}_x \kappa_{xp} \cos p\xi - \boldsymbol{i}_y j k_{y0} \sin p\xi \right] e^{j k_{xm} x} dx \\ &= \frac{b}{\sqrt{ab}} \frac{k_{z,p0}}{j\omega\epsilon} \sin(k_{z,p0} d) \tilde{\mathbf{e}}_{m0}^{\mathrm{TM}} \cdot \left(\boldsymbol{i}_x \kappa_{xp} C_p^{+} - \boldsymbol{i}_y j k_{y0} S_p^{+} \right),\end{aligned} \tag{A.15}$$

$$\begin{aligned}\mathbb{H}_{21}^{\mathrm{TE,TE}} &= \int_{S_{wb}} \mathbf{h}_{p0}^{\mathrm{TE}*} \cdot \frac{\tilde{\mathbf{h}}_{m0}^{\mathrm{TE}} e_{xm}^{-}}{\sqrt{ab}} Y_{m0}^{\mathrm{TE}} dS \\ &= b \cos^*(k_{z,p0} d) \frac{k_{z,p0}^*}{j\omega\mu} Y_{m0}^{\mathrm{TE}} \frac{\hat{\boldsymbol{\tau}}_{m0}}{\sqrt{ab}} \cdot \int_{x_1}^{x_2} \left[\boldsymbol{i}_x \kappa_{xp} \sin p\xi - \boldsymbol{i}_y j k_{y0} \cos p\xi \right] e^{-j k_{xm} x} dx \\ &= \frac{b}{\sqrt{ab}} \frac{k_{z,p0}^*}{j\omega\mu} \cos^*(k_{z,p0} d) Y_{m0}^{\mathrm{TE}} \tilde{\mathbf{h}}_{m0}^{\mathrm{TE}} \cdot \left(\boldsymbol{i}_x \kappa_{xp} S_p^{-} - \boldsymbol{i}_y j k_{y0} C_p^{-} \right),\end{aligned} \tag{A.16}$$

$$\begin{aligned}\mathbb{H}_{21}^{\mathrm{TM,TE}} &= \int_{S_{wb}} \mathbf{h}_{p0}^{\mathrm{TM}*} \cdot \frac{\tilde{\mathbf{h}}_{m0}^{\mathrm{TE}} e_{xm}^{-}}{\sqrt{ab}} Y_{m0}^{\mathrm{TE}} dS \\ &= b \cos^*(k_{z,p0} d) Y_{m0}^{\mathrm{TE}} \frac{\hat{\boldsymbol{\tau}}_{m0}}{\sqrt{ab}} \cdot \int_{x_1}^{x_2} \left[-\boldsymbol{i}_x j k_{y0} \sin p\xi + \boldsymbol{i}_y \kappa_{xp} \cos p\xi \right] e^{-j k_{xm} x} dx \\ &= \frac{b}{\sqrt{ab}} \cos^*(k_{z,p0} d) Y_{m0}^{\mathrm{TE}} \tilde{\mathbf{h}}_{m0}^{\mathrm{TE}} \cdot \left(-\boldsymbol{i}_x j k_{y0} S_p^{-} + \boldsymbol{i}_y \kappa_{xp} C_p^{-} \right),\end{aligned} \tag{A.17}$$

$$\begin{aligned}\mathbb{H}_{21}^{\mathrm{TE,TM}} &= \int_{S_{wb}} \mathbf{h}_{p0}^{\mathrm{TE}*} \cdot \frac{\tilde{\mathbf{h}}_{m0}^{\mathrm{TM}} e_{xm}^{-}}{\sqrt{ab}} Y_{m0}^{\mathrm{TM}} dS \\ &= b\cos^*(k_{z,p0}d)\frac{k_{z,p0}^*}{j\omega\mu} Y_{m0}^{\mathrm{TM}} \frac{\boldsymbol{i}_z \times \hat{\boldsymbol{\tau}}_{m0}}{\sqrt{ab}} \cdot \int_{x_1}^{x_2} \left[\boldsymbol{i}_x \kappa_{xp} \sin p\xi - \boldsymbol{i}_y j k_{y0} \cos p\xi\right] e^{-jk_{xm}x} dx \\ &= \frac{b}{\sqrt{ab}} \frac{k_{z,p0}^*}{j\omega\mu} \cos^*(k_{z,p0}d) Y_{m0}^{\mathrm{TM}} \tilde{\mathbf{h}}_{m0}^{\mathrm{TM}} \cdot \left(\boldsymbol{i}_x \kappa_{xp} S_p^{-} - \boldsymbol{i}_y j k_{y0} C_p^{-}\right),\end{aligned} \tag{A.18}$$

$$\begin{aligned}\mathbb{H}_{21}^{\mathrm{TM,TM}} &= \int_{S_{wb}} \mathbf{h}_{p0}^{\mathrm{TM}*} \cdot \frac{\tilde{\mathbf{h}}_{m0}^{\mathrm{TM}} e_{xm}^{-}}{\sqrt{ab}} Y_{m0}^{\mathrm{TM}} dS \\ &= b\cos^*(k_{z,p0}d) Y_{m0}^{\mathrm{TM}} \frac{\boldsymbol{i}_z \times \hat{\boldsymbol{\tau}}_{m0}}{\sqrt{ab}} \cdot \int_{x_1}^{x_2} \left[-\boldsymbol{i}_x j k_{y0} \sin p\xi + \boldsymbol{i}_y \kappa_{xp} \cos p\xi\right] e^{-jk_{xm}x} dx \\ &= \frac{b}{\sqrt{ab}} \cos^*(k_{z,p0}d) Y_{m0}^{\mathrm{TM}} \tilde{\mathbf{h}}_{m0}^{\mathrm{TM}} \cdot \left(-\boldsymbol{i}_x j k_{y0} S_p^{-} + \boldsymbol{i}_y \kappa_{xp} C_p^{-}\right).\end{aligned} \tag{A.19}$$

We now add the contribution of the TEM mode, present if $k_{yn} = 0$:

$$\begin{aligned}\int_{S_{wb}} \mathbf{h}_{00}^{\mathrm{TM}*} \cdot \mathbf{H}_t^{+} dS &= \frac{b}{\sqrt{ab}} \cos(kd) \left(\hat{\boldsymbol{\tau}}^{+} \frac{E_0^{+\mathrm{TE}}}{\eta_{\mathrm{TE}}} - \boldsymbol{i}_z \times \hat{\boldsymbol{\tau}}^{+} \frac{E_0^{+\mathrm{TM}}}{\eta_{\mathrm{TM}}}\right) \cdot \boldsymbol{i}_y \int_{x_1}^{x_2} e^{-jk_x^{+}x} dx \\ &= \frac{b}{\sqrt{ab}} \cos(kd) \left(\hat{\mathbf{h}}_{\mathrm{TE}}^{+} \frac{E_0^{+\mathrm{TE}}}{\eta_{\mathrm{TE}}} + \hat{\mathbf{h}}_{\mathrm{TM}}^{+} \frac{E_0^{+\mathrm{TM}}}{\eta_{\mathrm{TM}}}\right) \cdot \boldsymbol{i}_y C_0^{-},\end{aligned} \tag{A.20}$$

$$\begin{aligned}\int_{S_{wb}} \mathbf{h}_{00}^{\mathrm{TM}*} \cdot \frac{\tilde{\mathbf{h}}_{m0}^{\mathrm{TM}} e_{xm}^{-}}{\sqrt{ab}} Y_{m0}^{\mathrm{TM}} dS &= \frac{b}{\sqrt{ab}} \cos(kd) Y_{m0}^{\mathrm{TM}} (\boldsymbol{i}_z \times \hat{\boldsymbol{\tau}}_{m0}) \cdot \boldsymbol{i}_y \int_{x_1}^{x_2} e^{-jk_{xm}x} dx \\ &= \frac{b}{\sqrt{ab}} \cos(kd) Y_{m0}^{\mathrm{TM}} \tilde{\mathbf{h}}_{m0}^{\mathrm{TM}} \cdot \boldsymbol{i}_y C_0^{-},\end{aligned} \tag{A.21}$$

$$\int_{S_{wb}} \mathbf{h}_{00}^{\mathrm{TM}*} \cdot \mathbf{h}_{00}^{\mathrm{TM}} dS = wb\cos^2(kd). \tag{A.22}$$

Table A.1 summarizes the expressions used in the projections:

	field	field(*)
$\mathbf{E}_t^+$	$\frac{\boldsymbol{i}_z \times \hat{\boldsymbol{\tau}}^+}{\sqrt{ab}} e_{x0}^- E_0^{\mathrm{TE}} + \frac{\hat{\boldsymbol{\tau}}^+}{\sqrt{ab}} e_{x0}^- E_0^{\mathrm{TM}}$	
$\mathbf{H}_t^+$	$\frac{\hat{\boldsymbol{\tau}}^+}{\eta_{\mathrm{TE}}\sqrt{ab}} e_{x0}^- E_0^{\mathrm{TE}} - \frac{\boldsymbol{i}_z \times \hat{\boldsymbol{\tau}}^+}{\eta_{\mathrm{TM}}\sqrt{ab}} e_{x0}^- E_0^{\mathrm{TM}}$	
$\tilde{\mathbf{e}}_{m0}^{\mathrm{TE}}$	$\hat{\boldsymbol{\tau}}_{m0} \times \boldsymbol{i}_z$	$\hat{\boldsymbol{\tau}}_{m0} \times \boldsymbol{i}_z$
$\tilde{\mathbf{e}}_{m0}^{\mathrm{TM}}$	$\hat{\boldsymbol{\tau}}_{m0}$	$\hat{\boldsymbol{\tau}}_{m0}$
$\tilde{\mathbf{h}}_{m0}^{\mathrm{TE}}$	$\hat{\boldsymbol{\tau}}_{m0}$	
$\tilde{\mathbf{h}}_{m0}^{\mathrm{TM}}$	$\boldsymbol{i}_z \times \hat{\boldsymbol{\tau}}_{m0}$	
$\mathbf{e}_{p0}^{\mathrm{TE}}$	$(\boldsymbol{i}_x j k_{y0} c_{xp} - \boldsymbol{i}_y \kappa_{xp} s_{xp}) s_{zp}$	
$\mathbf{e}_{p0}^{\mathrm{TM}}$	$(\boldsymbol{i}_x \kappa_{xp} c_{xp} - \boldsymbol{i}_y j k_{y0} s_{xp}) s_{zp} \frac{k_{z,p0}}{j\omega\epsilon}$	
$\mathbf{e}_{00}^{\mathrm{TM}}$	$\boldsymbol{i}_x s_{z0} \frac{k}{j\omega\epsilon}$	
$\mathbf{h}_{p0}^{\mathrm{TE}}$	$-(\boldsymbol{i}_x \kappa_{xp} s_{xp} + \boldsymbol{i}_y j k_{y0} c_{xp}) c_{zp} \frac{k_{z,p0}}{j\omega\mu}$	$(\boldsymbol{i}_x \kappa_{xp} s_{xp} - \boldsymbol{i}_y j k_{y0} c_{xp}) c_{zp}^* \frac{k_{z,p0}^*}{j\omega\mu}$
$\mathbf{h}_{p0}^{\mathrm{TM}}$	$(\boldsymbol{i}_x j k_{y0} s_{xp} + \boldsymbol{i}_y \kappa_{xp} c_{xp}) c_{zp}$	$(-\boldsymbol{i}_x j k_{y0} s_{xp} + \boldsymbol{i}_y \kappa_{xp} c_{xp}) c_{zp}^*$
$\mathbf{h}_{00}^{\mathrm{TM}}$	$\boldsymbol{i}_y c_{z0}$	$\boldsymbol{i}_y c_{z0}$

Table A.1: Summary of the field expressions used in the projection integrals. The second column lists the modes as defined in Chapter 3; the third column lists their complex conjugates.

List of Figures

1.1 Scheme of the main components of a tokamak [2]. Key components include the toroidal and vertical field coils, the ohmic transformer to generate the plasma current, and the vacuum vessel that supports the breeding blanket and the divertor. 6
1.2 Clemmow-Mullaly-Allis (CMA) diagrams of the O-mode (left) and X-mode (right) in the cold plasma approximation. Dashed lines show possible propagation paths from the plasma boundary towards the resonance layer. Shaded areas are inaccessible due to the cut-off conditions [13]. 9
1.3 (a) Simplified scheme of a single-cavity gyrotron [18] and (b)-(c) examples of output coupling schemes for high-power high-frequency gyrotrons [14]. . 11
1.4 Section of a circular corrugated waveguide with radius $a \gg \lambda$, corrugation depth d, corrugation period w_1 and corrugation width w_2 [25]. 13
1.5 LP modes, showing how the degree of circular and radial symmetry changes with m and n: (a) LP_{01}, (b) LP_{02}, (c) LP_{11}-even, (d) LP_{11}-odd, (e) LP_{21}-even, (f) LP_{21}-odd. Even and odd modes are degenerate in the azimuthal direction [25]. 14
1.6 Cross section of a Gaussian Beam, showing the radius of curvature and the beam radius as it diverges [28]. 17
1.7 Sketch of quasi-optical parallel beam waveguides (left) and a multiple-beam waveguide (right) [32]. 18
1.8 Fixed focusing mirror (M1) and steerable flat (M2) mirror of DTT front-steering launchers [33]. 19
1.9 Conceptual schemes of (a) front-steering (FS) launchers and (b) remote-steering (RS) launchers for ECRH systems [34]. 20
1.10 Schematic representation of a miter-bend directional coupler [39]. 21
1.11 Schematic representation of cylindrical (left) and spherical (right) calorimetric loads [46]. 24
1.12 Graphical representation of the ECRH system of DTT: (a) Gyrotron Hall, (b) Quasi-optical evacuated transmission lines, (c) Torus Hall [50]. 25

1.13 Graphical representation of the combiner mirrors (left) and splitter mirrors (right) of a multi-beam transmission line [54]. 27

2.1 Principle of a planar lamellar grating reflector, with grating period a, width w and depth d. The 0th order is the specular reflection, and the -1st order is a diffracted lobe [56]. 30
2.2 Example of groove shapes: rectangular (lamellar), rectangular with rounded edges, triangular and sinusoidal [60]. 31
2.3 Anamorphic beam magnification from a diffraction grating (simplified using planar wavefronts) [67]. 36
2.4 Example of variation of isophote and isophase ellipses during propagation through optical elements. A stigmatic beam becomes a simple astigmatic beam and then a general astigmatic beam [75]. 38
2.5 Experimental configuration of the W7-X grating coupler. M1 and M2 are off-axis ellipsoidal reflectors, and M3 is an off-axis paraboloidal reflector. The effective focal lengths and beam waists shown in the diagram are normalized to (mm). 41
2.6 HFSS geometric model of the grating profile (depicted with a scaled milling radius of $R = 2$ mm for visualization purposes). The actual simulated profile utilizes $R = 16$ mm and $a = 1.68$ mm, yielding the nominal groove depth of $d \simeq 22$ μm. 42
2.7 Polar plot representing the angular diffraction spectrum for the W7-X grating coupler, with the 1st order diffraction angle at $\theta \simeq 34.6°$. 45
2.8 Contour plots showing the achievable polarization angles α and β as a function of the mechanical rotation angles (ϕ_1 and ϕ_2) of the two identical DTT grating polarizers [42]. 46

3.1 Lamellar one-dimensional unit cell with grating period a along x, cell size b along y, groove width $w = x_2 - x_1$, groove depth d. 49
3.2 HFSS model used as a benchmark for the lamellar grating ($a = 2$ mm, $w = a/8$, $d = a/20$, $\theta = 20°$, $\phi = 40°$). Single unit cell with periodic boundary conditions on the lateral walls and a Floquet port for the incident and diffracted modes. 60
3.3 Polar plot of the propagating diffracted orders for the example grating ($a = 2$ mm, $w = a/8$, $d = a/20$, $\theta = 20°$, $\phi = 40°$), showing the scattering angles $(\theta_{\text{out}}, \phi_{\text{out}})$ of each order. The incident wave is indicated by the black cross, and propagating orders are denoted by colored circles. The colors represent the diffraction efficiencies in dB ($P = 17$). 61

3.4 Convergence of the scattering coefficients with the number of slot modes P, compared to the reference HFSS values (dashed lines). 62
3.5 Detailed view of the scattering coefficient convergence as a function of slot modes P. The shaded bands indicate a 1 dB interval centered on the HFSS reference values to explicitly illustrate the agreement between the two numerical methods. 63

4.1 DTT top (green) and bottom (magenta) equatorial lines. The beams exiting the multi-beam (MB) transmission line are reflected by the planar splitters toward the equatorial ports (a). A detailed close-up of the six equatorial reflectors (b). 67
4.2 Number of propagating modes as a function of the grating period a and azimuthal angle ϕ, at $\theta = 45°$. The light blue area highlights the region where only the specular reflection ($m = 0$) and a single diffracted mode ($m = +1$ or $m = -1$) propagate. 68
4.3 Diffraction efficiency as a function of the grating period a and azimuthal angle ϕ. At specific parameter combinations, cross-polarization is negligible. The maps are evaluated for $w = \lambda/22$, $d = 20$ μm and $\theta = 45°$. 70
4.4 Highest diffraction efficiency among all polarizations as a function of a and ϕ. The red line shows the boundary for < -50 dB geometries. The star symbol corresponds to the selected geometry for the lateral couplers. Evaluated for $w = \lambda/22$, $d = 20$ μm and $\theta = 45°$. 71
4.5 Polar representation of the diffracted beams output angles (θ_{out}, ϕ_{out}) for the central reflector ($a = 1.5$ mm, $\phi = 0°$). The diagnostic mode propagates with direction $\theta_{\text{out}} = 27.9°$, $\phi_{\text{out}} = 0°$. 72
4.6 Highest diffraction efficiency for the central splitting mirror ($\phi = 0°$) as a function of the groove width w and depth d. Target values are found below the target boundary curves. Classical mounting limits the geometries that achieve a low maximum grating efficiency. 73
4.7 Polar representation of the diffracted beams trajectory (θ_{out}, ϕ_{out}) for the lateral reflector ($a = 2.5$ mm, $\phi = 60°$). The diagnostic mode propagates with direction $\theta_{\text{out}} = 44.9°$, $\phi_{\text{out}} = -60.1°$. 75
4.8 Highest diffraction efficiency for the lateral splitting mirrors ($\phi = 60°$) as a function of the groove width w and depth d. Target values are found below the target boundary curves. Conical mounting allows for lower efficiencies than classical mounting. 76
4.9 Example of a staircase approximation of a sinusoidal profile [83]. 80

List of Tables

2.1 ABCD matrix representation for ECRH-relevant optical elements. $M = \frac{\cos\theta_{\text{out}}}{\cos\theta_{\text{in}}}$ is the anamorphic magnification factor. For spherical mirrors, R is the physical radius of curvature. For ellipsoidal mirrors, f_{t} and f_{s} are the focal lengths in the tangential and sagittal planes. For the curved grating, the effective radii of curvature are $R_{\text{gt}} = \frac{2\cos\theta_{\text{in}}\cos\theta_{\text{out}}}{\cos\theta_{\text{in}}+\cos\theta_{\text{out}}} R_g$ and $R_{\text{gs}} = \frac{2}{\cos\theta_{\text{in}}+\cos\theta_{\text{out}}} R_g$, where R_g is the physical radius of the grating [28, 66]. . . . 35

2.2 Tensorial Matrix representation for ECRH-relevant optical elements [75–77]. For compactness, trigonometric functions are abbreviated as $c_x = \cos x$, $s_x = \sin x$, and $t_x = \tan x$. $M_\theta = c_{\theta_{\text{out}}}/c_{\theta_{\text{in}}}$ and $M_\phi = c_{\phi_{\text{out}}}/c_{\phi_{\text{in}}}$ the anamorphic magnification factors. 40

2.3 Diffraction efficiencies in dB. Values represent HFSS simulations, with measured results from Shi et al. [43] provided in parentheses. 42

2.4 Evolution of the Gaussian beam parameters along the W7-X alignment system (assuming a real intermediate waist after M1): radius of curvature, tangential and sagittal beam waists, propagation length, and far-field divergence angles. 44

2.5 Evolution of the Gaussian beam parameters along the W7-X alignment system (assuming a virtual intermediate waist upstream of M1): radius of curvature, tangential and sagittal beam waists, propagation length, and far-field divergence angles. 44

3.1 Reconstructed beam parameters (minor/major waist w and radius of curvature R) as a function of the number of dipoles per cell N_{dip}, compared with the tensor ABCD law, for the specular ($m = 0$) and diffracted ($m = 1$) orders. Values are reported for TM incidence. The power coupling efficiency at convergence is $\eta \simeq 1$ for both polarizations and both orders. 64

4.1 Scattering coefficients (dB) for the optimized central reflector ($a = 1.5$ mm, $\phi = 0°$, $w = \lambda/72$, $d = 20$ μm). Comparison between the numerical mode-matching predictions and FEM (ANSYS HFSS) results for the diagnostic diffracted order ($m = 1$). 74
4.2 Scattering coefficients (dB) for the optimized lateral reflectors ($a = 2.5$ mm, $\phi = 60°$, $w = \lambda/22$, $d = 20$ μm). Comparison between the mode-matching predictions and FEM (ANSYS HFSS) results for the diagnostic diffracted order ($m = 1$). 77
4.3 Gaussian beam parameters (minor/major beam radii w and radii of curvature R) for the central splitting mirror. Values are evaluated at a propagation distance of 1000 mm. The mode-matching solver results for both TE and TM incident polarizations are compared against the tensor ABCD law for the $m = 0$ and $m = 1$ orders. 78
4.4 Gaussian beam parameters (minor/major beam radii w and radii of curvature R) for the lateral splitting mirrors. Values are evaluated at a propagation distance of 1000 mm. The mode-matching solver results for both TE and TM incident polarizations are compared against the tensor ABCD law for the $m = 0$ and $m = 1$ orders. 78

A.1 Summary of the field expressions used in the projection integrals. The second column lists the modes as defined in Chapter 3; the third column lists their complex conjugates. 96